Thermo-optical effects in high-power end-pumped vanadate lasers

by

Hencharl Johan Strauss

Dissertation presented in partial fulfilment of the requirements for the degree of Doctor of Philosophy in Physics

at

Stellenbosch University

Department of Physics

Faculty of Science

Promoter: Prof. Hubertus von Bergmann
Co-promoter: Dr. Christoph Bollig

Date: March 2010

Declaration

By submitting this dissertation electronically, I declare that the entirety of the work contained therein is my own, original work, that I am the owner of the copyright thereof (unless to the extent explicity otherwise stated) and that I have not previously in its entirety or in part submitted it for obtaining any qualification.

Date: 10^{th} of February 2010

Abstract

Thermo-optical effects in high-power end-pumped vanadate lasers

Hencharl Johan Strauss
University of Stellenbosch, Private Bag X1, Matieland, 7602, Stellenbosch, South Africa
CSIR, National Laser Centre, PO Box 395, Pretoria, 0001, South Africa

The output power of end-pumped lasers is mainly limited by thermal effects in the bulk crystal gain material. The thermal effects either fracture the crystal or cause degradation in the laser beam quality and output power. This is especially pronounced in Nd:YVO_4 and Nd:$GdVO_4$ which exhibit strong thermal lensing. These two Nd^{3+} vanadate materials are of great value because of their high emission cross sections which makes them excellent gain materials for mode-locked, high repetition rate Q-switched and intra-cavity frequency doubled lasers.

The two Nd^{3+} vanadates have very similar spectral properties but many publications claim that the more expensive Nd:$GdVO_4$ is thermo-optically superior to Nd:YVO_4. However, a debate ensued after theoretical calculations as well as measurements of the thermal conductivity and thermo-optical coefficients indicated that the opposite is true. To our knowledge there has never been a direct comparison of the thermal lensing of these two materials under identical pumping and lasing conditions. In order to contribute to the debate we did such measurements for different crystals of these two materials with equal low doping using three different measurement methods. We subsequently determined that Nd:YVO_4 has slightly lower thermal lensing for the stronger gain π-polarisation.

One of the measurement methods we used is a novel more reproducible one that we developed for this purpose. It is more reproducible because it selectively measures only the focal length of the central, relatively unaberrated part of the thermal lens. Another measurement, utilising a probe beam through the laser crystal, found that there was almost no increase in the temperature when lasing is interrupted. This indicated that there is almost no upconversion present in the crystals which is probably due to their optimally chosen low

doping.

A further consequence of the vanadate debate is that there is still confusion about the value of the important thermo-optical coefficient for the higher gain π-polarisation (dn_e/dT) of Nd:YVO_4. This parameter is of great importance in thermal calculations since the strength of the thermal lens is largely dependent on it. We therefore numerically modelled the thermal lensing in our crystals using different dn_e/dT values and found that the value given by Sato & Taira (2007) matches our experimental results the best.

Our measurements also indicated that the thermal lens dioptric power increased non-linearly with pump power. This appeared to contradict theory of thermal lensing since we knew that there was no upconversion in the crystals (which is the standard explanation for the nonlinear increase). We proceeded to use our numerical modelling to identify the main source of the nonlinear increase as the varying spectral output of the diode pump laser.

The findings in this thesis therefore extend knowledge of the thermo-optical properties of the vanadates and increase understanding of the strongly aberrated thermal lenses formed inside them. Furthermore, the findings now enable the power-scaling of end-pumped vanadates lasers to higher levels.

Opsomming

Termo-optiese effekte in hoë-drywing longitudinale-gepompte vanadaat lasers

Hencharl Johan Strauss
Universiteit van Stellenbosch, Privaat Sak X1, Matieland 7602, Stellenbosch, Suid Afrika
CSIR, National Laser Centre, Posbus 395, Pretoria 0001, Suid Afrika

Die uitset drywing van longitudinale-gepompte vaste-toestand lasers word hoofsaaklik beperk deur termiese effekte in die laser kristal. Die kristal word of gekraak of die laser se bundel kwaliteit en uitset drywing verminder. Dit is veral 'n problem in Nd:YVO_4 en Nd:$GdVO_4$ kristalle waarin sterk termiese lense voorkom. Hierdie twee Nd^{3+} vanadaat kristalle is waardevol vanwee hulle hoë emissie deursnitte wat hulle uitstekend maak as versterkings materiale vir modus-gesinkroniseerde, hoë repitisie, Q-geskakelde en binne-resonator frekwensie-verdubbelde lasers.

Die twee vanadate het baie soortgelyke spektrale eienskappe, maar verskeie publikasies beweer dat die duurder Nd:$GdVO_4$ materiaal termo-opties beter is as Nd:YVO_4. Onlangse teoretiese berekeninge asook metings van die termiese en termo-optiese kwaliteite van die twee kristalle toon egter die teenoorgestelde. Sover ons weet is daar nog geen direkte vergelyking van die termiese lens in hierdie twee materiale onder identiese kondisies gedoen nie. Ons het dus so 'n meting aangepak vir kristalle met identiese lae konsentrasie van die Nd^{3+} ioon deur drie verskillende meet metodes te gebruik.

Een van die meet metodes is 'n nuwe, meer reproduseerbare metode wat ons ontwikkel het vir hierdie doel. Dit is meer reproduseerbaar omdat dit slegs die binneste deel van die termiese lens meet wat min sferiese aberrasie het. 'n Ander meeting, wat 'n toets-bundel deur die kristal stuur, het getoon dat daar byna geen verhoging in die die temperatuur van die kristal was toe ossilasie in die resonator onderbreek was nie. Dit is 'n aanduiding dat dat daar byna geen op-omskepping teenwoordig is in die kristalle nie wat te danke is aan hul optimale lae konsentrasie van die Nd^{3+} ioon.

'n Verdere gevolg van die debat is dat daar nog verwarring in die literatuur bestaan oor

die waarde van Nd:YVO_4 se termo-optiese dn_e/dT koeffisiënt. Hierdie parameter is van groot belang in berekinge van die termiese lens se fokale lengte vir die hoër wins π-polarisasie. Deur numeriese modellering te gebruik het ons bevind dat die waarde wat verskaf word deur Sato & Taira (2007) ons eksperimentele data die beste pas.

Ons metings het ook aangedui dat die dioptriese krag van die termiese lens nie linieër toeneem ten opsigte van die geabsorbeerde pomp krag nie. Dit was oënskynlik teenstryding met teorie oor termiese lense. Dit is omdat ons bevestig het dat daar geen op-omskepping in die kristalle teenwoordig was nie, wat die standaard verklaring vir die nie linieëriteit is. Ons het dus ons numeriese modellering gebruik om die hoofbron van die nie-liniëre toename te identifiseer as die veranderende spektrale uitset van die diode pomp laser.

Die bevindings in hierdie tesis bou dus kennis op oor die termo-optiese eienskappe van die vanadate en versterk begrip van die sterk termiese lense binne hulle. Verder stel die bevindings ons nou in staat om die uitset drywing van longitudinale-gepompte vanadaat lasers na hoër vlakke te skaal.

Acknowledgments

I would like to thank Prof. Hubertus von Bergmann for believing in me as well as Dr. Christoph Bollig for sharing his wealth of knowledge on diode-pump solid-state lasers.

Aan my ouers en al die maatjies

Contents

List of Figures

List of Tables

List of Symbols

Symbol	Quantity	Section
a	Directions $\perp$ crystallographic optical axis	Section 2.3.1
α_{abs}	Absorption coefficient	Section 2.3.2
$\alpha_{\text{abs}-a,c}(\lambda)$	Absorption coefs. a and c-direc.	Section 7.2.6
$\alpha_{\text{dio}-a,c}(\lambda)$	Diode abs. coef. a and c-direc.	Section 7.2.6
α_{th}	Thermal expansion coefficient	Section 2.3.2
$\alpha_{\text{th}-c}$	Thermal expansion coefficient c-direc.	Section 2.3.2
$\alpha_{\text{th}-a}$	Thermal expansion coefficient a-direc.	Section 2.3.2
A_n	Sellmeier A defocus coefficients	Section 2.3.4
A_{ft}	Temperature profile radial constant	Section 3.5
A_{sl}	Seidel A defocus coefficient	Section 3.4.4
a_z	Zernike radius	Section 3.4.4
A_2^0	Defocus Zernike coefficient	Section 3.4.4
A_4^0	Spherical aberration Zernike coefficient	Section 3.4.4
B_n	Sellmeier B coefficients	Section 2.3.4
B_{sl}	Seidel B spherical coefficient	Section 3.4.4
c	Crystallographic optical axis	Section 2.3.1
C_n	Sellmeier C coefficient	Section 2.3.4
C_{sl}	Seidel C coefficient	Section 3.4.4
c	Speed of light	Section 4.2.5
C_{ind}	Factor independent of pump radius	Section 5.2.2
D	Dioptric power	Section 5.2.2
$D_{\text{single, double}}$	Single and double pumped dioptric powers	Section 6.3.2
D_{eff}	Effective dioptric power	Section 6.3.2
D_n	Sellmeier D coefficient	Section 2.3.4
ΔD_{th}	Range of stable dioptric powers	Section 5.2.2
d_r	Displacement at radius r	Section 3.4.2
d_{al}	Alignment displacement in a crystal	Section 3.7.1
d	Diameter of the diode pump fibre core	Section 5.2.1

Symbol	Quantity	Section
E_{YM}	Young's modulus	Section 2.3.2
E	Electric field	Section 2.3.4
f	Focal length of a perfect lenses	Section 3.4.5
f_{th}	Focal length of a thermal lens	Section 3.4.5
$\lvert\Delta\frac{1}{f_{\mathrm{th}}}\rvert$	Stable range of dioptric powers	Section 5.2.2
f_{col}	Focal length of a collimating lens	Section 5.2.4
f_{foc}	Focal length of a focusing lens	Section 5.2.4
g_1	Cavity stability parameter side 1	Section 4.2.5
g_2	Cavity stability parameter side 2	Section 4.2.5
h	Zernike summation	Section 3.4.4
$I_{\mathrm{dio}}(\lambda)$	Spectral profile of the diode laser	Section 7.2.6
$I_{\mathrm{dio}}(x)$	Intensity profile of diode laser	Section 5.2.4
j	Zernike radial order	Section 3.4.4
k_{th}	Thermal conductivity	Section 2.2
$k_{\mathrm{th}-c}$	Thermal conductivity c-direc.	Section 2.3.2
$k_{\mathrm{th}-a}$	Thermal conductivity a-direc.	Section 2.3.2
$k_{\mathrm{th}}(T)$	Temp dep. thermal conductivity	Section 7.2
$k_{\mathrm{th},x,y,z}(T)$	Temp dep. thermal conductivity in x,y,z directions	Section 3.3
k_λ	Wavenumber	Section 3.4.5
K_{s}	Kurtosis parameter	Section 5.2.4
$L_{1,2}$	Left and right arm lengths of a resonator	Section 4.2
l_{cr}	Crystal length before heating	Section 2.3.2
Δl_{cr}	Increase in crystal length due to heating	Section 2.3.2
l_{rs}	Total resonator length	Section 4.2.5
λ	Wavelength	Section 2.3.4
λ_{lr}	Laser wavelength	Section 5.2.2
λ_{p}	Pump wavelength	Section 5.2.1
$\lambda_{\text{dio-min}}$	Minimum pump wavelength	Section 5.2.7
$\lambda_{\text{dio-max}}$	Maximum pump wavelength	Section 5.2.7
L_{ls}	Sum of losses (excl. transmission)	Section 5.2.2
M^2	Beam quality factor	Section 5.2.1
$\mathrm{M}^2_{\mathrm{x}}$	Beam quality in x-direction	Section 5.5
$\mathrm{M}^2_{\mathrm{y}}$	Beam quality in y-direction	Section 5.5
n	Refractive index	Section 2.2
n_e	Refractive index e-direction	Section 2.3.2
n_o	Refractive index o-direction	Section 2.3.2
$n(r)$	Refractive index at radial distance r	Section 3.4.1
n_{unp}	Refractive index of an un-pumped crystal	Section 3.4.1
dn/dT	Thermo-optical coefficient	Section 2.3.4

Symbol	Quantity	Section
$dn/dT(\lambda)$	Wavelength dep. thermo-optical coefficient	Section 2.3.4
dn_o/dT	Thermo-optical coefficient o-direc.	Section 2.4
dn_e/dT	Thermo-optical coefficient e-direc.	Section 2.4
NA	Numerical aperture	Section 5.2.1
η_{abs}	Percentage of pump power absorbed	Section 5.2.2
$\eta_{\text{p-q}}$	Pump quantum efficiency	Section 5.2.2
η_{slope}	Slope efficiency	Section 5.2.2
η_{PH}	% of pump power into heat	Section 3.5
o	Transverse higher order mode number x	Section 4.2.5
p	Transverse higher order mode number y	Section 4.2.5
P_{abs}	Absorbed pump power	Section 5.2.2
$P_{\text{left,right}}$	Left and right absorbed pump powers	Section 6.3.2
ρ	Normalised radial distance	Section 3.4.4
π	polarisation $\|\|$ to c-direction	Section 2.3.4
$\Delta\phi(r)$	Phase change profile	Section 3.4.1
$\frac{d}{dz}\Delta\phi(r,z)$	Differential phase change profile	Section 3.4.1
$\Delta\phi_{\frac{dn}{dT}}(r)$	Refractive index phase change profile	Section 3.4.1
$\Delta\phi_{\text{bg}}(r)$	Bulging phase change profile	Section 3.4.2
$\Delta\phi_{\text{tot}}(r)$	Total phase change profile	Section 3.4.3
$\Delta\phi_{\text{lens}}(r)$	Phase change of perfect lens	Section 3.4.5
$\phi_{\text{Gauss}}(r)$	Phase of Gaussian beam	Section 3.8
$\phi_{\text{pr}}(r)$	Phase of probe beam	Section 3.8
$d\phi_{\text{pr}}(r)/dr$	Derivative of probe phase	Section 3.8
q	Longitudinal higher order mode number	Section 4.2.5
q_H	Total heat load	Section 7.2
r	Radial distance in crystal	Section 3.3
$R_{1,2}$	Left and right resonator mirror radii	Section 4.2
R_{cr}	Crystal radius	Section 3.5
R_{G}	Gaussian radius of curvature	Section 3.8
$R_u^j(\rho)$	Radial Zernike polynomial	Section 3.4.4
$\Delta S_{\text{ag}}(r)$	Sag function	Section 3.4.2
s_{al}	Alignment sensitivity	Section 3.7.1
S_{al}	Total alignment sensitivity	Section 3.7.1
σ	Polarisation $\perp$ to c-direction	Section 2.3.4
σ_{vM}	Von Mises stress	Section 3.10
$\sigma_{1,2 \text{ and } 3}$	Stresses in the principle axes	Section 3.10
σ_{max}	Max stress in the crystal	Section 5.2.2

Symbol	Quantity	Section
σ_{em}	Stimulated-emission cross section	Section 5.2.2
θ_{al}	Angular mirror misalignment	Section 3.7.1
τ_{s}	Upper laser level lifetime	Section 2.1
$\Delta T(r,z)$	Temperature increase due to heating	Section 2.3.2
$T(r,z)$	Temperature profile	Section 3.3
$t_{\mathrm{cr}}(r)$	Transfer function of crystal	Section 3.8
T_{OC}	Output coupler transmission	Section 5.2.2
u	Zernike azimuthal order	Section 3.4.4
ν_{Pois}	Poisson's ratio	Section 2.3.2
$\nu_{r,s,q}$	Laser resonance frequencies	Section 4.2.5
ν_{t}	Transverse resonance frequency	Section 4.2.5
ν_{l}	Longitudinal resonance frequency	Section 4.2.5
ν_{p}	Pump frequency	Section 5.2.2
ν_{l}	Laser frequency	Section 5.2.2
w_{l}	Laser radius	Section 5.2.2
w_0	Laser waist radius	Section 5.2.2
w_{cr}	Laser radius in crystal	Section 3.7.1
$w_{\text{min-M}}$	Minimum laser radius in crystal	Section 3.7.1
w_{00}	TEM_{00} mode radius	Section 6.3.4
w_{p}	Pump radius	Section 3.5
x	Horizontal transverse direction	Section 7.2.1
$< x^1 >$	1^{st} intensity moment	Section 5.2.4
$< x^2 >$	2^{nd} intensity moment	Section 5.2.4
$< x^4 >$	4^{th} intensity moment	Section 5.2.4
Δx	FEA horizontal mesh element	Section 7.2
y	Vertical transverse direction	Section 7.2.1
Δy	FEA vertical mesh element	Section 7.2
z	Propagation direction	Section 3.3
Δz	FEA mesh element prop. direc.	Section 7.2
z_{R}	Rayleigh length	Section 5.2.2
$Z_u^j(\rho,\varphi)$	Zernike polynomial	Section 3.4.4

Chapter 1

Introduction

End-pumped solid-state lasers are compact, efficient and produce good quality laser beams. Before the early 1990s their power output was limited by the amount of pump power available from diode sources and pump beams had to be focused to very small sizes inside the crystal just to reach threshold (Fan & Byer, 1988). The fast emergence of ever higher power diodes solved this problem but also caused new ones to emerge. This is because end-pumping produces very high incident pump power densities of up to 10kW/cm^2. This leads to strong local heating which can cause the crystal to fracture long before the maximum output of the diode is reached. However, fracture is not the only thermal problem limiting laser output. In some materials thermo-optical aberrations severely limit the amount of output power available from good-beam-quality lasers.

Possible approaches to solve the thermal problems are to increase the length of the gain medium and to lower the doping (fibre lasers) or to decrease the width of the gain medium and to increase the doping (thin disk lasers). However, these two laser systems have other limitations. Fibre lasers can not deliver pulses with energy much larger than 10 mJ. Neither can they be intra-cavity frequency doubled due to their high loss/high gain nature. The pump set-up of a thin disk laser is also much more complex and their mode volume is small so that they have limited energy storage. Their low gain is also not optimum for short pulses of high peak power. Bulk end-pumped systems therefore remain the best solution for high pulse energy and frequency doubling applications.

Nd:YVO_4 and Nd:$GdVO_4$ (referred to in this thesis as the vanadates) are naturally birefringent gain materials with high emission cross sections and broad, strong absorptions suitable for diode pumping. This makes them ideal for mode-locked, high repetition rate Q-switched and intra-cavity frequency doubled lasers. Such lasers are widely used for both research and industrial applications. For instance, intra-cavity doubled vanadate lasers are used to pump Ti:Sapphire lasers. Well-known examples of these are the Spectra Physics Millennia (Newport, 2009) and Coherent Verdi (Coherent, 2009) systems.

However, both vanadates have high thermo-optical coefficient (dn/dT) values which causes them to exhibit strong thermal lensing and aberrations. The strong thermal lensing causes resonators to be stable at only certain ranges of pump powers and the aberrations degrade the output power and beam quality. This study will contribute to minimising these negative

influences by solving several specific, usually related problems.

Firstly, we determine **which of the two vanadates has weaker thermal lensing properties** because they compete with each other in the commercial laser market due to the similarity of their spectral properties. Their thermal and thermo-optical properties are therefore the deciding factors which determine which one should be chosen. However, there is still a debate about the relative magnitudes of the dn/dT and thermal conductivities values which determine the strength of the thermal lensing. We therefore directly compare the strength of the thermal lensing (defocus) in two equally low doped crystals of either material. From this we determine that Nd:YVO_4 has slightly weaker thermal lensing which refutes several earlier publications that claimed the opposite (Czeranowsky *et al.*, 2002; Zagumennyi *et al.*, 2003; Ogawa *et al.*, 2005). To our knowledge this is the first systematic study of the thermal lensing in the two vanadates under comparable conditions (the same low doping, dimensions, laser set-up and measurement conditions).

We do so by **developing a novel, more reproducible method to measure the focal length of the thermal lens**. This is because the methods using laser resonators to determine the thermal focal length that are described in the literature do not take the aberrations into account, leading to a substantial error in the thermal focal lengths. In contrast, our method measures the focal length of only the central unaberrated part of the thermal lens by using TEM_{00} beams from matched resonators.

The dn/dT value has a large influence on the thermo-optical effects and it is very important to know its precise value in order to do any thermo-optical calculations. We therefore compare the measured focal lengths of the thermal lens with numerically calculated values in order to **determine which one of Nd:YVO_4's widely varying dn_e/dT values reported in the literature is the correct one**. Our results show that the dn_e/dT value given by Sato & Taira (2007) matches our experimental results the best.

The measurements also indicate that the thermal dioptric power increased non linearly with absorbed pump power. **By using numerical calculations we identify the sources of this nonlinear increase in dioptric power** as the varying spectral output of the diode laser and to a lesser degree end-face bulging of the crystal. Eichenholz & Richardson (1998) and Amarande & Damzen (2006) also reported the nonlinear increase but either did not investigate it further or attributed it to nonlinear heat sources like upconversion.

Lastly, we show that by using low doped vanadate crystals there is almost no difference in thermal lensing during lasing and non-lasing conditions. This indicates that there is little to no upconversion in the crystals. **We therefore find that lower doped vanadate crystals are essential for power-scaling vanadate lasers** even though we did not do a systematic study on this.

1.1 Summary of thesis

In the following chapter we discuss different laser materials as well as their composition, which comprise of a host and dopant material. We then focus on the vanadates and use them to discuss thermal, thermo-optical and spectral properties of laser materials. We specifically consider the debate in the literature about the thermal conductivity and thermo-optical

coefficients. The spectroscopic properties of the vanadates are then compared to each other and lastly, the transition processes that are responsible for the extra thermal energy in laser crystals are identified.

In the third chapter we consider the temperature profiles in end-pumped bulk crystals and examine their optical influence. We discuss the formation of a thermal phase change profile due to both a varying refractive index and end-face bulging of an end-pumped crystal and find that the physical manifestation of this phase change is a spherically aberrated thermal lens inside the gain region and rapidly drops off to zero at the edges of the crystal. The influence of this phase change profile on resonator internal as well as external beams is then discussed.

In the fourth chapter we review different methods to measure the thermal lens focal length of the gain medium. First, we cover methods that utilise the influence of the thermal lens on internal resonator beams. One method utilises quenching flat-flat resonators. We also propose a new internal resonator method that only measures the relatively unaberrated central part of the thermal lens. Secondly, the external probe beam methods are discussed which are especially suited for determining relative differences between thermal lenses under different conditions.

In the fifth chapter we describe our experimental set-up. First we discuss the development of the crystal cooling mounts for improved heat removal efficiency by using new high thermal conductivity silver epoxy. We then consider the practical aspects of our particular pump set-up and how we design for a particular pump profile in the crystal. The basic set-up of an end-pumped system is then discussed. We explain the alignment of the different resonators, followed by the diagnostic set-up. Finally we present the complete experimental set-up we used to measure thermal lenses by means of three different measurement methods.

The sixth chapter contains the experimental results of the three different thermal lens measurement sets. We determine that Nd:YVO_4 has slightly weaker thermal lensing than Nd:$GdVO_4$ for the higher gain π-polarisation. The measurements also indicate that the dioptric power increases non-linearly with absorbed pump power. HeNe probe beam experiments confirm that Nd:YVO_4 has lower thermal lensing for both polarisations at 632.8 nm as well. The probe beam measurements further reveal that there is no change in the thermal lensing between lasing and nonlasing conditions, which indicates that there is almost negligible upconversion in the low doped crystals we used.

In the seventh chapter we combine the experimental results with the results of numerical simulations to determine which of the widely varying dn_e/dT values of Nd:YVO_4 reported in the literature match our measurements the best. The value reported by Sato & Taira (2007) is thus identified and we use it to identify the sources of the nonlinear increase of the dioptric power with absorbed pump power. These sources are the varying spectral output of the diode laser and to a lesser degree end-face bulging. The calculations also show the importance of using a temperature dependent thermal conductivity in thermal calculations. Lastly we present a fracture stress analysis of a low doped Nd:YVO_4 crystal.

In the final chapter we draw the conclusions we reach from this study. We also make suggestions about future research that can be undertaken.

Chapter 2

Laser materials

2.1 Introduction

Laser crystals are selected for various properties in the design of systems, the most important being gain and upper laser level lifetime at the required wavelength. In addition, one has to take into account various other material and spectroscopic properties. We will review the most important design parameters in this chapter.

2.2 Host and dopant materials

Laser crystals consist of a host material that is doped with active ions (the dopant) which replace an ion with the same number of valence electrons. The spectroscopic properties of the laser crystal largely depend on the dopant material, while the host material determines the material properties such as thermal conductivity (k_{th}), refractive index (n), birefringence and hardness. The host and dopant material also influences each others properties.

2.2.1 Host materials

There is a multitude of crystal host materials that can be chosen from to build lasers. One of the oldest available and best studied materials on the market is Yttrium Aluminium Garnet ($Y_3Al_5O_{12}$ or YAG). It is an isotropic material which means that its properties are invariant in all its crystallographic directions.

Other well known host materials are Yttrium (Y), Gadolinium (Gd) and Lutetium (Lu) orthovanadate (YVO_4 and $GdVO_4$ and $LuVO_4$) and Yttrium Lithium Fluoride (YLF). They are all uni-axial, which implies that one of the crystallographic directions has different properties than the other two. The vanadates are known for their high gain while YLF is known for its low thermo optical properties and long upper laser level lifetime (τ_{s}). In this study we specifically focus on YVO_4 and $GdVO_4$. For the sake of brevity, we will only refer to them as the vanadates. In YVO_4 and $GdVO_4$, Y and Gd ions are respectively replaced by active (dopant) ions.

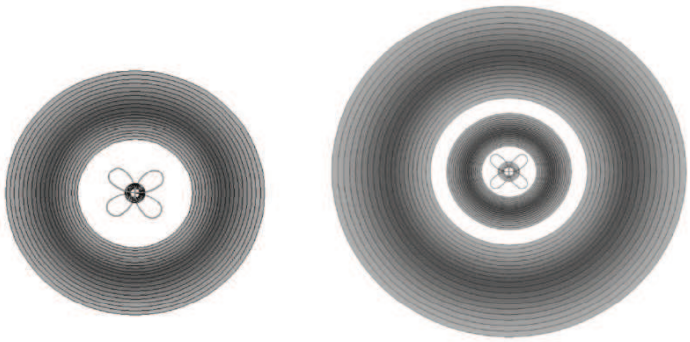

Figure 2.1: Orbital structure of the transition metals (left) and lanthanides (right) (Barnes, 2007). The 3d transition orbitals of the transition metals (in the form of a four leaf clover) are directly exposed to the 4s bonding electrons on the outside. The 4f transition levels of the lanthanides (also in the form of a four leaf clover) are shielded from the crystal field by the circular shaped 5s and 5p orbitals which are between them and the circular 6s orbitals on the outside.

2.2.2 Dopant materials

There are various dopant materials which can generally be divided into two categories, namely the transition metals and the lanthanides. The transition metal active ions are on the fourth row of the periodic table and range from Titanium to Nickel. Lanthanide doping materials (also known as the rare earths) are found on the sixth row of the periodic table and range from Cerium to Ytterbium. We will focus on the lanthanides since they are the most commonly used. More specifically we will consider Neodymium (Nd) which is the most common lanthanide dopant and has strong emission lines at $\sim 1\,\mu$m, $1.3\,\mu$m and $0.900\,\mu$m in order of relative strength. The doubling of these frequencies leads to green, red and blue laser emission respectively. This makes Nd^{3+} doped crystals especially attractive for full colour applications. Other common lanthanides include Holmium (Ho), Erbium (Er) and Thulium (Tm) which are used to obtain $2.1\,\mu$m $1.5\,\mu$m and $1.9\,\mu$m lasers respectively. In this study we use Nd:YVO_4 and Nd:$GdVO_4$ to mostly do experiments at both $1.064\,\mu$m and $1.34\,\mu$m.

The host influences the spectroscopic properties of the dopant by means of the local crystal fields (Koechner, 1999). Its influence on the spectra of the lanthanides is limited because their 4f upper laser levels are shielded by the already filled $5s^2$ $5p^6$ sub-shells which have lower energy but larger orbitals as can be seen on the right sketch in Figure 2.1. The small influence of the lanthanide crystal fields leads to spectrally narrow transitions in emission and absorption (Barnes, 2007). They also perturb the energy levels only slightly, which causes the spectral frequencies of crystals with the same dopant to be similar. This is not true for

the transition metals whose 3d transition levels are not shielded (left sketch in Figure 2.1). The crystal field of the transition metal doped materials therefore has a strong influence on their energy levels and transition rates.

The crystal fields also influence τ_s and the intensity of the emission lines of the lanthanides. A long τ_s is especially important for Q-switched lasers because it determines the energy storage of the crystal (Csele, 2004 pp. 125) while the intensity of emission lines determines the strength of the gain at that wavelength.

2.3 Vanadate material properties

In this section we will discuss the material properties of uni-axial host crystals by using vanadate as example. The general discussions of the properties can therefore be applied to other uni-axial laser crystals like YLF, even though the magnitude and even the sign of some of the values may differ substantially.

2.3.1 Vanadate crystal structure

Both YVO_4 an $GdVO_4$ have a simple tetragonal crystal structure which implies that both are uni-axial and have orthogonal axes. Figure 2.2 shows the crystal structure of either YVO_4 or $GdVO_4$ projected along the *a*-direction on the left, and along the *c*-direction on the right. The red spheres represent Y^{3+} or Gd^{3+} ions and the blue spheres represent VO_4^{3-} ions. Nd^{3+} has a valence of 3+, the same as the Y or Gd ions which it displaces (Koechner, 1999 pp. 29).

Figure 2.2 also shows the unit cell which is the smallest possible volume one can use to reconstruct the entire crystal by stacking them next to, and on top of each other. It can be observed from the ions inside the two marked ovals that the arrangement of the ions repeats at the boundaries of the unit cell in the *c*-direction. The same is true in any other direction as can be visually confirmed in the figure.

One can observe in the right projection in Figure 2.2 that the vertical and horizontal directions are equivalent and are both termed the *a*-direction (Hecht, 1998 pp. 330-340). The horizontal direction in the left projection is different to the other two directions and is labelled the *c*-direction, or the **crystal** optical axis.

By comparing the two projections it is evident that the number of ions in the *a*-direction is less than in the *c*-direction. The lattice constant in the *a*-direction is also larger than in the *c*-direction. The layers perpendicular to the *c*-direction are therefore more densely packed than those perpendicular to the *a*-direction. This causes a number of properties to be different in the *a*-direction and *c*-directions.

2.3.2 Thermal expansion

The shorter intermolecular distances in the *c*-direction lead to a higher thermal expansion coefficient in that direction. This is because the expansion is related to the increasing thermal vibrations of the ions which are higher in the denser *c*-direction (Zhang *et al.*, 1999). Because the *c*-direction expands more, the tensile stresses will also be more in that direction. This

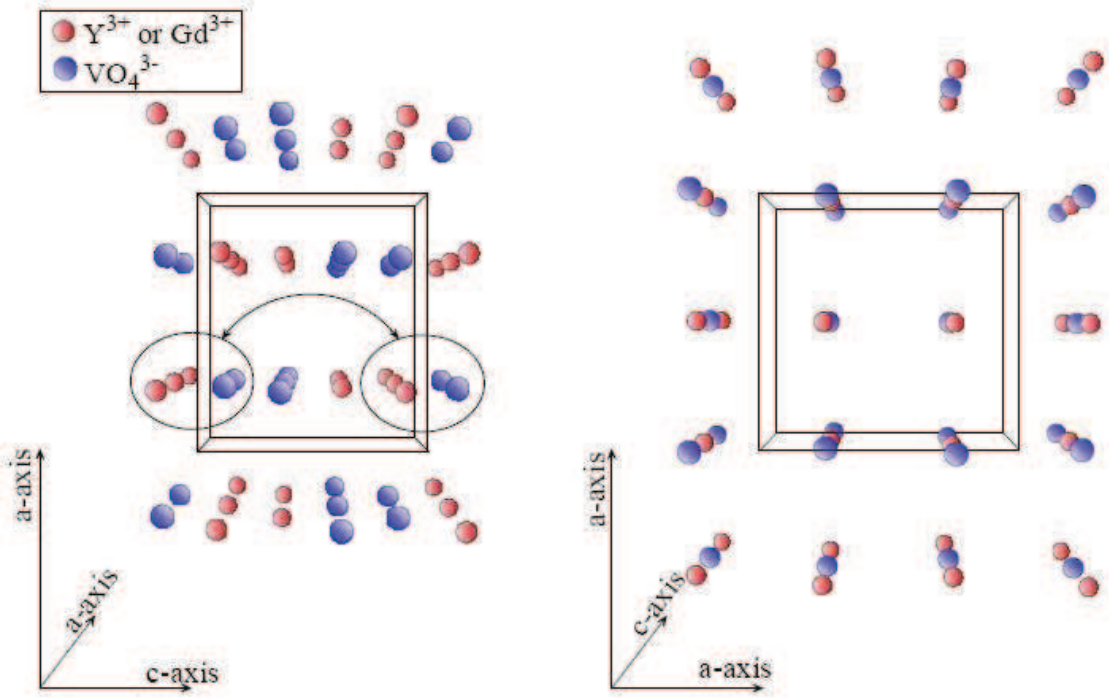

Figure 2.2: The crystal structure of YVO_4 or $GdVO_4$ adapted from Zhang *et al.* (1999). The red spheres represent Y^{3+} or Gd^{3+} and the blue spheres represent VO_4^{3-} ions. The structure on the left is the projection along the *a*-direction. The structure on the right is the projection along the *c*-direction. The unit cell is drawn into both structures.

Property	**Nd:YVO_4**	**Nd:$GdVO_4$**	**Reference**
n_e (c-direc)	2.155	2.190	(Sato & Taira, 2007)
n_o (a-direc)	1.958	1.972	(Sato & Taira, 2007)
$k_{\mathrm{th}-c}$ [W/mK]	$716.32/\mathrm{T}^{0.76766}$	$896.14/\mathrm{T}^{0.78106}$	(Sato & Taira, 2006)
$k_{\mathrm{th}-a}$ [W/mK]	$643.94/\mathrm{T}^{0.69711}$	$821.58/\mathrm{T}^{0.79855}$	(Sato & Taira, 2006)
$\alpha_{\mathrm{th}-c}$ $[\times 10^{-6}K^{-1}]$	8.19	7.89	(Sato & Taira, 2007)
$\alpha_{\mathrm{th}-a}$ $[\times 10^{-6}K^{-1}]$	1.69	1.14	(Sato & Taira, 2007)
E_{YM} [N/mm^2]	133000	133000	(Ma *et al.*, 2007)
ν_{Pois}	0.33	0.33	(Ma *et al.*, 2007)

Table 2.1: Material properties of Nd:YVO_4 and Nd:$GdVO_4$.

also has implications for mounting laser crystals. If the expansion of the crystal is restricted in the c-direction it can lead to increased stresses and premature fracturing.

The rate of expansion is usually constant for a crystallographic direction over the range of temperatures that are found in practice. This constant rate of expansion is called the thermal expansion coefficient α_{th} and is defined as:

$$\frac{\Delta l_{\mathrm{cr}}}{l_{\mathrm{cr}}} = \alpha_{\mathrm{th}} \Delta T \tag{2.1}$$

where ΔT is the temperature increase, l_{cr} is the length before heating and Δl_{cr} is the increase in the length in a specific crystallographic direction due to the heating. The linear thermal expansion coefficients for the vanadates are listed in Table 2.1. Because of the linear expansion a temperature variation inside these crystals causes their end-faces to bulge outwards. We will observe in Section 3.4.5 that this contributes to a thermal lens in laser crystals.

The thermal expansion also creates stresses in the crystals. The stresses ultimately lead to fracture at high pump powers. This fracture limit largely depends on the tensile strength of the material. YAG is extremely strong with a tensile strength of 200 MPa, while vanadate is much weaker with a tensile strength of 53 MPa (Paschotta, 2008). YLF is even weaker with a tensile strength of only 33 MPa (Wetter *et al.*, 2008). It is therefore very difficult to power-scale YLF lasers because the crystals fracture so easily. Various techniques therefore have to be used to limit the stresses in YLF crystals.

2.3.3 Thermal conductivity

The thermal conductivity (k_{th}) is inversely related to the inter-ionic distances. The smaller the distances are the more efficiently heat can be transferred. The heat flow and hence the thermal conductivity will therefore be larger in the c-direction which is more densely packed. This implies that the crystal faces perpendicular to the c-direction must be cooled since they will transport the heat away more efficiently. The dissimilar heat flow in the different crystallographic directions lead to an astigmatic temperature distribution in uni-axial crystals. The thermal conductivity is also slightly dependent on doping. Lower doped crystals have

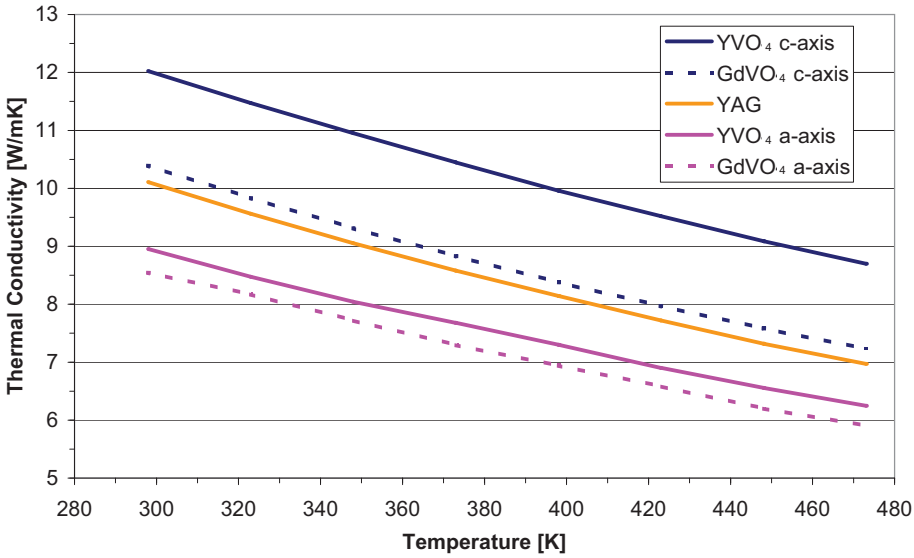

Figure 2.3: The thermal conductivity as a function of temperature for the vanadates and YAG as measured by (Sato & Taira, 2006). Nd:YVO_4 is in blue, Nd:$GdVO_4$ in pink and the isotropic material YAG in yellow. The solid lines were measured in the c-direction and the dotted lines in the a-direction of the uni-axial vanadates.

less distortion in their crystal lattices and therefore have higher thermal conductivities (Sato & Taira, 2006).

The thermal conductivity decreases with temperature because the intermolecular distances increase with temperature which makes energy transfer between ions less efficient (Sato & Taira, 2006). The temperature dependence of the thermal conductivity is often neglected in studies of the temperature effects in laser crystals (Sheldon *et al.*, 1982; Peng *et al.*, 2001; Pfistner *et al.*, 1994; Ma *et al.*, 2007). However, Sato & Taira (2006) showed that the thermal conductivities of the vanadates and YAG vary significantly over the temperature range commonly found in laser crystals. Their results are reproduced in Figure 2.3. Functions fitted through their data are given in Table 2.1 and were used in the numerical calculations in Chapter 7.

2.3.4 Refractive indices and thermo-optical coefficients

The refractive index (n) can not be explained as easily by the crystal structure alone. It requires knowledge about the binding forces between the ions in the crystallographic directions (Hecht, 1998 pp. 330-340).

However, one can expect the denser c-direction to be optically denser and therefore to have a higher refractive index. This is indeed the case for both vanadates. The refractive index in the c-direction is called the extraordinary refractive index (n_e) and the one in the a-directions the ordinary refractive index (n_o). Light polarised along the c-direction ($E \parallel c$) is said to be π-polarised and along the a-directions ($E \parallel a$) σ-polarised (Section 2.3.1). This

$\boldsymbol{E} \parallel \boldsymbol{a}$	$\boldsymbol{E} \parallel \boldsymbol{c}$
n_o	n_e
σ	π

Table 2.2: Polarisation properties.

is briefly summarised in Table 2.2. A crystal is a-cut if one of the a-directions is along the propagation direction of the beam inside the crystal and likewise with c-cut crystals. Both n and its dependence on temperature (dn/dT) also increase slightly with doping concentration (Sato & Taira, 2007).

We will observe in Section 2.5.2 that the laser output of the vanadates has different spectra for the polarisations in the two crystallographic directions. Only one of the polarised laser lines usually oscillates due to a large gain difference between the two. The consequence is that oscillating laser beams experience only a single refractive index. The extraordinary refractive index can therefore not be varied between the values of n_o and n_e for resonator modes as can be done for external beams (Hecht, 1998 pp. 330-340).

The variation of the refractive index with temperature is a very important temperature effect in bulk crystal solid state lasers. This is because a refractive index profile inside the crystal leads to the formation of an aberrated, pump power dependent thermal lens. This thermal lens can cause resonators to be stable for only certain pump power ranges. It also introduces losses inside the resonator that can act as soft aperture, reduce the beam quality and decrease the output power. We discuss thermal lensing and aberrations in detail in Chapter 3.

Both refractive indices usually vary linearly over the range of temperatures found in laser crystals. This constant rate of change is known as the thermo-optical coefficient dn/dT. The dioptric power of the thermal lens mentioned earlier is roughly directly related to the thermo-optical coefficient (Section 5.2.2). dn/dT is high and positive for the vanadates and YAG, while it is low and negative in YLF. It is also different for the different crystallographic directions in non-isotropic crystals like YVO_4, $GdVO_4$ and YLF (dn_e/dT and dn_o/dT). In the next section we show that there is some debate over the values of dn_e/dT of both vanadates in the literature.

The refractive index also changes with wavelength due to dispersion, which is an interplay of various electric polarisation mechanisms contributing at a particular frequency (Hecht, 1998 pp. 67). The empirical relationship between refractive index and wavelength for a transparent medium is known as the Sellmeier equation. It can be given by (Shen *et al.*, 2004)

$$n^2(\lambda, T) = \mathrm{A}_n(T) + \frac{\mathrm{B}_n(T)}{\lambda^2 - \mathrm{C}_n(T)} - \mathrm{D}_n(T)\lambda^2. \tag{2.2}$$

This is a modified version of the original equation which is longer and includes more coefficients (Malitson, 1965). The Sellmeier coefficients A_n to D_n are different for the two polarisations of the uni-axial materials and are listed in Table 2.3 for Nd:YVO_4 (Shi *et al.*, 2001) and Nd:$GdVO_4$ (Shen *et al.*, 2004) at 20°C.

Sellmeier coefficients	**Nd:YVO_4 *c*-direction** [K^{-1}]	**Nd:YVO_4 *a*-direction** [K^{-1}]	**Nd:$GdVO_4$ *c*-direction** [K^{-1}]	**Nd:$GdVO_4$ *a*-direction** [K^{-1}]
A_n	4.6072	3.77879	4.70852	3.82356
B_n	0.10809	0.07405	0.11547	0.07575
C_n	0.06250	0.04573	0.05014	0.03954
D_n	0.01431	0.00970	0.01031	0.00515

Table 2.3: Sellmeier coefficients of both Nd:YVO_4 and Nd:$GdVO_4$ for both polarisations at 20°C.

Nd:YVO_4 dn_e/dT (c-direc.)	**Nd:YVO_4 dn_o/dT** (a-direc)	**Nd:$GdVO_4$ dn_e/dT** (c-direc.)	**Nd:$GdVO_4$ dn_o/dT** (a-direc)	**Source**
1.0498×10^{-5}	1.6592×10^{-5}	NA	NA	(Shi *et al.*, 2001)
7.92×10^{-6}	NA	1.01×10^{-5}	1.38×10^{-5}	(Sato & Taira, 2007)
3.9×10^{-6}	8.50×10^{-6}	NA	NA	(Bermudez *et al.*, 2002)
3.0×10^{-6}	8.5×10^{-6}	4.7×10^{-6}	NA	(Castech, 2008)
NA	NA	9.3×10^{-6}	13.6×10^{-5}	(Shen *et al.*, 2004)

Table 2.4: dn/dT coefficients of both Nd:YVO_4 and Nd:$GdVO_4$ for both polarisations at 1.064 μm as published in various sources.

The dn/dT values are also dependent on wavelength. In most cases $dn_e/dT(\lambda)$ is higher at lower wavelengths. Thermal lensing in a crystal will therefore be stronger for a HeNe laser at 632.8 nm than for a 1 μm laser.

2.4 The vanadate debate

Various dn/dT coefficients at 1.064 μm of both Nd:YVO_4 and Nd:$GdVO_4$ are available in the literature. The most recent value for the important c-direction of Nd:YVO_4 as reported by Sato & Taira (2007) is 7.92×10^{-6}. This is more than twice the value of 3.00×10^{-6} that is normally provided by manufacturers (Castech, 2008). Other values for both polarisations of the vanadates that are also available in the literature are listed in Table 2.4. The confusion over which value to use is of some concern since the dn/dT coefficient is the most important contributor to the thermal lens effect in vanadates. What is clear from observing all the data sets is that in both materials dn_o/dT is much larger than dn_e/dT which implies that the σ-thermal lens is stronger.

There is also debate on the thermal conductivity of the two vanadates. Until recently, it was thought that the newer and more expensive $GdVO_4$ has almost double the thermal conductivity of YVO_4. According to the heat flow equation (Peng *et al.*, 2001), less heat would build up inside the crystal which leads to a lower peak temperature. A significant number of publications assumed this and reported high output powers from Nd:$GdVO_4$ lasers (Liu

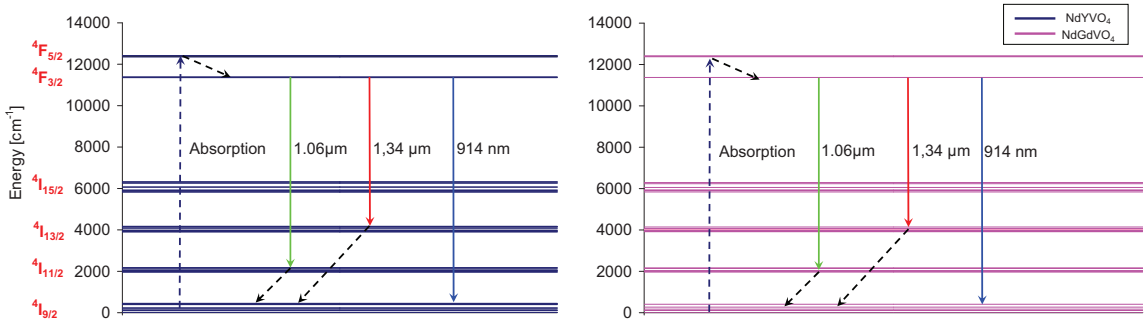

Figure 2.4: The laser energy levels and transitions of Nd:YVO_4 and Nd:$GdVO_4$ (data obtained from Anderson *et al.*, 1994).

et al., 1999; Zagumennyi *et al.*, 2003; Du *et al.*, 2004; Saikawa *et al.*, 2005). However, their results did not reflect the twofold higher thermal conductivity. Gd is also larger than Y and should theoretically lead to $GdVO_4$ having a lower thermal conductivity than YVO_4 because it perturbs the crystal structure more. Recently, Sato & Taira (2006) accurately re-measured the thermal conductivity and its dependency on temperature of both materials with the quasi-one-dimensional flash method. They found that the thermal conductivity of Nd:YVO_4 was much higher than was initially measured. In fact, their measured values indicated that it was even higher than that of Nd:$GdVO_4$. The reason for this is probably that the original measurements of the thermal conductivity of Nd:YVO_4 were performed in the 1970s with samples that had more impurities than the crystals that are available today (Koechner, 1999 pp. 63).

There is therefore a great deal of confusion in the literature over which material has the best thermal and thermo-optical properties. One of the main aims of this study is to compare the lasing and thermo-optical properties of Nd:YVO_4 and Nd:$GdVO_4$ and their polarisations under almost identical pump and laser conditions. In the next section we review the spectroscopic properties of the vanadates which make them such attractive materials for diode pumped lasers.

2.5 Vanadate spectroscopic properties

Figure 2.4 shows the laser energy levels and laser transitions of both Nd:YVO_4 (left) and Nd:$GdVO_4$ (right) on a single energy level diagram. It is significant that the energy levels are almost identical, since Gd's average atomic weight is almost twice that of Y. It could be expected that $GdVO_4$ would have a much larger influence on the energy levels of the Nd^{3+} dopant because the hosts valence electrons are in an orbital with a much higher energy. The reason for the similarity is that the nearest neighbours to the Nd^{3+} ions are O^{2-} ions, which are the same in the structures of the two crystals (Anderson *et al.*, 1994). Y and Gd therefore only have a small influence on the energy levels of Nd^{3+}. In the next two sections we discuss the various transition processes that occur between the Nd^{3+} energy levels.

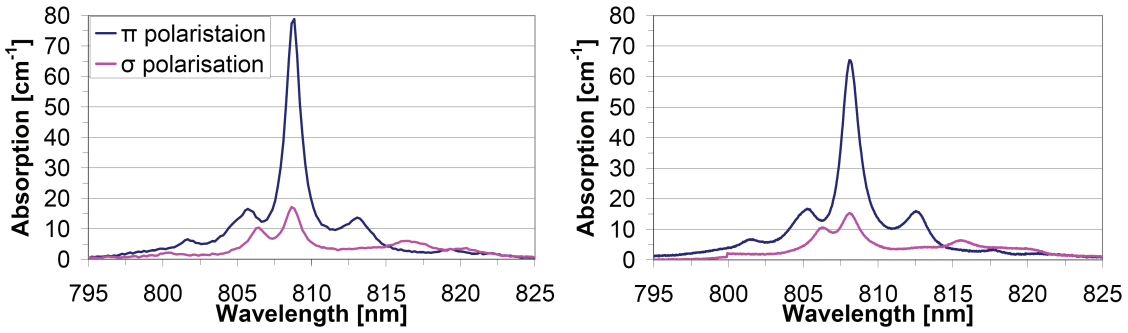

Figure 2.5: Absorption of the π-polarisation (blue) and σ-polarisation (pink) of Nd:YVO_4 on the left and Nd:$GdVO_4$ on the right (Cross, 2004).

2.5.1 Absorption

Figure 2.5 shows the absorption spectra ($\alpha_{\text{abs}-a,c}(\lambda)$) of Nd:$YVO_4$ and Nd:$GdVO_4$ around 808 nm (Cross, 2004). The absorption spectra for both polarisations look very similar as was expected from their almost identical energy levels. Nd:YVO_4 only has a slightly higher maximum absorption peak at a slightly longer wavelength.

The most common way to pump Nd:vanadate is to use pump light with a wavelength of around 808 nm. From Figure 2.4 it can be observed that such photons pump electrons in the $^4I_{9/2}$ level to the $^4F_{5/2}$ level (Ermeneux *et al.*, 1999). The electrons in the $^4F_{5/2}$ level then decay to the $^4F_{3/2}$ upper laser level. One can also pump electrons directly into the upper laser level by using a pump wavelength of 880 nm (Saikawa *et al.*, 2005). However, pump sources at these wavelengths are less common and are more expensive. We will therefore concentrate on pump sources at 808 nm which were also what we employed.

The absorption curve of a diode laser in a vanadate crystal is found by taking the convolution of the diode laser spectra with the absorption curves of Figure 2.5 over the range of wavelengths in which the diode laser operates. The convolution of these two spectra then leads to a much broader laser diode absorption spectrum. An explanation of the convolution process and the resulting diode laser absorption spectra can be found in Section 7.2.6.

2.5.2 Stimulated emission

The $^4F_{5/2}$ level has a lifetime of only 19 ps and rapidly decays into the upper laser level $^4F_{3/2}$. The lifetimes of this level for both Nd:YVO_4 and Nd:$GdVO_4$ are 90 μs and 83.4 μs respectively (Anderson *et al.*, 1994). This is relatively short compared to Nd:YAG (230 μs) and Nd:YLF (520 μs) which implies that Nd^{3+} vanadate is not the most suitable material for low repetition Q-switched high energy pulsed lasers due to its limited energy storage (Csele, 2004 pp. 125).

The ions in the upper laser level can then undergo stimulated emission to three lower laser levels. The first two levels to which it can radiate according to transition probability are the $^4I_{11/2}$ and $^4I_{13/2}$ levels with output wavelengths of 1.064 and 1.34 μm respectively (Figure 2.4). These are also referred to as the Neodymium 1 and 1.3 μm lines and both are

Source	1 μm π	1 μm σ	1.3 μm π	1.3 μm σ	900 nm π	900 nm σ
Nd:YVO_4	123	52	32	13	4, 84	4, 3
Nd:$GdVO_4$	125	61	33	24	6, 6	5, 6
Nd:YLF	22	14	3	3	1, 2	1, 3
Nd:YAG	29	29	7	7	3, 9	3, 9

Table 2.5: The stimulated emission cross sections for the strongest lines of a few 1% Nd^{3+} doped laser materials in units of $\times 10^{-20}cm^2$ (Czeranowsky, 2002).

four-level processes. The other transition is to the lower pump level $^4I_{9/2}$, which has an output wavelength of 912-915 nm depending on the crystal type and polarisation. This is also known as the Neodymium 900 nm line and is a quasi-three level process. The stimulated emission cross sections for the strongest lines of these transitions can be found in Table 2.5 in units of $\times 10^{-20}cm^2$ (Czeranowsky, 2002 pp. 10-11). The two vanadates have similar cross sections for all three transitions and are significantly higher than those of YLF and YAG. This makes vanadate the ideal choice for high-power CW, intra-cavity doubled lasers (Koechner, 1999 pp. 64). They are also suited for passively mode-locked lasers because their high gain compensates for their short upper laser level lifetimes.

Table 2.5 also indicate that for uni-axial crystals the emission is two in the different crystallographic directions. The π-polarisation is stronger in both the vanadates and YLF. Lasers built with these crystals will therefore preferentially oscillate on the π-polarisation in the absence of other effects that create a bias for the σ-polarisation. This makes the output of uni-axial crystals linearly polarised along one of their crystallographic directions.

2.5.3 Heat generation in crystals

Heat generation in crystals can be attributed to a number of transition processes. The most common source of heat in laser crystals is the quantum defect. There are also processes involving higher energy levels which can add to the heat load of laser crystals. The two processes that predominate in Nd^{3+} doped materials are excited-state absorption and Auger upconversion. In the next few sections we discuss these heat generation processes in detail because we will focus on the effect that extra heat has on laser crystals and resonators in the rest of this thesis.

2.5.4 The quantum defect

The quantum defect is caused by the energy difference between the energy of the pump and lasing photons. The energy difference between the two is converted to heat and transferred to the crystal structure as phonons. For vanadate lasers that are pumped at $\sim$ 808 nm and operate on the 1 μm, 1.3 μm and 900 nm lines the quantum defect is $\sim$24%, 40% and 12% respectively.

The quantum defect is a significant contributor to the heat load for the 1 μm and 1.3 μm lines because of the large non-radiative transitions from the $^4I_{11/2}$ and $^4I_{13/2}$ lower laser levels

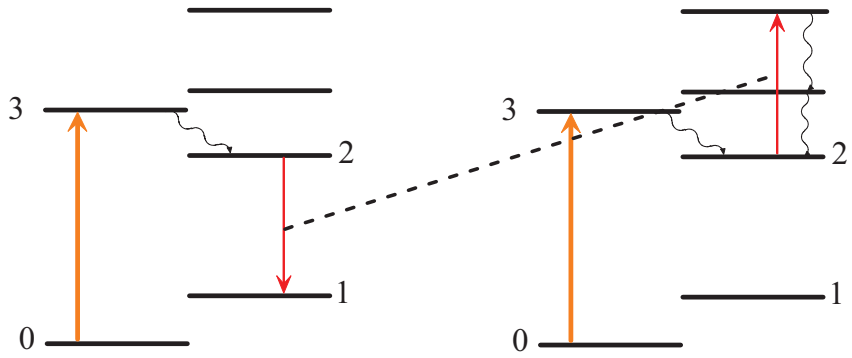

Figure 2.6: Auger upconversion in a four-level laser material.

to the $^4I_{9/2}$ ground state respectively (Figure 2.4). At 1.34 μm operation the population of the $^4I_{13/2}$ level is high because of stimulated emission to it. Significantly more heat is therefore generated within the crystal during 1.34 μm lasing than during non-lasing or lasing at the other wavelengths. In Section 2.5.6 it will be observed that excited state absorption is also significant at this wavelength and has the same effect. The $^4F_{5/2}$ to $^4F_{3/2}$ transition generates extra heat for all three processes when 808 nm pump light is used. However, its contribution is small compared to the other two non-radiative transitions. The three level 900 nm transition therefore have the the lowest heat generation from the quantum defect.

2.5.5 Auger upconversion

Auger upconversion, also just referred to as upconversion, is a process between two close lying neighbouring active ions that are both in the upper laser level and is illustrated for a general four-level material in Figure 2.6. One of these active ions transfers its energy to the other which is excited into an even higher level. The ion in the higher level then decays radiatively and non-radiatively back to the upper laser level or lower energy levels. An ion in the upper laser level is therefore lost and its energy converted into heat, infra-red and visible radiation.

Active ions that are in the $^4F_{3/2}$ level can "down-convert" to any of the three lower laser levels (Figure 2.4) and transfer their energy to a number of higher lying levels (Chen *et al.*, 2000). A complete energy level diagram of all possible upconversion processes in Nd:YVO_4 can be found in Wang & Song (2007).

Upconversion is highly dependent on doping concentration. By increasing the doping concentration the average distance between active ions is effectively decreased, which increases the probability of energy transfer between them. Upconversion is also dependent on the number of active ions in the $^4F_{3/2}$ upper laser level and is therefore indirectly dependent on which transition stimulated emission takes place, since the inversion density is clamped at the lasing threshold. This can become significant for the 1.34 μm and 914 nm transitions

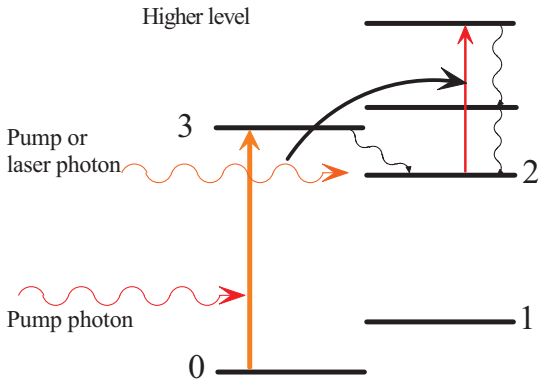

Figure 2.7: Excited-state absorption of a pump or laser photon in a four-level laser material.

because they have lower gain and therefore higher thresholds (Chen *et al.*, 1999). This also implies that heat generated by upconversion can become severe under non-lasing conditions since the inversion is not clamped (Blows *et al.*, 1998). In such cases an interruption of the lasing process in highly pumped crystals can lead to fracture of the laser crystal due to the extra generated heat.

From the characteristics discussed above it follows that we can identify upconversion by higher fluorescence (luminosity) in the crystal during **non-lasing** conditions as well as a temperature **decrease** during **lasing** conditions.

2.5.6 Excited state absorption

In some materials there are higher energy levels (above level 3) present which have an energy difference between them and the upper laser level (excited state) that is very close to either the pump or laser photon energies. Laser or pump photons are absorbed and the energy of some of the active ions in the upper laser level is raised to this higher level. The ions in the higher level then decay radiatively and non-radiatively back to the upper or lower laser levels. A pump or laser photon is therefore lost and extra heat is generated within the crystal. This process is called excited state absorption (ESA) and is illustrated for general four-level materials in Figure 2.7.

ESA is especially problematic in vanadate lasers that operate at 1.34 μm. Ions in the $^4F_{3/2}$ upper laser level absorb the 1.34 μm laser radiation which increases their energy to the $^4G_{7/2}$ level (Okida *et al.*, 2005). This level then decays both radiatively and non-radiatively back to the upper laser level or to the lower laser levels. The large energy differences between the lower laser levels and the $^4G_{7/2}$ level imply that ESA is observed by an increase in visible radiation emanating from the crystal **during** 1.34 μm operation. The temperature also increases during 1.34 μm operation due to non-radiative decay from the $^4G_{7/2}$ level. This causes a hysteresis of the threshold for resonators that are only stable for certain ranges of pump powers (Section 3.7.1).

From the characteristics discussed above it follows that excited state absorption manifests itself by **increased** temperature and fluorescence (luminosity) in the crystal during **lasing**

conditions.

2.6 Conclusion

In this chapter we investigated the material and spectroscopic properties of vanadate laser crystals. An examination of Nd:YVO_4 and Nd:$GdVO_4$ revealed that there is much confusion in the literature over the values of their respective thermal and thermo-optical properties. The spectroscopic properties of the two vanadates were also found to be very similar. Finally, we identified the processes that generate extra heat inside vanadate crystals during lasing and nonlasing operation. In the next chapter we will investigate the effects of this extra heat load on laser beams.

Chapter 3

Thermal effects

3.1 Introduction

All optically pumped laser crystals exhibit at least some thermal effects due to the extra heat that is generated from the various transition processes discussed in the previous chapter. The main thermal effects in solid state lasers are thermal lensing, thermal aberrations, depolarisation and stresses which ultimately lead to fracture. In this chapter we examine the causes and effects of these mostly undesirable processes.

3.2 Pumping and cooling of laser crystals

3.2.1 Cooling of laser crystals

There are various methods to cool laser crystals. Most methods remove excess heat by using some sort of heat transferring material between the crystal and a water cooled heat sink. The most common cooling method is side-cooling where some or all surfaces that are parallel to the propagation direction (z) are cooled (Mudge *et al.*, 1997). A less common method is face-cooling which involves cooling the optical surfaces that are perpendicular to the propagation direction. It is normally used for very thin crystals like thin disk lasers (Stewen *et al.*, 2000). In this study we utilised side-cooling and the technique we used is described in more detail in Section 5.1.2.

3.2.2 Pumping schemes

The most popular methods to pump laser crystals are side and end-pumping. This also includes hybrid methods like thin disk and slab laser designs. With side-pumping any optical pump source is used to illuminate the crystal volume through the cooled side surfaces. In an end-pumped scheme a laser beam is focused into a crystal through the optical surfaces and so preferentially illuminate the mode volume of the resonator. Side-pumping is mainly used for very high output power lasers while end-pumping is used to build highly efficient lasers with good beam quality. We only employed end-pumping in this study and the next few sections will therefore only concentrate on its effects.

3.3 Heat flow in side-cooled end-pumped laser crystals

This section focusses on the heat flow and temperature in side-cooled continuous wave (CW) end-pumped bulk crystals which are either cylindrically or square cut. The crystals are pumped on one or both of their round or square faces and the pump light is absorbed along the z-direction in which the crystal is usually longer. One can expect that the temperature would be highest on the optical axis and that it would decrease along the length of the crystal as the pump light is absorbed.

The 3D temperature profile can be found by solving the general steady state differential heat equation

$$k_{\mathrm{th},x}(T)\frac{\partial^2 T}{\partial x^2} + k_{\mathrm{th},y}(T)\frac{\partial^2 T}{\partial y^2} + k_{\mathrm{th},z}(T)\frac{\partial^2 T}{\partial z^2} = -Q_{\mathrm{th}}(x,y,z). \tag{3.1}$$

where $k_{\mathrm{th},x,y,z}(T)$ are the temperature dependent thermal conductivities in the horizontal, vertical and propagation directions and $Q_{\mathrm{th}}(x,y,z)$ is the heat source density (Chen *et al.*, 2009). This equation is often numerically solved by means of finite element analysis (FEA) but has also been analytically solved by keeping the thermal conductivity independent of direction and temperature. For cylindrical isotropic crystals with a temperature independent thermal conductivity Equation 3.1 reduces to

$$\frac{1}{r}\frac{\partial}{\partial r}(r\frac{\partial T}{\partial r}) + \frac{\partial^2 T}{\partial z^2} = -\frac{Q_{\mathrm{th}}(r,z)}{k_{\mathrm{th}}}. \tag{3.2}$$

The boundary conditions of this problem is that the heat flux from each of the rods surfaces is normal to the surface and proportional to the temperature increase of the surface above the ambient temperature. The heat flow from the end faces into the surrounding air is a few orders of magnitude smaller than that of the actively cooled side surfaces (Farrukh *et al.*, 1988). This implies that the heat flows mainly in the radial direction so that the heat flow in the axial z-direction can be ignored. This further reduces Equation 3.2 to

$$\frac{1}{r}\frac{\partial}{\partial r}(r\frac{\partial T}{\partial r}) = -\frac{Q_{\mathrm{th}}(r,z)}{k_{\mathrm{th}}}, \tag{3.3}$$

which implies that the crystal is divided into thin slices in the z-direction which are temperature independent of each other (Chenais *et al.*, 2004). This equation will be solved for two well known pump profiles in Section 3.5.

3.4 Thermally induced phase change

In the next few sections we discuss how an arbitrary temperature profile in and end-pumped crystal produces a phase change profile for transiting beams.

3.4.1 Phase change due to the refractive index profile

The refractive index of a specific polarisation varies inside the crystal because it is temperature dependent. It was observed in the previous chapter that the dn/dT coefficient is a constant

for a specific wavelength and polarisation (Section 2.3.4). The refractive index profile in the crystal is therefore given by

$$n(r,z) = \frac{dn}{dT}\Delta T(r,z) + n_{\text{unp}}, \tag{3.4}$$

where $\Delta T(r,z)$ is the temperature increase profile due to the heat load and n_{unp} is the constant refractive index of the un-pumped crystal.

The differential phase change at a specific distance r from the optical (propagation) axis in a thin slice dz is directly proportional to the refractive index profile $n(r,z)$ and is given by

$$\frac{d}{dz}\Delta\phi_{\frac{dn}{dT}}(r,z) = \frac{2\pi}{\lambda}n(r,z). \tag{3.5}$$

The differential phase change profile can thus be directly derived from the temperature increase profile using to Equation 3.4

$$\frac{d}{dz}\Delta\phi_{\frac{dn}{dT}}(r,z) = \frac{2\pi}{\lambda}\left(\frac{dn}{dT}\Delta T(r,z) + n_{\text{unp}}\right). \tag{3.6}$$

The total phase change due to the refractive index variation is then found by integrating Equation 3.6 over the length of the crystal (l_{cr}) so that

$$\Delta\phi(r)_{\frac{dn}{dT}} = \frac{2\pi}{\lambda}\frac{dn}{dT}\int_0^{l_{\text{cr}}}\Delta T(r,z)dz + \frac{2\pi}{\lambda}n_{\text{unp}}l_{\text{cr}}. \tag{3.7}$$

The second term is a constant offset due to the refractive index of the un-pumped crystal and can be ignored in the thermal analysis. The integration in the first term can be performed by taking into account the pump divergence and absorption. However, pump beams are usually collimated and are strongly absorbed within laser crystals. This implies that the integrated refractive index phase change often will have a profile that is similar to that of the differential phase change.

3.4.2 Phase change due to the end-face bulging

Most materials expand when heated. The pump-faces do not expand uniformly but bulge more in the centre because the temperature is usually highest there. The phase change of any curved dielectric interface can be found by means of the sag function $\Delta S_{\text{sag}}(r)$ which is the difference between the displacement at a distance r from the optical axis and the displacement of the crystal edge. In Figure 3.1 the sag function of the bulging curve is given by

$$\Delta S_{\text{sag}}(r) = d(r) - d(R_{\text{cr}}) \tag{3.8}$$

and the resulting phase change profile by

$$\Delta\phi_{\text{bg}}(r) = \frac{2\pi}{\lambda}(n-1)\Delta S_{\text{sag}}(r). \tag{3.9}$$

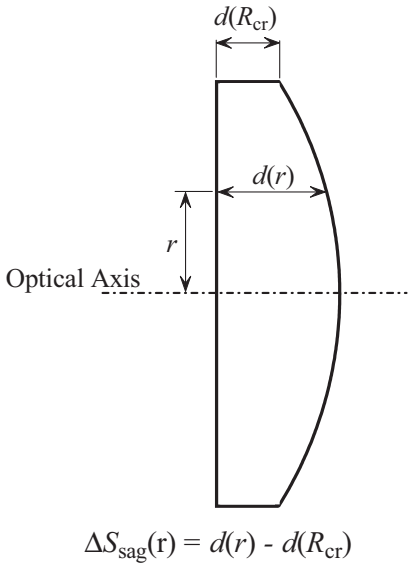

Figure 3.1: Calculation of the sag function of a curved dielectric surface.

If the plane stress approximation is used the phase change from the end-face bulging of a laser rod is given by (Chen *et al.*, 1997)

$$\Delta\phi_{\mathrm{bg}}(r) = \frac{2\pi}{\lambda}(n-1)(\nu_{\mathrm{Pois}}+1)\int_0^{l_{\mathrm{cr}}} \Delta T(r,z)dz. \tag{3.10}$$

The error of using this approximation is usually less than 10%. One of the implications of this error is that the bulging does not increase linearly with pump power as we will show with numerical finite element analysis calculations in Section 7.4.2.

3.4.3 The total phase change due to thermal effects

The total thermal phase change profile from the crystal is obtained by adding together the phase change profiles from the varying refractive index (Equation 3.7) and end-face bulging (Equation 3.9) so that

$$\Delta\phi_{\mathrm{tot}}(r) = \Delta\phi_{\frac{dn}{dT}}(r) + \Delta\phi_{\mathrm{bg}}(r) \tag{3.11}$$

$$= \frac{2\pi}{\lambda}\left(\frac{dn}{dT}\int_0^{l_{\mathrm{cr}}} \Delta T(r,z)dz + \Delta S_{\mathrm{sag}}(r)\right). \tag{3.12}$$

By inserting Equation 3.10 we find that

$$\Delta\phi_{\mathrm{tot}}(r) = \frac{2\pi}{\lambda}\left(\frac{dn}{dT} + (n-1)(\nu_{\mathrm{Pois}}+1)\right)\int_0^{l_{\mathrm{cr}}} \Delta T(r,z)dz. \tag{3.13}$$

In the vanadates the two parts reinforce each other to form a strong positive thermal phase change. In YLF the phase change caused by the integrated varying refractive index of the

σ-polarisation is negative ($dn_o/dT < 0$) and of the same order as the positive phase change caused by the bulging (Hardman *et al.*, 1999). The two contributions therefore almost cancel each other out, thus giving the σ-polarisation of YLF a very weak thermal phase change.

3.4.4 Expanding the phase change profile

The thermally induced phase or the differential phase change profiles in the two orthogonal directions can be expanded in order to analyse them. They can simply be fitted by the even power series Seidel function

$$\Delta\phi(r) = C_{\mathrm{sl}} + A_{\mathrm{sl}} r^2 + B_{\mathrm{sl}} r^4 + ... \tag{3.14}$$

where C_{sl}, A_{sl} and B_{sl} are defined as the Seidel piston, defocus and spherical aberration coefficients respectively (Wyant & Creath, 1992). A_{sl} and B_{sl} depend on the maximum radius (or aperture) to which the data is fitted. However, the Seidel polynomials are not orthogonal. The magnitude of B_{sl} will therefore depend on the magnitude of A_{sl} as well as on potential extra higher order terms like $D_{\mathrm{sl}} r^6$.

In order to avoid this, an orthogonal set of polynomials can be used to expand the optical phase profile. Such a set is the Zernike polynomials. The even ones are defined as

$$Z_u^j(\rho\varphi) = R_u^j(\rho)\cos(j\varphi) \tag{3.15}$$

and the odd ones as

$$Z_u^{-j}(\rho\varphi) = R_u^j(\rho)\sin(j\varphi), \tag{3.16}$$

where u and j are positive integers with $u \geq j$, φ is the azimuthal angle in radians and $\rho = r/a_z$ is the normalised radial distance (Wyant & Creath, 1992). a_z is called the Zernike radius which is the aperture within which the Zernike coefficients are calculated. The radial Zernike polynomials are defined as

$$R_u^j(\rho) = \sum_{h=0}^{(u-j)/2} \frac{(-1)^k (u-h)!}{h![\frac{1}{2}(u+j)-h]![(u-j)-h]!}\rho^{u-2h} \qquad \text{for } u-j = \text{ even} \tag{3.17}$$

and 0 for $u-j =$ odd. For $j = 0$ the even definition is used. Table 3.1 lists a selection of some of the more important Zernike polynomials. Some of these are also plotted in Figure 3.2 as 3D surface graphs.

A 2D phase function can be expanded with the Zernike polynomials by determining the relative weight coefficients of each of the Zernike polynomials. These coefficients can be found by using the normalised phase function $\phi(a_z\rho, \varphi)$ in the integral

$$A_u^j = (u+1)/\pi \int_0^{2\pi}\int_0^1 \phi(a_z\rho,\varphi) Z_u^j(\rho,\varphi)\cos(j\varphi)\, d\rho d\varphi. \tag{3.18}$$

The Zernike expansion enables us to make determinations on the relative magnitude of the different higher order aberrations due to the orthogonality of the Zernike polynomials.

u	j	$Z_u^j(\rho\varphi)$	**Aberration**
0	0	1	Piston
1	-1	$\rho\sin\varphi$	Tilt-Y
1	1	$\rho\cos\varphi$	Tilt-X
2	-2	$\rho^2\sin 2\varphi$	Astigmatism-Y
2	0	$2\rho^2-1$	Defocus
2	2	$\rho^2\cos 2\varphi$	Astigmatism-X
3	-3	$\rho^3\sin 3\varphi$	Trefoil-Y
3	-1	$(3\rho^3-2\rho)\sin\varphi$	Coma-Y
3	1	$(3\rho^3-2\rho)\cos\varphi$	Coma-X
3	3	$\rho^3\cos 3\varphi$	Trefoil-X
4	-4	$\rho^4\sin 4\varphi$	Quadrafoil-Y
4	-2	$(4\rho^4-3\rho^2)\sin 2\varphi$	5^{th} order Astigmatism-Y
4	0	$6\rho^4-6\rho^2+1$	Spherical aberration
4	2	$(4\rho^4-3\rho^2)\cos 2\rho$	5^{th} order Astigmatism-X
4	4	$\rho^4\cos 4\rho$	Quadrafoil-X
5	-5	$\rho^5\sin 5\varphi$	Pentafoil-Y
6	0	$20\rho^6-30\rho^4+12\rho^2-1$	5^{th} order Spherical Aberration

Table 3.1: A selection of some of the more important Zernike polynomials and the aberrations that they quantify.

However, it is not as intuitive as the Seidel expansion since individual Zernike polynomials tend to fluctuate around the phase profile that is expanded. We therefore chose to use a Seidel expansion for illustrative qualitative purposes and the Zernike expansion for quantitative analysis.

3.4.5 Spherically aberrated thermal lensing

The r^2 term of Equation 3.14 and the Z_2^0 polynomial are both associated with a lensing effect. In order to explain this it is noted that the phase change of a perfect thin lens is given by

$$\Delta\phi_{\text{lens}}(r) = -\frac{k_\lambda}{2f}r^2, \tag{3.19}$$

where f is its focal length and k_λ is the wave number $2\pi/\lambda$. This relation is derived from geometrical considerations and the binomial approximation for a spherical lens. The phase change of a perfect lens is thus strictly quadratic. By comparing Equations 3.14 and 3.19 it is evident that $A_{\text{sl}} = \pi/\lambda f$. The quadratic part of the thermal phase change is therefore equivalent to a thin lens of focal length

$$f_{\text{th}} = -\frac{\pi}{\lambda A_{\text{sl}}}. \tag{3.20}$$

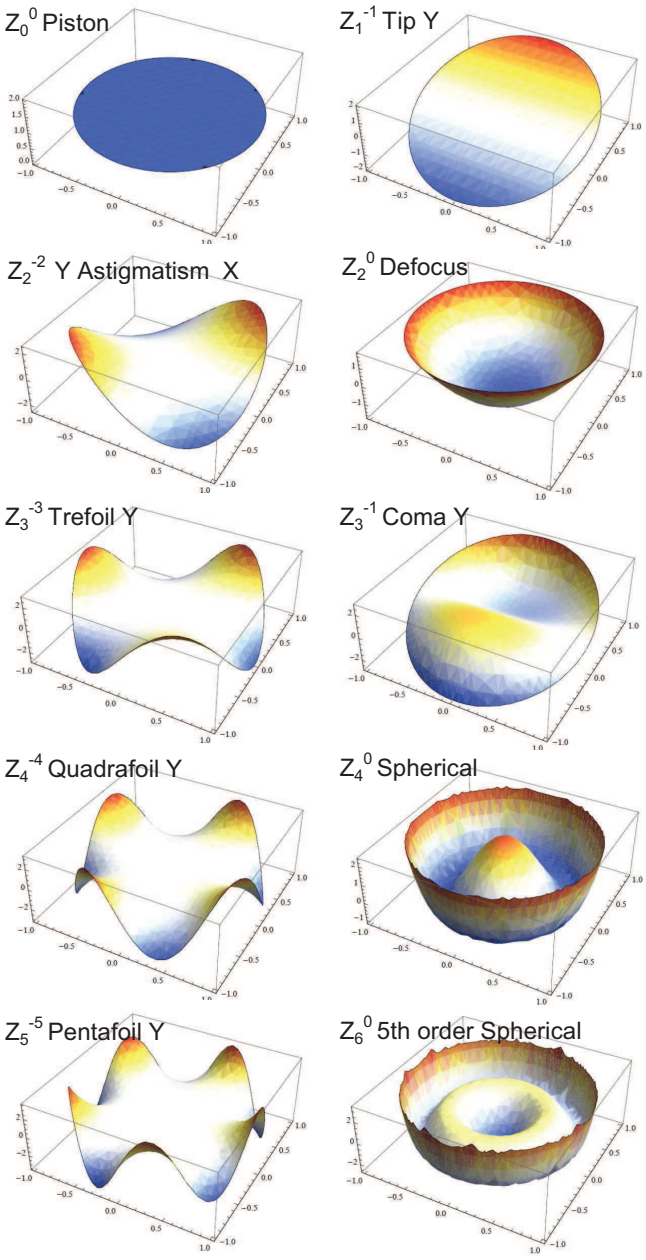

Figure 3.2: A selection of some of the more important Zernike polynomials plotted as 3D surface graphs calculated with Mathematica (Mathematica, 2008).

Similarly, by using the defocus Zernike coefficient A_2^0, the focal length of the thermal lens can be shown to be equal to

$$f_{\text{th}} = -\frac{k_\lambda \pi a_z^2}{4A_2^0}. \tag{3.21}$$

Equations 3.21 and 3.20 are equivalent and both can be used to determine the focal length of the thermal lens using either the Seidel or Zernike expansions.

The r^4 term in Equation 3.14 and the Z_4^0 Zernike polynomial is associated with spherical aberration. Spherical aberration is well known in optics and astronomy (O'Donoghue, 2000) and it has adverse effects on beams inside and outside resonators. Some of these effects are discussed in Sections 3.7.2 and 3.8.

Only the Zernike A_4^0 coefficient is a good measure of the amount of spherical aberration in a given phase profile. The phase becomes less quadratic further away from the optical axis which is referred to as negative spherical aberration (Pu, 1998). Figure 3.3 illustrates the effects that negative spherical aberration has on a beam outside a resonator. Light rays further away from the optical axis undergo a different phase change than they would have undergone for a perfect lens. This causes them to be focused at different positions than those close to the axis. This shifting of the focus position along the optical axis is called longitudinal spherical aberration. The beam radius at the focus is also larger which is called transverse spherical aberration and the new focus size is known as the circle of least confusion.

3.5 Temperature profiles due to diode end-pumping

The pump beam profiles from fibre coupled diode lasers usually have a shape that is a mixture between flat-top and Gaussian. If a flat-top pump beam with a normalised intensity distribution of

$$I(r,z) = \frac{\alpha_{\text{abs}} e^{-\alpha_{\text{abs}} z}}{\pi w_{\text{p}}^2(z)(1 - e^{-\alpha_{\text{abs}} l_{\text{cr}}})} \qquad \text{for} \qquad r \leq w_{\text{p}}(z) \tag{3.22}$$

and 0 for $r > w_{\text{p}}(z)$ is used[1], the solution to Equation 3.3 is

$$T(r,z) = T(R_{\text{cr}}) + A_{\text{ft}}(z) \begin{cases} \ln\left(\frac{R_{\text{cr}}^2}{w_{\text{p}}^2(z)}\right) + 1 - \frac{r^2}{w_{\text{p}}^2(z)} & r \leq w_{\text{p}}(z) \\ \ln\left(\frac{R_{\text{cr}}^2}{r^2}\right) & r > w_{\text{p}}(z) \end{cases} \tag{3.23}$$

where R_{cr} and $w_{\text{p}}(z)$ are the crystal and pump radii respectively and $T(R_{\text{cr}})$ is the temperature of the cooling mount (Farrukh *et al.*, 1988; Cousins, 1992; Chen *et al.*, 1997; Chenais *et al.*, 2004). R_{cr} is the same as the temperature before heating due to teh chosen boundary conditions. The radially independent parameter is equal to

$$A_{\text{ft}}(z) = \frac{\eta_{\text{PH}} P_{\text{abs}}}{4\pi k_{\text{th}}} \frac{\alpha_{\text{abs}}}{(1 - e^{-\alpha_{\text{abs}} l_{\text{cr}}})} e^{-\alpha_{\text{abs}} z}, \tag{3.24}$$

[1]This is for an ideal pump beam. In reality a beam loses its flat-top shape after a certain propagation distance.

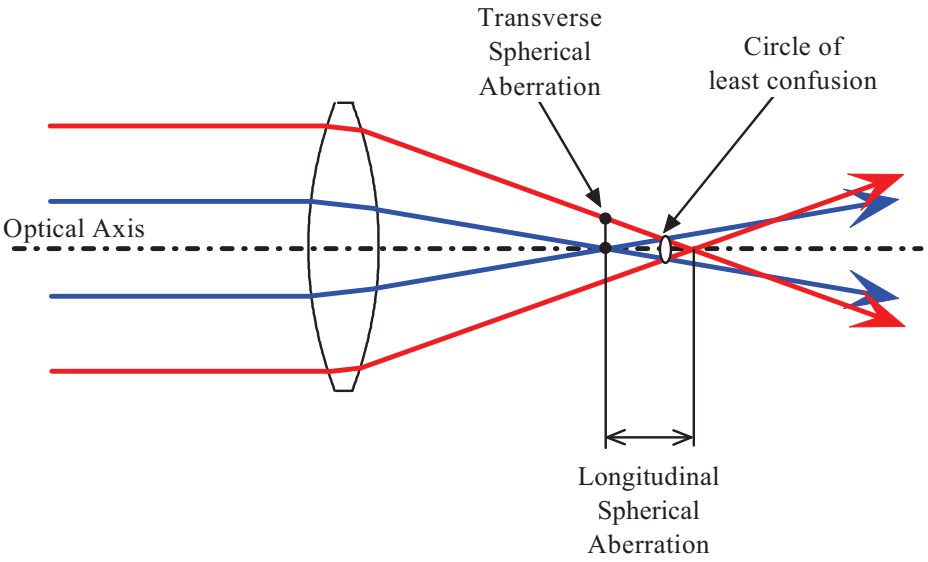

Figure 3.3: Negative spherical aberration in a lens. The displacement of the focus along the optical axis is called longitudinal spherical aberration while the increase in the beam radius is called transverse spherical aberration. The net effect is to shift the position and increase the size of the apparent focus which then becomes known as the circle of least confusion.

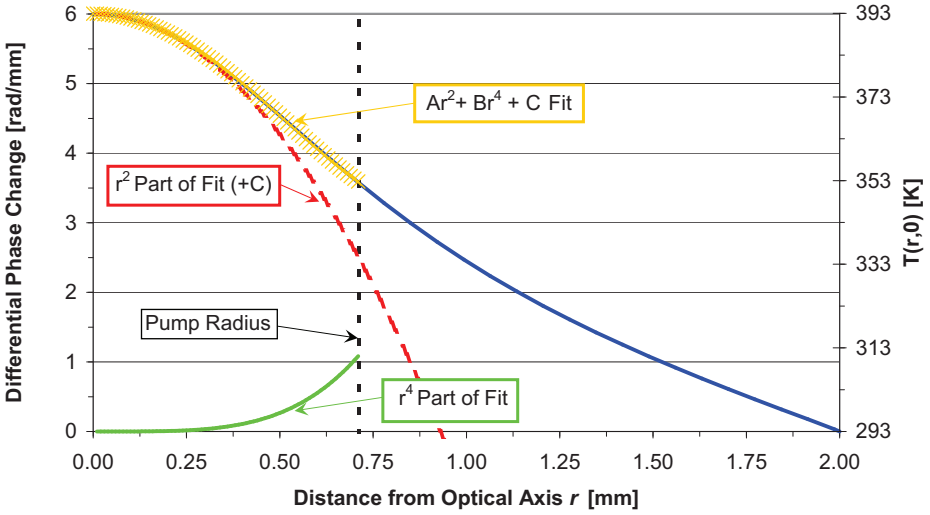

Figure 3.4: The temperature and refractive index differential phase change values on the pump face of a crystal pumped by a Gaussian pump beam can be found on the right and left axes respectively. A Seidel polynomial with both second and fourth order terms is also fitted to the data.

where η_{PH} is the percentage of pump power that is converted into heat and P_{abs} is the amount of absorbed pump power.

Closer examination of Equation 3.23 reveals that $T(r,z)$ inside the pump-region is purely quadratic. It is clear from Equation 3.19 that the differential phase profile inside the pump-region acts as a perfect lens. If the pump beam is collimated and absorbed over a relatively short distance the bulging inside the pump-region is also quadratic. This implies that the bulging will form a perfect positive thermal lens on the pump face(s) of the crystal.

If a similarly normalised Gaussian pump beam is used the temperature profile is given by

$$T(r,z) = T(R_{\mathrm{cr}}) + A_{\mathrm{ft}}(z)\left[\ln\left(\frac{R_{\mathrm{cr}}^2}{r^2}\right) + E_1\left(\frac{2R_{\mathrm{cr}}^2}{w_{\mathrm{p}}^2(z)}\right) - E_1\left(\frac{2r^2}{w_{\mathrm{p}}^2(z)}\right)\right] \tag{3.25}$$

where $E_1(u) = \int_0^\infty \frac{e^{-u}}{u}du$ is the exponential integral function (Innocenzi *et al.*, 1990).

The temperature and differential phase change profiles at $z = 0$ caused by such a Gaussian pump beam is plotted in Figure 3.4 using[2] $R_{\mathrm{cr}} = 2$, $w_{\mathrm{p}}(0) = 0.71$. Typical values of $A_{\mathrm{ft}}(0) = 30$, $\lambda = 1.064\,\mu$m and $dn/dT = 1 \times 10^{-5}\,\mathrm{K}^{-1}$ were used to calculate the differential phase change. An even Seidel polynomial fit to the differential phase profile inside the pump-region illustrates that in addition to quadratic lensing it also has a significant fourth order spherical aberration content. Substantial spherical aberrations can also be expected from the end-face bulging (Equation 3.10) due to the non-quadratic temperature profile.

[2]The reason why a pump radius of 0.71 was chosen was to later verify numerical calculations for the actual experimental setup.

Most fibre-coupled end-pump beams have a profile that is a mixture between flat-top and Gaussian. We can therefore expect a temperature profile inside the pumped region that is not purely quadratic. We will analyse the effects that this more complex temperature profile has on transiting laser beams in the next few sections.

Both the differential phase change profiles of the Gaussian and flat-top pump beams become roughly linear outside the pump-region. The effect that this has on beams inside resonators will be discussed in Sections 3.9.

An estimation of the relative amount of higher order aberrations can be made by expanding the differential phase profile caused by the Gaussian pump beam in Figure 3.4. The Zernike radius is chosen as the pump radius but other limits to the integration can also be defined depending on the phase area of interest. All the uneven Zernikes are found to be 0 due to the rotational symmetry of the thermal lens. The expansion does consist of a piston coefficient (Z_0^0) of 4.611, a defocus coefficient (Z_2^0) of -1.202, a spherical aberration coefficient (Z_4^0) of 0.177 and a 5^{th} order spherical aberration coefficient (Z_6^0) of -0.019. The defocus is not considered as an aberration because its phase change is quadratic which is the same as the phase of spherical and Gaussian beams. The 5^{th} order spherical aberration is an order of magnitude smaller than the spherical aberration and its influence is therefore insignificant. This implies that normal spherical aberration is the predominant higher order aberration within the pumped region of most end-pumped crystals. Thermal lenses inside the pump-region can consequently be approximated as spherically aberrated lenses. Astigmatism is also common, especially in uni-axial materials. However, in such cases the defocus and spherical aberration are traditionally separately evaluated in the horizontal and vertical directions.

3.6 Properties of vanadate thermal lenses

A few general observations can now be made about thermal lenses in a-cut vanadate crystals.

1. The π and σ-polarisations of any beam that propagates through a vanadate crystal will experience different thermal lens strengths due to the different dn/dT values in the two transverse crystallographic directions (Section 2.3.4).

2. The thermal lens for a specific polarisation in one of the crystallographic directions will be asymmetric because the thermal conductivity (Section 2.3.3) is different in the a and c-directions.

3. The thermal profile will have two components in the propagation direction because of the different absorption coefficients in the a and c-directions (Section 2.5.1). Pump light polarised along the c-direction (π) will be stronger absorbed and will have a concentrated heat load near the crystal pump-face. Light polarised along the a-direction (σ) will cause a heat load that is more spread out over the length of the crystal due to its weaker absorption.

4. The principle point of the thermal lens can change with pump power if the wavelength of the pump changes with input current (as is the case for high-power pump laser

modules). This is because the absorption changes with wavelength which also changes the volume within which the pump light is absorbed.

3.7 Influence of the thermal phase change on resonators

3.7.1 Resonator stability

Vittorio Magni published two papers in 1986 and 1987 in which he described the behaviour of resonators with a varying, pump-power dependent thermal lens (only the defocus) by using ABCD matrix formalism. His main contribution was the development of a theory that describes the alignment sensitivity of these resonators. In his first paper (Magni, 1986) he developed this theory for only a three element system, but later broadened it to multi-element systems with a single variable thermal lens (Magni, 1987). In this section we briefly illustrate how we utilised his analytic equations by using a specific three element resonator as an example.

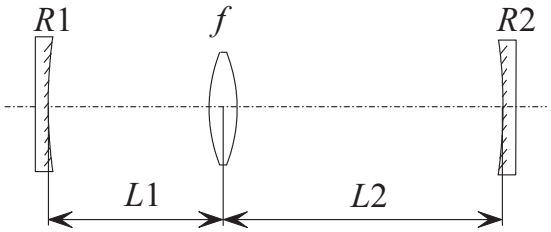

Figure 3.5: Simple three element resonator containing a variable internal lens.

Figure 3.5 illustrates the general three element resonator that Magni modelled. The thermal lens in the crystal is modelled as a thin lens of variable focal length f. Values of $R1 = 100\,\text{mm}$, $L1 = 150\,\text{mm}$, $L2 = 450\,\text{mm}$, $R2 = 300\,\text{mm}$ and a wavelength of $1.064\,\mu\text{m}$ is used in this example resonator. The beam radii on each of its three elements were calculated with Magni's equations as a function of the thermal lens focal length. Figure 3.6 illustrates the beam radii on $R1$, $R2$ and the crystal (thermal lens) as the dioptric power is increased by increasing the diode pump power into the crystal (Section 5.2.1).

It can be observed that there are two zones (ranges) of the dioptric power where the resonator is stable. These two zones have the same dioptric power width and also the same minimum beam radius in the crystal, $w_{\text{min-M}}$. At the stability limits of the resonator the beam radii on the optics either approach zero or infinity. Each stability limit is indicated with numbers in Figure 3.6 because they define each stability zone. At stability limit #1 the beam radii approach zero on both end-mirrors. At instability limits #2 and #3 the beam radii approach zero on one mirror and to infinity on the other. At stability limit #4 the beam radii approach infinity on both mirrors. Any stable resonator with an internal varying lens will have either or both of these stability zones. The zone where the radii on both of the mirrors approach zero at one of the stability limits is defined as Zone 1. The zone where the radii on both of the mirrors approach infinity at one of the stability limits is defined

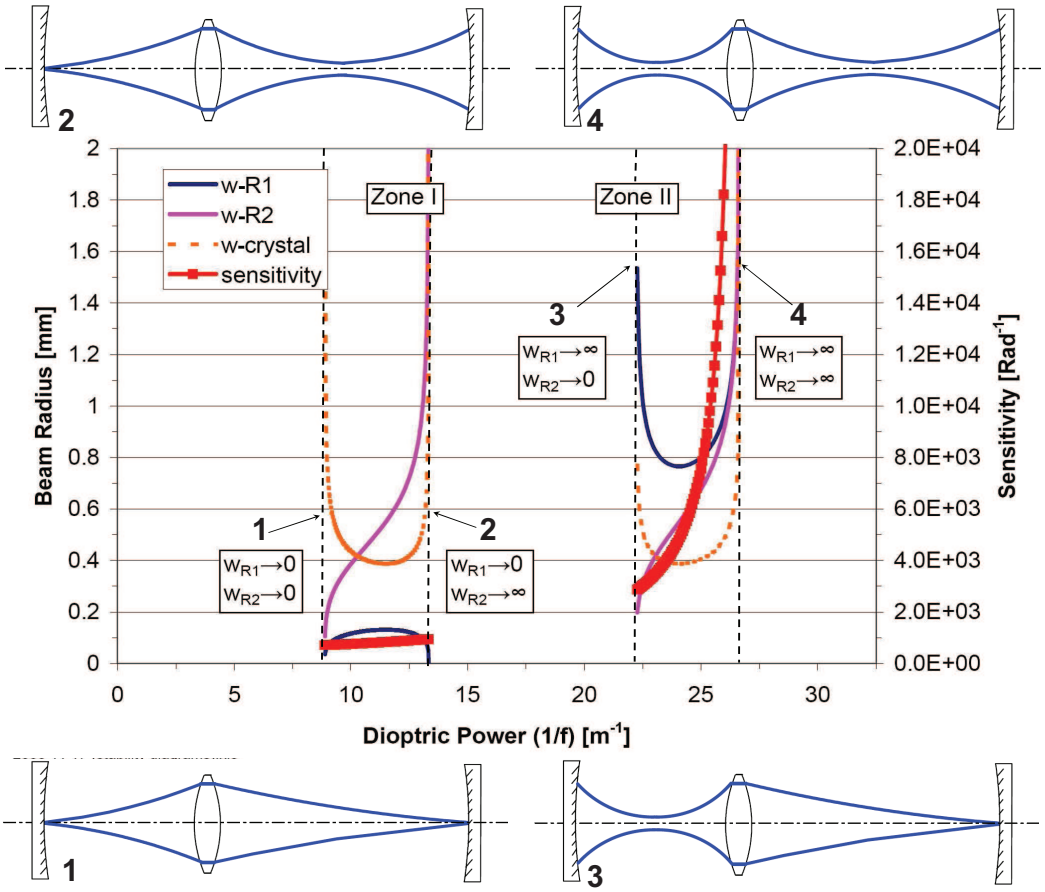

Figure 3.6: Beam radii and alignment sensitivities for a typical three element resonator with a variable internal lens calculated with equations provided by Magni (1986). Zone 1 is on the left and Zone 2 is on the right. Representations of the beam radii in the resonator at the stability limits are drawn above and beneath the graph.

as Zone 2. These two zones behave very differently with regard to the alignment sensitivity which for a specific end-mirror is defined as

$$s_{\text{al}} = \frac{d_{\text{al}}}{w_{\text{min-M}}}\theta_{\text{al}}, \tag{3.26}$$

where d_{al} is the displacement of the optical axis in the crystal for a small angular misalignment θ_{al} of the end mirror and $w_{\text{min-M}}$ is determined from the minimum of either of the two w_{cr} curves in Figure 3.6. The total alignment sensitivity (S_{al}) is the Euclidean norm of the two alignment sensitivities on each of the resonator end mirrors and is plotted in red in Figure 3.6.

In Figure 3.6 S_{al} (in red) can be observed to increase dramatically at the infinity-infinity stability limit of Zone 2 (stability limit #4). This is because the thermal lens images the mirror centres of curvatures on top of each other at this stability limit (see the top right resonator representation in Figure 3.6. The optical axis has to go through both the centres of curvatures of the mirrors and at least one image of the centres of curvatures to be contained within the resonator. There is therefore only a single direction in which the laser is stable, which makes the resonator extremely alignment sensitive.

Resonators with high alignment sensitivity tend to make extremely poor lasers because they tend to drift spatially to avoid small losses like air currents. High alignment sensitivity causes these slight movements to result in high intermittent losses. The resonator output power is therefore unstable and the output beam has poor pointing stability.

Unfortunately large beam radii on the optics are exactly what is required to avoid damage in high-power Q-switched lasers. For such lasers one **has** to build Zone 2 resonators because of the persistent small size of the beam radii on one of the mirrors in Zone 1 (Figure 3.6). The alignment sensitivities then have to be calculated for various resonator configurations until one is found in which S_{al} is below an acceptable limit.

3.7.2 Spherical aberrations and the matching ratio

The matching ratio is important for designing resonators because it determines the optimal TEM_{00} mode size in the crystal. In the previous section we demonstrated that for resonators that become stable at a certain thermal lens focal length, the beam size decreases to a certain minimum value. The TEM_{00} mode is the TEM mode with the smallest beam radius and will therefore first enter the pump-region as the dioptric power is changed. If the TEM_{00} mode oscillates with a significant overlap in the outer areas with spherical aberrations it will experience losses and have a decreased beam quality. These losses will decrease as the TEM_{00} mode size decreases with changing pump power. If the laser mode radius is decreased further, the losses for the first higher order mode (TEM_{01}) also decrease sufficiently so that it can compete with the TEM_{00} mode for gain. The ratio of the laser to pump mode size just before the TEM_{01} starts to oscillate is defined as the matching ratio and the resonator is said to be matched. There are therefore two regimes with respect to beam quality. In the first regime the spherical aberrations degrade the beam quality and in the second, higher order modes do so.

At the matching point the pure TEM_{00} mode has the lowest losses and therefore the highest output power and beam quality. However, the matched TEM_{00} output power will be lower than for an aberration free laser since the TEM_{00} mode does not overlap with the whole gain profile and also still overlaps with a significant amount of spherical aberrations.

The matching ratio (w_{00}/w_{p}) depends on both the losses from the spherical aberration and the gain of the TEM_{01} mode. It could therefore depend on the pump power, dn/dT value, the emission cross-section, the pump profile and, to a lesser degree, the expansion coefficient. We will experimentally investigate some of these dependencies in Sections 6.3.4 and 7.4.4.

3.8 Far field diffraction pattern of an aberrated thermal lens

The thermal phase change profile ($\Delta\phi_{\mathrm{tot}}(r)$ in Equation 3.12) also has an effect on external beams. The first obvious effect is to focus or defocus them due to its quadratic component (Section 3.4.5). The magnitude of this will vary for different wavelengths since both n and dn/dT are wavelength dependent (Equation 3.12 and Section 2.3.4).

The effect of spherical aberration in $\Delta\phi_{\mathrm{tot}}(r)$ also has a significant influence on the intensity profile of a Gaussian probe beam. The phase of a Gaussian spherical beam is quadratic and is given by

$$\phi_{\mathrm{Gauss}}(r) = -\frac{nk_\lambda r^2}{2R_{\mathrm{G}}} \tag{3.27}$$

where R_{G} is the Gaussian radius of curvature at a specific z position (Siegman, 1986 Chapter 16.3).

The wavelength of a probe beam must be chosen so that it is not absorbed or amplified by the laser crystal. The thermal lens should therefore not change the amplitude of the probe beam. This implies that the transfer function of the crystal $t_{\mathrm{cr}}(r)$ for probe beams consists of only a phase component which contains the total phase change profile from the varying refractive index and end-face bulging which is given by

$$t_{\mathrm{cr}}(r) = e^{i\Delta\phi_{\mathrm{tot}}(r)}. \tag{3.28}$$

To get an idea of what the influence of $t_{\mathrm{cr}}(r)$ will be inside the pump-region Equation 3.14 (the Seidel expansion) and Equation 3.27 can be combined to find the phase of the transmitted probe beam as

$$\phi_{\mathrm{pr}}(r) = -\frac{nk_\lambda r^2}{2R_{\mathrm{G}}} + A_{\mathrm{sl}}r^2 + B_{\mathrm{sl}}r^4 + C_{\mathrm{sl}} \tag{3.29}$$

$$= \left(A_{\mathrm{sl}} - \frac{nk_\lambda}{2R_{\mathrm{G}}}\right) r^2 + B_{\mathrm{sl}}r^4 + C_{\mathrm{sl}}. \tag{3.30}$$

C_{sl} is just a constant phase delay and A_{sl} only changes the radius of curvature of the probe beam. B_{sl} adds a non-quadratic component to the phase of the probe beam so that the probe beam can no longer be described by the Gaussian solutions. This will manifest itself

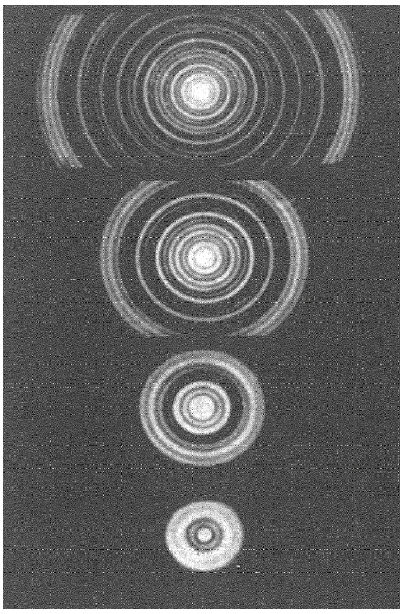

Figure 3.7: The diffraction patterns at various distances after an element with primary spherical aberration given in Born & Wolf (1986) who reproduced them from Nienhuis (1948).

in a slight increase in the M^2 of the beam as well as a modulation of its intensity profile. The analytical solution of the diffraction pattern of an element with only spherical aberration is given in Born & Wolf (1986) (pp. 476). The complete analytical solution consists of spherical Bessel functions and is rather elaborate. However, they do report that the diffraction pattern is shaped into multiple concentric rings. The centre has a high intensity peak and the outer ring is thicker than the rest and is subdivided into smaller rings. Figure 3.7 is a copy of experimental photos in Born & Wolf (1986) who reproduced them from Nienhuis (1948). We observed very similar ring structures in the intensity profile of a HeNe probe laser beam after it passed through a thermal lens. These ring profiles can be observed in Figure 6.12.

3.9 Thermal phase change outside the pump-region

In the previous sections only the phase change inside the pump-region was investigated. The phase change outside the pump-region is also significant but is often ignored because it does not overlap with the gain. From Figure 3.4 it can be observed that while the phase profile inside the pump-region is roughly quadratic, outside it approaches a linear curve that has a lower average slope than a linear fit to the phase inside the pump-region would have. The rate of phase change is therefore much lower outside the pump-region than inside. Light rays in this section would thus be focused much further away than light rays within the pump-region. To visualise this exaggerate Figure 3.3. Resonators that are only stable for large phase changes can therefore oscillate only within the pump-region and will be unstable outside it. The phase change outside the pump-region consequently acts a soft aperture. Such resonators are used for matching, and the higher order modes (with larger beam radii) either

have high losses or are completely unstable (Section 3.7.2). We can also find resonators that are only stable for lower phase changes and that become unstable at higher phase changes. Such resonators can be used for thermal lens measurement experiments as will be seen in Section 4.2.1.

3.10 Stresses due to the thermal expansion

The expansion that leads to the end-face bulging also causes stresses inside the crystal. The von Mises stress is of particular importance since materials start yielding when it reaches a critical value. The von Mises stress is defined as

$$\sigma_{\mathrm{vM}} = \sqrt{\frac{1}{2}\left[(\sigma_1 - \sigma_2)^2 + (\sigma_2 - \sigma_3)^2 + (\sigma_3 - \sigma_1)^2\right]}, \tag{3.31}$$

where $\sigma_{1,2 \text{ and } 3}$ are the stresses in the three principle axes of the crystal (Pilkey, 1997). These stresses can be calculated analytically or with numerical finite element analysis programs. The position and size of the maximum von Mises strains in these calculations then indicate at which pump power and at which position the crystal will yield.

3.11 Conclusion

This chapter examined the thermal phase change profiles in laser crystals and the effects they have on beams inside and outside resonators. The thermal phase change mainly focuses or defocuses beams inside or outside resonators. Spherical aberration inside the pump-region cause losses and an increase in M^2 for internal resonator beams. It can also add a non-quadratic component to the phase of an external probe beam so that it can no longer be described as Gaussian. In the next few chapters we will mainly describe methods for measuring the quadratic defocus.

Chapter 4

Thermal lens measurement techniques

4.1 Introduction

Measuring the focal lengths of thermal lenses has traditionally been viewed as challenging. This is because their focal length varies with input power, pump radius, higher order thermal processes and the area of the crystal that is examined (Bernhardi *et al.*, 2008, Section 2.5.3, Section 3.4.4 and Section 3.7.1). Thermal lens measurement techniques can be classified into three general categories, namely resonator, probe and interferometric methods. Resonator methods use the output beam properties of resonators with known dimensions and mirror curvatures to determine the thermal lens focal lengths at a specific pump power. Probe methods rely on how the thermal lens changes the size of an external probe beam after propagating through the crystal. Interferometric methods also utilise a probe beam but use different interference techniques to obtain the transfer function of the laser crystal and can easily determine higher order aberrations. This chapter will review some of the methods in these categories to measure strong positive thermal lenses.

4.2 The resonator methods

The resonator methods can be divided into several different subcategories which utilise different properties of resonators. These are methods that

1. use the resonator stability limits (quenching methods),
2. back-calculate the thermal lens from the output beam,
3. use the beating between transverse modes in a multimode beam and
4. use the degeneracy points of a resonator.

Some of these methods will be discussed in the next few sections.

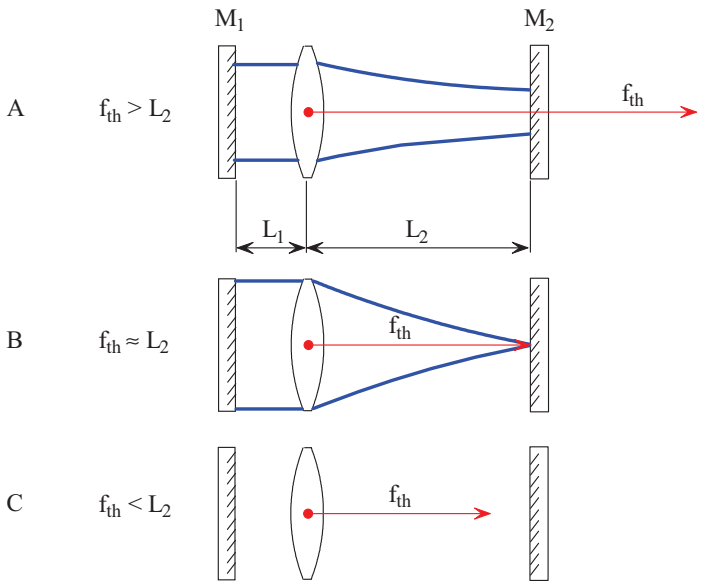

Figure 4.1: Quenching of a flat-flat resonator as the focal length decreases due to increasing pump power. For case A, $f_{\mathrm{th}} \geq \mathrm{L}_2$ and the laser is stable. For case B, $f_{\mathrm{th}} \sim \mathrm{L}_2$ and the laser is at its stability point and starts to quench. Finally, for case C, $f_{\mathrm{th}} \leq \mathrm{L}_2$ and the resonator is unstable.

4.2.1 Determining the thermal lens by means of resonator quenching

Quenching refers to the pump-region where resonators become unstable. It can be identified by a decreasing laser output for increasing input pump powers. The quenching methods are some of the quickest, easiest and cheapest methods to measure thermal lenses. Variations of these methods were used by Lancaster & Dawes (1998), Sennaroglu (1999) and Song *et al.* (2002). The simplest quenching method uses a resonator consisting of both a flat output-coupler and a flat back-reflector as is illustrated in Figure 4.1. One of the mirrors is located close to the crystal and forms the short arm L_1 of the resonator. The thermal lens is approximated by a thin lens close to the pumped side of the crystal. The distance to the other mirror M_2 (L_2), is varied but must always be longer than L_1, bearing in mind that the optical crystal length l_{cr}/n has to be added to the arm length that does not contain the pumped side.

These resonators are distinctive in that they are only stable when the focal length of the thermal lens f_{th} is larger than L_2. This is illustrated in Figure 4.1 A. For crystals with positive dn/dT values the dioptric power ($D = 1/f_{\mathrm{th}}$) increases with pump power. The focal length therefore decreases as the pump power is increased, until it is the same magnitude as L_2 ($f_{\mathrm{th}} = \mathrm{L}_2$) at which point the laser becomes unstable and the output power decreases. This is illustrated in Figures 4.1 B and C. The quenching pump power is therefore an input power where the thermal focal length is known ($f_{\mathrm{th}} \sim \mathrm{L}_2$). The length of L_2 can therefore be

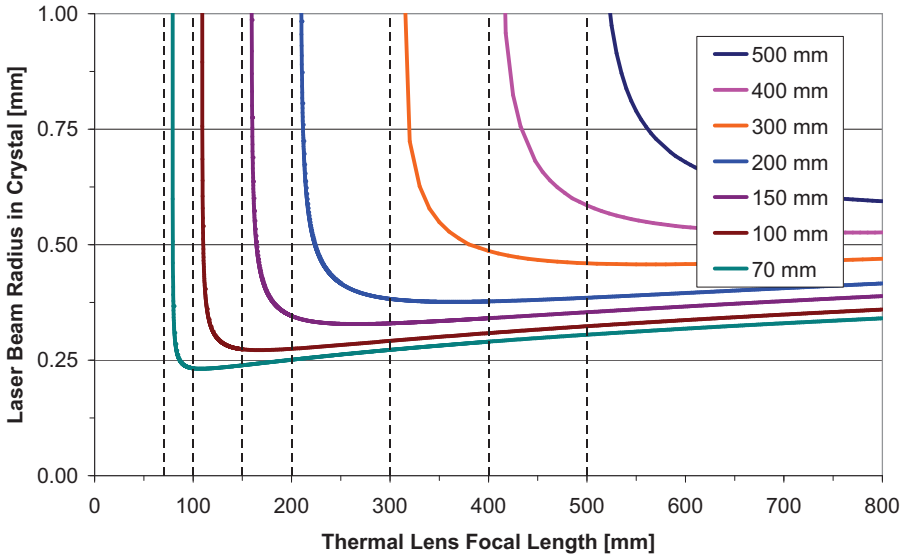

Figure 4.2: The TEM_{00} laser radius in a crystal as a function of thermal lens focal length of several flat-flat resonators with varying arm lengths L_2.

varied to obtain f_{th} over a range of pump powers.

As an example, Figure 4.2 plots the laser TEM_{00} beam radius in the crystal (w_{cr}) versus f_{th} for several lengths of L_2 (with L_1 kept constant at 61 mm). In all of the cases w_{cr} increases dramatically towards an asymptote at $f_{th} = L_2$. This increase also becomes sharper and the minimum beam radius in the crystal decreases as L_2 is made shorter. A large pump radius is usually chosen for high-power lasers in order to decrease stresses and thermal lensing (Bernhardi, 2008). This implies that for measurement of strong thermal lenses (short L_2's) the TEM_{00} mode size is much smaller than the pump size so that multiple higher order modes oscillate in the resonator. Matching (Section 3.7.2) will therefore be rarely observed in high-power flat-flat lasers because the matching power is very sensitive to small changes in thermal lensing near the asymptote.

Flat-flat resonators also extract all the gain from laser crystals before they quench because the higher order modes are stable for lower values of f_{th} and overlap with the outer aberrated parts of the gain medium (Section 3.9). This implies that the aberrated part is also measured by the quenching method. The effect of this is that the quenching is not a sharp well defined point, but rather a region where the laser output power rolls over due to the lower rate of phase change in the outer aberrated parts thereby reducing the accuracy of this method. We attempt to increase the accuracy and separate the different parts of the thermal lens by identifying finer structures in the laser output power curve in Section 6.2.

4.2.2 Back calculating the thermal lens from an output beam

The thermal lens focal length can also be obtained by characterising the output beam from a resonator and back-calculating what thermal lens focal length is inside it. Figure 4.3 shows

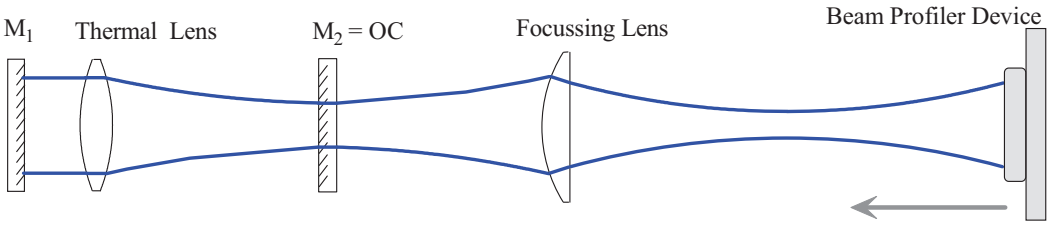

Figure 4.3: Characterisation of the output beam of a resonator with a thermal lens.

the output of a resonator with an internal thermal lens being characterised by a beam profiler device. The profiler can be a camera, slit, knife-edge or any other device that can determine the size of the output beam. A focusing lens is needed to create an artificial waist, since the waist of the output beam is usually located close to, or inside the resonator (in most cases on a flat output coupler). The beam size is measured at several positions to characterise the beam spatially. Gaussian propagation equations are then used to back-calculate the beam size somewhere inside the resonator which is employed to determine the focal length of the thermal lens with an ABCD matrix model of the resonator.

Several variations of this technique have been used in the past. Neuenschwander *et al.* (1995) measured the beam radius in the near and far field with a lens placed at the distance of its focal length behind the output coupler. Both Agnesi & Uggetti (2002) and Mukhopadhyay *et al.* (2003) used a knife edge to measure the beam and then back-calculated to determine the size of the beam radius on the output-coupler.

A big advantage of this method is that the focal length is determined from a beam quality (M^2) measurement that is already necessary in laser development. The method can therefore be relatively cheap and easy by using existing or self built equipment.

The traditional way that the method is applied is not very accurate. The error on the magnitude of the thermal lens can be up to 30% (Chenais *et al.*, 2006). These can be attributed to two factors which we tried to eliminate. The first is mainly due to the uncertainty on the distance from the artificial waist position to the principle point of the lens. This error can be eliminated by performing a single measurement of the beam radius before the focusing lens. The magnitude of the thermal lens can then be obtained by back-calculating from the accurate measurement position by using the M^2 value that was measured after the lens. The calculation produces two solutions. The correct one can be identified by comparing the approximate beam size on the focus lens with the numerical propagation of both solutions.

The second source of errors is that different size beams overlap with different amounts of spherical aberration. The net effect is that the Zernike radius is different for different measurements which affects the magnitude of the defocus in aberrated systems. To reduce this error we propose to use only matched TEM_{00} beams which overlap with a minimum of spherical aberration. The resulting thermal lens focal lengths are also of greater practical value since they are obtained for matched resonators which deliver good quality beams. We termed this version of the back calculation method, the mode-matched method, and present it in the following section.

4.2.3 The new mode-matching method

Many resonators can be used to achieve matching. We chose to use a relatively simple concave (CV) flat resonator as is illustrated in Figure 4.4. The distance between the curved mirror M_2 and the crystal forms the long arm of the resonator L_2. The curved mirror M_2 is a highly reflective back-reflector and the flat mirror M_1 is a partially transmitting output coupler which ensures that the beam that leaves the resonator is reasonably collimated.

The resonator is unstable for weak thermal lenses and only becomes stable for stronger thermal lenses with focal lengths $f_{th} \leq L_2$. This is illustrated in Figure 4.4 A and B. This resonator is therefore the inverse of the quenching flat-flat resonator that is stable for weak thermal lenses and becomes unstable for strong thermal lenses. As the pump power is increased the strength of the thermal lens increases and the mode size in the resonator decreases. The resonator is matched when the TEM_{00} laser mode equals the matching ratio times the pump radius for a specific crystal and pump profile (Section 3.7.2). A maximum of four such matching points can be found in resonators (Figure 3.6). Any one of them can be used, but it is recommended to keep to the one described here since it is alignment insensitive and the other matching points can easily be confused with each other in some set-ups.

The pump power at which matching occurs can be determined from the intensity profile on a CCD camera. The TEM_{00} mode intensity increases as the power is increased from threshold. This is because its losses decrease due to decreasing overlap with the spherical aberration as well as an increase in the amount of active ions that are pumped into the upper laser level. At pump powers higher than the matching pump power the first higher order mode (for example TEM_{10}) oscillates and competes with the TEM_{00} mode for gain. The TEM_{01} mode has a node on the propagation axis where the TEM_{00} mode has a maximum intensity. The combined intensity profile of the two modes therefore shifts from the centre to the sides of the beam. This is first visible as a decrease in the central intensity of the beam and is illustrated by the peaking of the maximum intensity in Figure 4.5. If a laser is operated at a pump power level just before this happens it is said to be matched. This method of detecting the matching point is very accurate so that the matching power can easily be determined with an accuracy of ± 0.2 W.

The focal length of the thermal lens is then obtained by approximating the thermal lens as a perfect thin lens and then applying the back-calculation technique of the previous section using a beam from a matched resonator. The thin lens approximation is valid because the TEM_{00} mode only overlaps with the central relatively unaberrated part of the thermal lens (Siegman, 1986 pp. 593 - 597).

As an example, Figure 4.6 shows these calculated TEM_{00} beam radii in a laser crystal as function of thermal lens dioptric power. The calculations were done for resonators with different arm lengths L_2 to a 50 mm concave back-reflector M_2 (L_1 was 58 mm). Plot A never matches so that it can not be used to determine the thermal lens focal length. In plot B matching occurs, but it is not possible to experimentally determine whether the resonator is matched because the first higher order mode never oscillates. In plots C to F matching occurs at different thermal lens dioptric powers. The thermal lens behaviour can therefore be determined over a range of pump powers by adjusting the length of L_2 as well as the curvature of M_2.

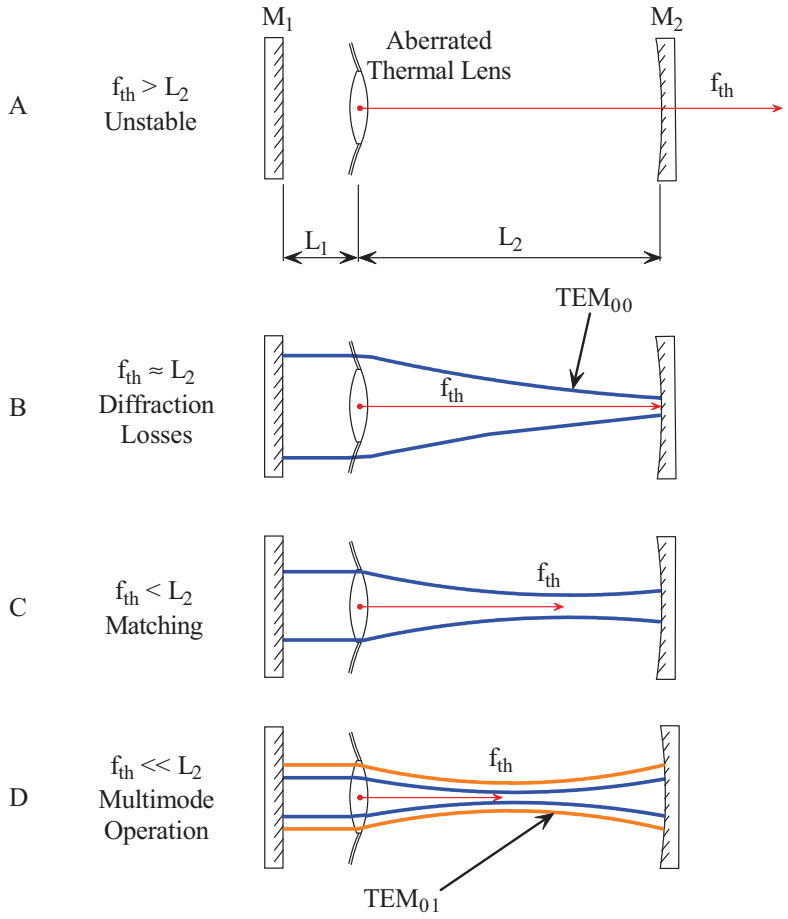

Figure 4.4: Mode matching in a concave-flat resonator. In A, $f_{\mathrm{th}} > \mathrm{L}_2$ and the laser is unstable. In B, $f_{\mathrm{th}} \sim \mathrm{L}_2$ and the TEM_{00} overlaps with the outer spherically aberrated part of the thermal lens which decreases its beam quality. In C, $f_{\mathrm{th}} < \mathrm{L}_2$ and the resonator is matched. In D, $f_{\mathrm{th}} << L_2$ and higher order modes start to oscillate which again decreases the beam quality.

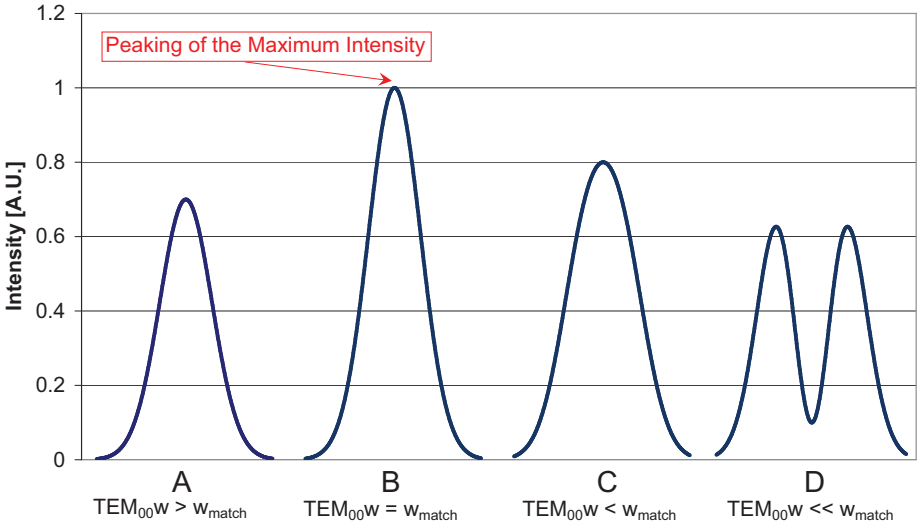

Figure 4.5: A schematic of the transverse x or y profiles of a concave-flat resonator just before and after matching. In A, the TEM_{00} mode undergoes diffraction losses. In B, matching occurs and the centre of the intensity profile peaks. In C and D, the first higher order mode starts to compete for gain and shifts the intensity to the sides of the beam.

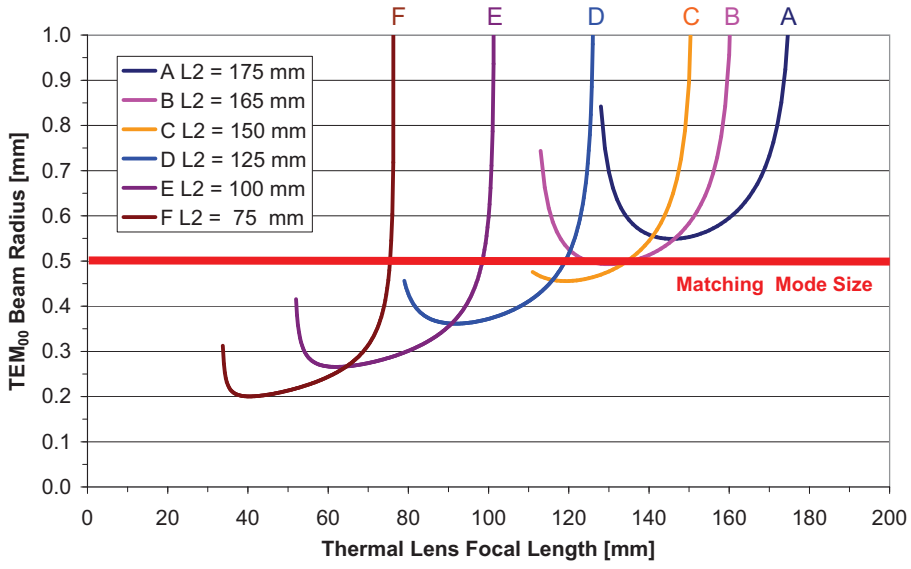

Figure 4.6: Beam radii in the laser crystal (or on the lens in Magni (1987)'s model) as a function of focal length for a typical concave-flat resonator consisting of a 50 mm concave back-reflector at several distances L_2 from the crystal ($L_1 = 58$ mm).

Advantages and disadvantages of the new mode-matched method

The method has several advantages:

1. The method is much more reproducible than other resonator methods because it measures only the central relatively unaberrated part of thermal lens by default.
2. The resonators that are used to determine the thermal lens focal length deliver good quality beams that can be used for other applications.
3. It measures the M^2 factor for the TEM_{00} beams as a function of diode pump power. The M^2 factor changes with increasing spherical aberrations inside the laser crystal.
4. It also measures the laser power versus diode pump power for TEM_{00} beams. An effective slope efficiency for only the TEM_{00} beams can therefore be obtained by combining a range of measured output powers.

The method also has several disadvantages:

1. The measurements can take very long and become quite cumbersome.
2. It is still not as accurate as some of the interferometric techniques.
3. Thermal lens measurements can only be performed under lasing conditions.
4. While this method was designed to measure the unaberrated part of the thermal lens, knowledge about the aberrated part is also of great use. This method does not allow measurements of both in a single measurement.

4.2.4 The transverse-mode beat-frequency method

The transverse-mode beat-frequency method was first proposed by Ozygus & Erhard (1995). It uses the property that the transverse Gaussian modes have slightly different frequencies due to the Guoy phase shift in a resonator (Siegman, 1986 pp. 645-646). These frequency values are a function of the resonator dimensions and the thermal lens focal length.

The differences between these frequencies can be detected by means of a high frequency modulation on top of the normal laser output intensity which is called frequency beating (Siegman, 1986 pp. 575). The higher order modes are usually approximated as orthogonal which means that they should not beat with each other (Siegman, 1986 pp. 568). However, they are visible if only a small part of the transverse profile of a multimode beam is detected with a fast pin diode. This is because the pin diode does not integrate over the modes but detects only a small part in which the modes are not orthogonal with respect to each other. The frequencies can then be obtained by means of a Fourier analysis of the modulated intensity trace. Highly multimode beams like those that emanate from short flat-flat resonators are therefore used in this method.

Ozygus & Erhard (1995) also give solutions for the thermal lens values for a curved-flat resonator that is in multimode operation. They show that their measured thermal focal length

values decrease with the higher order mode number. This is because the radii of the higher order modes increase with mode number (Hodgson, 2005 pp. 225). The higher the order of the mode is, the more it overlaps with the aberrated part of the thermal lens. The net effect is a measurement of a weaker thermal lens due to the negative spherical aberration. Both the central and aberrated parts of the thermal lens can therefore be measured simultaneously by using a highly multimode beam and recording the different beat frequencies.

4.2.5 The resonator degeneracy method

This method is very similar to the one in the previous section but use special resonator configurations. The resonance frequencies of both the longitudinal and transverse modes in a resonator are given by $\nu_{r,s,q} = q\nu_l + (r+s+1)\nu_t$ where q is the longitudinal mode number, $\nu_l = c/2L$ is the longitudinal mode spacing and r & s are the rectangular higher order mode numbers (Hodgson, 2005 pp. 233). The longitudinal and transverse resonance frequencies also have the following relationship:

$$\nu_t = (\nu_l/\pi)\arccos(\sqrt{g_1 g_2}) \tag{4.1}$$

where g_1 and g_2 are the cavity stability parameters which are defined as (Magni, 1986):

$$g_{1,2} = 1 - \mathrm{L}_{2,1}/f_{\mathrm{th}} - (\mathrm{L}_1 + \mathrm{L}_2 - \mathrm{L}_1\mathrm{L}_2/f)/\mathrm{R}_{1,2} \tag{4.2}$$

where $\mathrm{L}_{1,2}$ are the resonator arm lengths and $\mathrm{R}_{1,2}$ the radii of curvature of the left and right resonator mirrors (as depicted in Figures 4.1 and 4.4). Resonators with $g_1 g_2 = 0$, 1/4, 1/2 and 3/4 correspond to $\nu_l/\nu_t = 2, 3, 4$ and 6. This implies that the higher order transverse modes have resonance frequencies that are integer numbers of each other and of the longitudinal modes. They are therefore degenerate modes and the degeneracy points are thus denoted as second, third, fourth and sixth order degeneration. At these resonator configurations there will be spatial hole burning by the higher modes since they overlap longitudinally. Wu *et al.* (1999) showed that at the degeneracy points the TEM_{00} power decreases sharply and that the spatial profile of the laser obtains a large multimode content. This is in order to extract the gain optimally, which is now different from normal non-degenerate resonators because of the spatial hole burning. Resonator configurations can be found where one of the arm lengths is kept constant so that by changing the other arm length the resonator can have either 2^{nd}, 3^{rd} or 4^{th} order degeneracy, which is verified by means of the TEM_{00} power output, the 2D beam profiles or the transverse mode beat frequencies. The thermal lens focal length can then be determined from Equation 4.2.

4.3 Probe beam techniques

Probe beam techniques can be divided into two categories. The first employs beam propagation methods that:

1. measure the focus position of an external probe beam or,

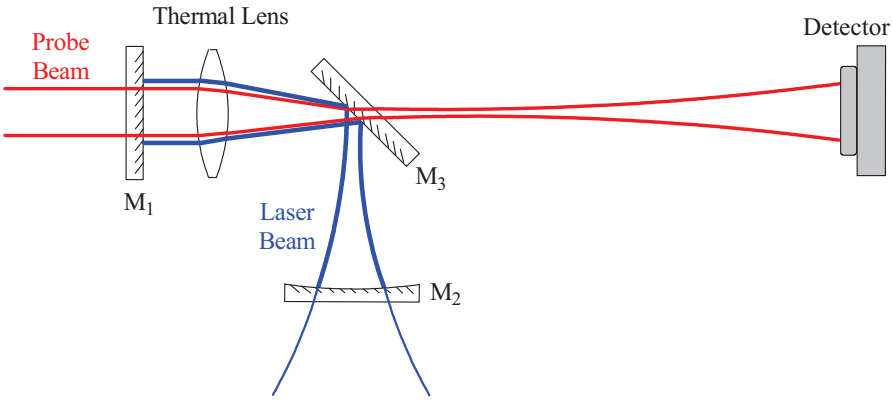

Figure 4.7: A probe beam is focussed by a thermal lens inside a resonator. It is transmitted by resonator mirror M_3 and its radius is measured by a detector.

2. back-calculate the focal length from the beam radius change of an external probe beam or,

3. measure the deflection of a very small probe beam (compared to the pump mode size).

The second uses various interferometric techniques like

1. shear interferometry and

2. Shack-Hartman wave-front analysis.

Measuring the focus position of an external probe beam is the quickest and the easiest method, but it can yield incorrect results if the collimation of the probe beam is not well known. Back calculating the thermal lens is more accurate and can be used with slightly diverging beams. Both techniques are covered in the following section. The deflection technique is useful since it provides a space resolved measurement of the thermal lens. Clarkson (2001) used it extensively to determine the phase change profile in a Nd:YAG rod. The interferometric techniques were not employed in this study and are therefore only briefly discussed.

4.3.1 Probe beam propagation methods

This method was first proposed by Hu & Whinnery (1973). Changes in the beam radius of a probe beam are used to determine the focal length of the thermal lens through which it was propagated. Figure 4.7 illustrates a simple probe beam set-up to measure thermal lens strength inside a resonator. The probe beam is aligned collinear with the laser and pump beams inside the crystal. The wavelength of the probe beam must therefore be in a range so that it is not absorbed or amplified by the crystal and is also not strongly reflected by the laser mirrors.

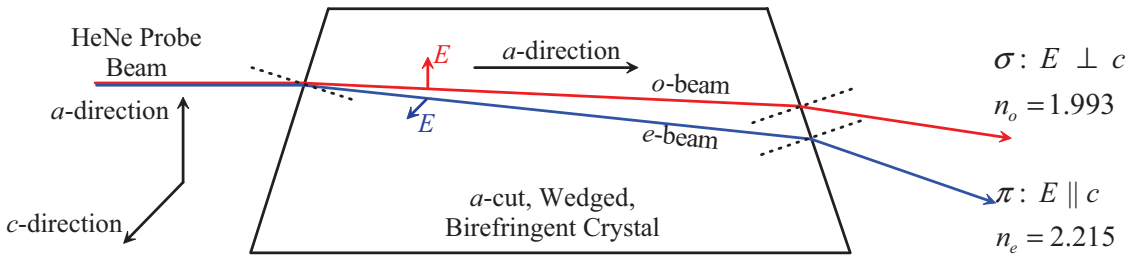

Figure 4.8: A wedged birefringent crystal splits a probe beam into ordinary and extraordinary beams. Each beam scan be used to determine the thermal lens behaviour for a particular polarisation.

In its simplest form a detector is used to determine the waist position at various pump powers. It is important that the probe beam is well collimated otherwise the waist position will not correspond to the focal length of the thermal lens. Usually the detector position is kept constant and the pump power is increased until the minimum beam radius is observed. One of the main problems with this method is that in many set-ups it is not possible to get a well enough collimated beam into the crystal due to the presence of pump lenses and curved laser mirrors.

The focal length can also be determined by back calculating from the change in the beam radius of a characterised probe beam. ABCD matrices are used in the calculations wherein the thermal lens is approximated as a thin lens at the pump-face of the crystal. The focal length is then determined for a range of pump powers at a single detector position. It is preferable that the probe beam is roughly collimated. If this is not possible in the required set-up, the divergence must be kept to a minimum so that the probe beam radius does not change significantly inside the crystal.

For *a*-cut birefringent crystals the probe beam must also be linearly polarised in one of the two crystal directions. This is because each polarisation experiences a different thermal lens due to the different dn/dT values in the two crystallographic directions (Section 2.3.4). If the beam is not polarised the *o* and the *e*-beams after the crystal must be seperated from each other with a polariser. An alternative is to use wedged birefringent crystals. Because the two crystallographic directions have different indices of refraction, the *o* and the *e*-parts of the probe beam are spatially separated, which then diverge from each other after the crystal. This is illustrated in Figure 4.8. The focal length of the thermal lens of each polarisation can therefore be simultaneously obtained if a large area CCD is used. However, one should only measure the two beams individually under lasing conditions. The test laser is then set up to oscillate only on the polarisation of interest since higher order thermal effects might be different for each polarisation.

Advantages and disadvantages of the probe beam propagation methods

Probe beam methods are especially useful for performing comparative measurements. They can be used to determine the thermal lens focal length under both lasing and non-lasing conditions. They can also be used to compare the focal lengths of the different polarisations and different crystals. Such measurements of the relative difference in the dioptric power can be very accurate since the measurements are not sensitive to the crystal position.

A major drawback of these, and all other probe beam methods, is that the probe beam wavelength is often much shorter than the laser wavelength. Usually the spectrum of the probe is in the visible because it also doubles as an alignment laser, thus decreasing the complexity and cost of the set-up. This causes complications since the dn/dT value (which is usually the main contributor to the thermal lens) is also wavelength dependent. This means that the probe beam will experience a different thermal lens strength than the laser beam in the resonator. One therefore has to know the dn/dT values at both the probe and laser wavelength beforehand, in order to get the correct scale factor with which to multiply the measured focal lengths. This means that the measurements are not independent of other measurements, which could be problematic for new laser materials. This can be addressed by using a laser which has a different gain material but which oscillates close to the wavelength of the probed laser crystal. For instance, a Nd:YVO_4 laser can be probed with a Nd:YLF laser which has slightly wavelength shifted emission lines at 1 and 1.3 μm.

4.3.2 Interferometric methods

Interferometric techniques also utilise probe beams. Shear interferometry involves splitting the probe beam so that one beam probes the crystal and the other bypasses it. By letting them interfere an interferogram is obtained which provides information about the derivative of the wave-front. Any distortion in the wave-front will then show up in the interferogram. The thermal lens focal length and aberrations is then calculated from these distortions (Blows *et al.*, 1998).

The Shack-Hartmann wave-front sensor measures the wave-front by using an array of small lenslets. A wave-front of a probe beam that was propagated through a thermally aberrated crystal enters the sensor and falls onto a lenslet array. Each lenslet focuses the part of the wave-front that falls on it, onto a CCD array where the focus is laterally displaced depending on the local slope of the wave-front on the lenslet. These slopes are then calculated by software which uses the position of the displaced focuses. The wave-front can consequently be reconstructed by merging all the individual wave-front slopes (Chenais *et al.*, 2004; Neal & Mansell, 2008). The static reference aberrations is obtained by first measuring the wave-front of the probe beam without any pump power into the crystal. The crystal is then pumped and the wave-front is measured again. Subtracting the two wave-fronts provides only the distortions due to the temperature profile. The phase aberrations are then found by expanding the measured aberrations by a set of orthogonal Zernike polynomials (Section 3.4.4). From this expansion the A_2^0 and A_4^0 Zernike coefficients are found from which the thermal focal length and spherical aberration can be determined (Section 3.4.5).

4.4 Conclusion

This chapter gave an overview of some of the methods that can be employed to measure the focal lengths of thermal lenses. The most important resonator, probe beam and interferometric methods were discussed. The next few chapters illustrate how some of these techniques are implemented to measure the thermal lens focal lengths in Nd^{3+} vanadate crystals.

Chapter 5

Experimental set-up

This chapter focuses on experimental techniques that were developed by us to build end-pumped solid-state lasers and to measure the strength of thermal lenses. The pump set-up is especially important since it has a large influence on both the gain and thermal properties of the laser. We therefore devote a substantial portion of this chapter to it. We also show how some of the thermal lens measurement techniques that were discussed in the previous chapter were implemented into one comprehensive set-up. This chapter is structured chronologically and the first section starts with the description and mounting of the vanadate crystals.

5.1 Low doped vanadate crystals

5.1.1 Crystal properties

The thermal lensing behaviour of a Nd:YVO_4 crystal was compared to that of a Nd:$GdVO_4$ crystal. Two other Nd:YVO_4 and three other Nd:$GdVO_4$ crystals were used to determine the variance of the measurements with respect to different crystals and boules. One Nd:YVO_4 crystal that was accidentally damaged on one side in the mounting process was used for destructive testing under non-lasing conditions. The crystals had a low doping concentration of $\sim$0.15% and were grown by Castech (Castech, 2008). Figure 5.1 illustrates the crystal dimensions, wedges and orientation of the crystallographic directions. The crystals were square-cut with transverse dimensions of 4×4 mm. One crystal of each material was 18 mm and the rest were 20 mm long. Two different boules were used for the 18 mm and 20 mm long crystals. This made the thermal lens results more representative and less prone to doping concentration errors.

The pump-faces of the crystals were cut with a 2° wedge at opposite angles. This was originally done to avoid back reflections in mode-locking experiments that did not form part of this study. The wedge was orientated so that the beam deviation was sideways when the stronger π-polarisation was vertical. This was because the 45° HR 1.06 μm HT 808 nm mirrors (45° HR laser mirrors) that were used in the resonator better reflected vertically polarised light. The wedges also had the advantage that the crystal spatially separated the two polarisations due to its large birefringence as was illustrated in Figure 4.8. The lasers could therefore be forced to operate on only one polarisation simply by aligning them, so

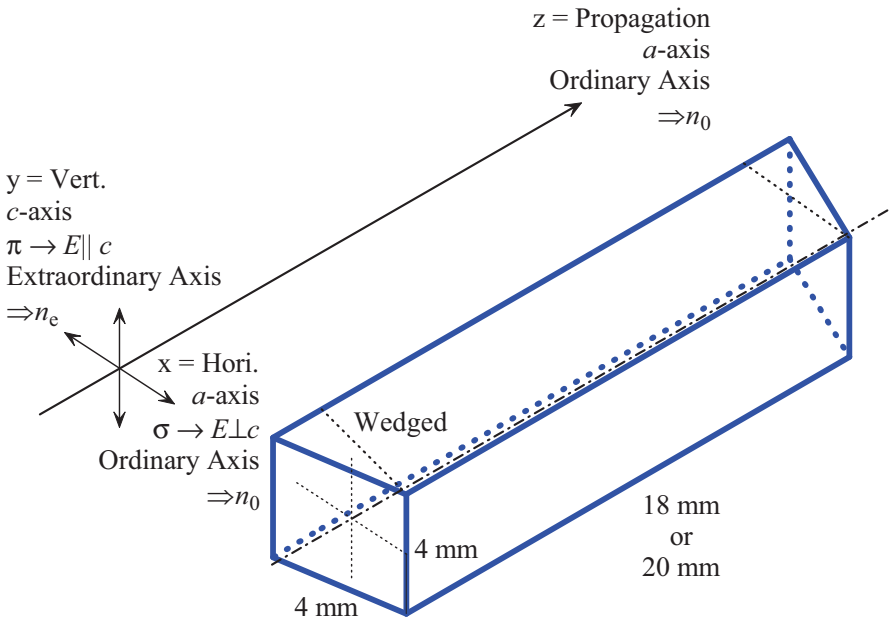

Figure 5.1: General dimensions of the square-cut vanadate crystals that were used in this study.

that the different resonator methods could be used to determine the thermal lens properties of each polarisation separately. This also caused the polarisation to be stable for the entire range of pump powers that were available to us. This is different from unwedged crystal lasers that can change polarisation due to the different strengths of the thermal lensing of the two polarisations (Lin *et al.*, 2009).

All the crystals were anti-reflection coated for both 1.064 and 1.34 μm. The output wavelength of the laser could therefore be forced onto the much weaker 1.3 μm line by exchanging the 1.06 μm coated optics with 1.34 μm coated ones. Mirrors were therefore used to select the wavelength and alignment was used to select the polarisation.

5.1.2 Mounting square vanadate crystals

The laser crystals were mounted in heat-sinks to remove excess heat generated within them by various transition processes (Section 2.5.3). The more efficiently the heat is removed by the heat-sink, the lower the temperature and therefore the negative thermal effects will be in the crystal. The heat-sinks were made from copper because of its high thermal conductivity of 380 W/m K. Copper is also relatively inexpensive compared to other high thermal conductivity materials like gold (318 W/mK), silver (429 W/m K) and diamond (900 to 2320 W/m K or even higher). The heat-sinks were water-cooled since as much as 40 W of thermal power could be generated inside the crystals due to the quantum defect alone (when double end-pumping them).

The laser crystals were premounted with four copper blocks, effectively encasing the crystal. This is illustrated in Figure 5.2 by the central orange coloured blocks. Premounting

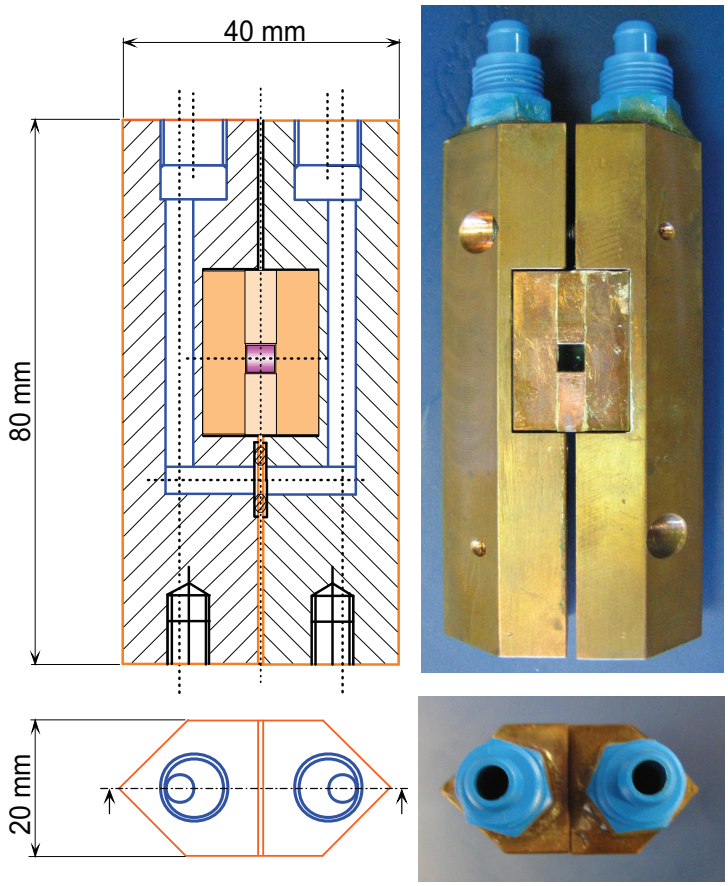

Figure 5.2: A pre-mounted square crystal clamped between two water-cooled copper heat-sinks. On the left is a sectioned front and a top view machine drawing of the assembled mount. The four orange coloured blocks formed the premount of the crystal. The water cooling channels can be observed in blue on the sectioned drawing. On the right are photos of the complete assembled mount.

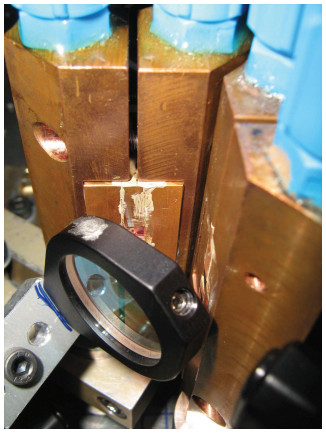

Figure 5.3: Two crystal mounts and a 45° HR laser mirror spaced close together in a quadruple pump set-up. This set-up was made possible by the 45° edges of the water-cooled heat-sinks.

made handling the crystals easier and reduced the risk of damaging them. A new experimental mounting technique was used to do this. Traditionally Indium foil is used as an interface layer between the heat-sink and the crystal since it is extremely malleable. It therefore easily fills voids between the crystal and copper surfaces which increases the heat transfer efficiency between them. We chose to use a silver epoxy (H20S from Epotek (2008)) to bond the square vanadate crystals to the premount copper blocks. The silver epoxy had a relatively high thermal conductivity of $\sim$30 W/m K for bonding layers of less than 50 μm. This requirement was fulfilled since the copper blocks were pressed directly to the crystal during curing. All the excess epoxy was therefore squeezed out, which left only a very thin layer between the crystal and the copper blocks. The heat flow between them was therefore high due to this thin interface layer and relatively high thermal conductivity. For comparison, Indium has a thermal conductivity of $\sim$80 W/m K but is usually relatively thick compared to the epoxy. This can be corrected by melting the Indium and we are currently investigating such techniques. The crystals were also recessed by more than half a millimetre on each side in the z-direction to ensure that they were cooled right up to their pump-faces where the thermal load was the highest. This was a mistake in hindsight because it made cleaning the optical surfaces of the crystals very difficult.

The pre-mounted crystal was then wedged between two water-cooled copper heat-sinks. This can be observed on the left and right of the pre-mounted crystal in Figure 5.2. Indium could be used between the premount and the water-cooled heat-sinks because of the large contact area between them and to be able to exchange premounted crystals. The water channel formed a single loop through the two mounts and was sealed at the connection point with a thick O-ring. From the top view of Figure 5.2 it can be observed that the water channels were off-centre with respect to the Festo pipe connectors that were used (CK-1/8-PK-6-KU in Festo (2009)). This was to accommodate the pre-mounted crystal and to make the water flow turbulent, which increased the heat flow between the copper and the water. The whole construction also had no soldered holes that could potentially ionise the water. The crystal

mount could therefore be connected to the 140 W diode cooling system (Section 5.2.1) which contained microchannels which required that only deionised water be used through them (Section 5.2.1).

The outside edges of the water-cooled mounts were cut at 45° on both sides in order to fit two fully mounted crystals close together in a two crystal, quadruple pumped set-up. The edges also allowed a 45° mirror to be placed very close to the two crystal mounts. The photo in Figure 5.3 shows such a set-up. Unfortunately the very high-powers in this laser, difficult crystal cleaning conditions and dust in the lab caused one of the crystals to become damaged during initial testing of this set-up and the experiments were abandoned. However, similar experiments are again planned for the near future.

5.2 Pump set-up and characterisation

This section focuses on the properties of the pump diodes, how we chose the pump focus size in the crystal and how we aligned the pump beam to obtain a certain profile at its focus.

5.2.1 Laser diode pump sources

The diode pump source determines the total amount of pump power available, the wavelength range and the pump beam quality. High power diode modules are usually the most expensive part of diode end-pumped systems, which makes their selection a critical design decision.

We used three laser diode modules in our experiments. Thermal lensing experiments were performed with a 140 W laser diode module (JOLD 140-CAXF-6A) and laser experiments with two 75 W diode modules (JOLD 75-CPXF-2P). All the diode modules were manufactured by JENOPTIK (2008) and were specified to operate at a wavelength (λ_p) of ~ 805 nm at full power and a cooling temperature of 18 °C. The outputs of the 140 W and 75 W diodes were delivered with multimode fibres with core diameters (d) of 600 μm and 400 μm respectively. All the fibres had a numerical aperture (NA) of 0.22.

The laser diode modules had to be cooled because of extra heat generated inside them from electrical resistance, carrier leakage and absorption. Water cooling is usually needed for high-power modules because tens to hundreds of Watts of thermal power is generated within them. The wavelength was also dependent on the junction temperature which made stabilising the diode temperature critical.

The 140 W diode had micro-channels close to the diode junction for better cooling. The cooling water first had to be distilled to protect these microchannels. The microchannels were also directly attached to the diode wafer. A leakage-current through the cooling system could therefore destroy the diode module. This implied that the cooling water had to be deionised below a certain level. The water therefore had to be regularly replaced since it became ionised over a relatively short period of time. The microchannels also caused a further complication in that only copper, certain stainless steels and plastic could be used in the coolant cycle. Using any other metal than copper would have formed a weak cell in the cycle that could have caused an electrolytic build-up in the microchannels. The two 75 W diodes had none of these problems since they were passively cooled with an external heat-sink so that tap water could be used through them.

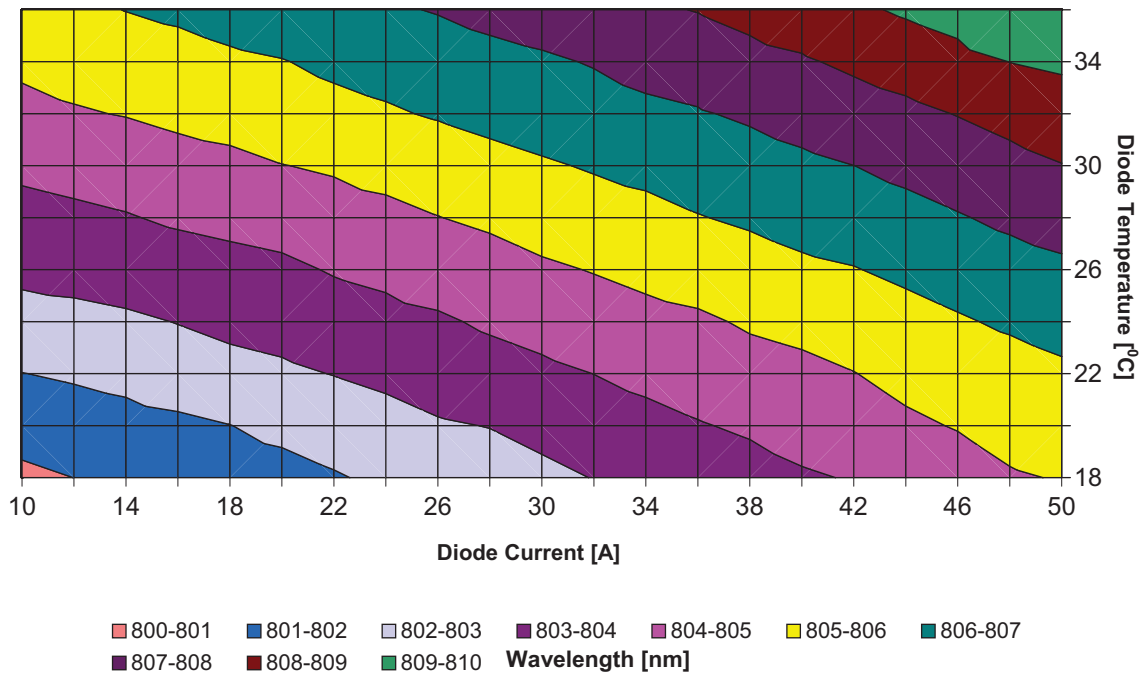

Figure 5.4: The average output wavelength in nm of the two 75 W diodes as a function of both current (x-axis) and temperature (y-axis) of the diodes.

The wavelength of the diode modules depended on both the cooling temperature and the current through them. This was because the temperature influences the thermal population distributions in the valence and conduction bands, which in turn influence the gain's maximum wavelength (Paschotta, 2009). Figure 5.4 illustrates the measured average wavelength of the two 75 W diodes as a function of both current (x-axis) and temperature (y-axis). The average wavelength could therefore be selected for a certain output power by adjusting the cooling temperature. For maximum absorption in both vanadates the wavelength had to be set to $\sim$ 808 nm (Section 2.5.1). The cooling temperature of the diode had to be raised to 30°C in order to optimise the absorption of the diodes at the maximum input current through them of 50 A. Similar measurements were performed for the 140 W diode module and it was found that its wavelength ranged from 805 nm at threshold, to 808 nm at a maximum current of 30 A when cooled at 30°C. We chose to optimise operation for maximum absorption at maximum output power. This was also a mistake in hindsight as will be seen in Section 7.4.5.

The optical fibres that were used to deliver the pump light from the diode to the optical table also homogenised and circularised it. By using the far field approximation it can be shown that the beam quality factor (M^2) of the pump beam exiting the fibre is approximately

given by

$$M^2 = NA\frac{\pi d}{2\lambda_p}, \tag{5.1}$$

where d is the diameter of the fibre-core and λ_p is the wavelength of the pump light. The pump light from the 140 W and the two 75 W laser diode modules had measured M^2 factors of 265, 149 and 137 respectively. This compared well with the values obtained with Equation 5.1 of 258 ($d = 600\,\mu$m, NA= 0.22 and $\lambda_p = 805$ nm) and 172 ($d = 400\,\mu$m, NA= 0.22 and $\lambda_p = 805$ nm)[1].

5.2.2 Pump focus size inside the crystal

In the next few sections we investigate the factors that determine the pump focus size inside the crystal and how we determined it for our set-up.

Absorption length

As a rule of thumb the pump beam size in the crystal is chosen so that its Rayleigh length inside the crystal is longer than the longest of the two absorption lengths ($z_R > \mathrm{Max}[(1/\alpha_{abs-a,c})]$). This is to ensure that most of the pump light is absorbed in the collimated part of the beam. The longest absorption length that was encountered in the vanadate crystals was ∼13 mm. This was for the σ-polarisation at threshold pump power when the diode laser wavelength was far away from the absorption peak at ∼ 808 nm. The Rayleigh length inside a crystal is equal to

$$z_R = \frac{n_{cr}\pi w_0^2}{M^2\lambda_p}, \tag{5.2}$$

where n_{cr} is the refractive index of the particular polarisation in the crystal and the w_0 is the waist radius.

When the values of Section 2.3.4 and 5.2.1 was inserted into Equation 5.2 it was determined that the beam radii should be chosen to be larger than 0.65 and 0.48 mm for the 140 W and 75 W diodes respectively.

Laser Efficiency

The threshold and slope efficiency of a four-level laser is given by

$$P_{thr} = \frac{\pi h\nu_p(w_l^2 + w_p^2)}{4\eta_{abs}\eta_{p\text{-}q}\sigma_{em}\tau_s}(T_{OC} + L_{ls}) \tag{5.3}$$

and

$$\eta_{slope} = \eta_{p\text{-}q}\frac{\nu_l}{\nu_p}\frac{T_{OC}}{(T_{OC} + L_{ls})} \qquad \text{for } w_p < w_l. \tag{5.4}$$

[1] The measurements were done at currents where the diodes just started to lase.

ν_{p} and ν_{l} are the pump and laser frequencies, w_{p} and w_{l} are the pump and laser radii and η_{abs} is the percentage of the pump power that is absorbed. $\eta_{\mathrm{p\text{-}q}}$ is the pump quantum efficiency which is the average number of ions in the upper laser level created per absorbed pump photon and varies between 0.59 to 0.85 in the literature. T_{OC} is the transmission of the output coupler and L_{ls} is the sum of all the other losses in the resonator such as scattering and diffraction losses. σ_{em} and τ_{s} are the effective stimulated-emission cross section and the lifetime of the upper laser level (Bollig, 1997).

It can be observed that the threshold increases with the square of the pump radius while the slope efficiency does not depend on the pump radius. This implies that four-level lasers with smaller pump radii are more efficient overall since they start lasing at lower pump powers and increase their output power with the same linear constant η_{slope}. The pump radius therefore have to be reduced as much as possible in order to increase the efficiency.

Thermal stresses

Another consideration is the thermal stresses inside the crystal. It is commonly believed that a pump beam that is large at the focus should be chosen in order to spread the heat load over a larger volume in the crystal, thereby reducing stresses. However, in an adaption of Yan & Lee (1994)'s work it has been shown in the thesis of Bernhardi (2008) (pp. 30) that the maximum stress in a cylindrical crystal is given by

$$\sigma_{\mathrm{max}} = C_{\mathrm{ind}} P_{\mathrm{abs}} (1 - \frac{w_{\mathrm{p}}^2}{2R_{\mathrm{cr}}^2}) \tag{5.5}$$

where w_{p} is the pump radius, R_{cr} the crystal radius, P_{abs} the absorbed pump power and C_{ind} a factor that does not depend on the pump radius. It is therefore not the absolute pump radius in the crystal that determines the maximum stress in the crystal, but rather the **ratio** of the pump radius to the crystal size. Figure 5.5 shows the radially dependent factor of the maximum tensile stress inside the crystal according to Equation 5.5.

When the entire crystal is pumped, the maximum stress intensity is 0.5× the radially independent part. This increases to 1× for very small pump sizes. The ratio can also not be increased above $\sim 2/3$ since this would lead to significant diffraction losses for the TEM_{00} mode (Hodgson, 2005 pp. 260). For pump to crystal ratios below 0.5 the maximum stress inside the crystal does not increase significantly and one can basically choose any pump size. The maximum tensile stress can therefore only be reduced by a factor of ~ 0.2 by varying the pump size. This was also experimentally proven by Yan & Lee (1994).

Thermal lensing

Another aspect to consider when choosing the pump spot is the thermal lens. According to Bernhardi (2008) the analytical temperature solution of a crystal pumped by a flat-top pump beam (Equation 3.23) has a dioptric power of

$$D = \frac{1}{f_{\mathrm{th}}} = \frac{dn}{dT} \frac{2\eta_{\mathrm{p\text{-}q}}\eta_{\mathrm{abs}}}{4\pi k_{\mathrm{th}} w_p^2}. \tag{5.6}$$

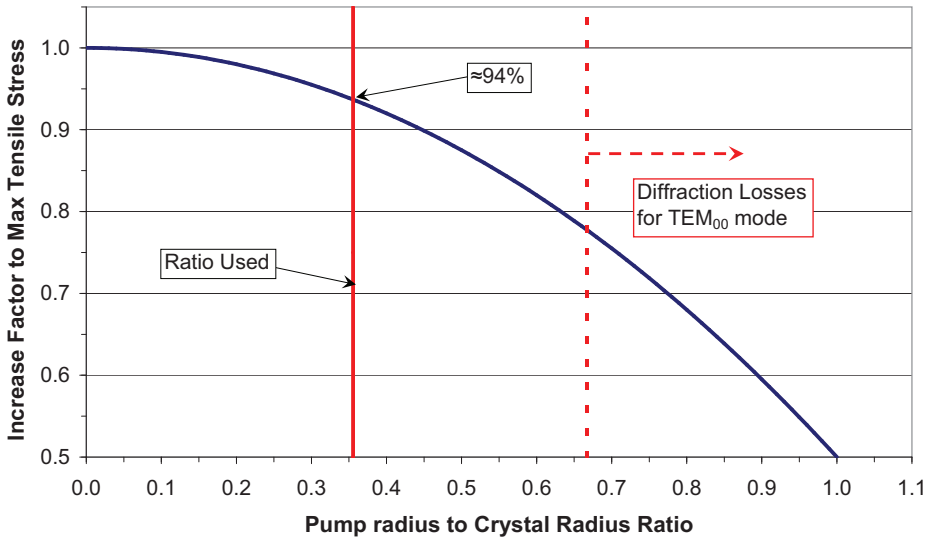

Figure 5.5: The radially dependent increase factor of the maximum tensile stress inside a cylindrical crystal.

All the symbols are the same as defined in Sections 2.3.3 and 5.2.2. The dioptric power is therefore very roughly inversely proportional to the square of the pump beam radius. The pump beam radius must therefore be made as large as possible to limit the influence of the thermal lens.

However, there is a second aspect of the thermal lens that one has to take into account. According to Magni (1986) and Section 3.7.1 the minimum the laser beam radius can be in the crystal is equal to

$$w_{\text{min-M}} = \frac{2\lambda_{\text{lr}}}{\pi} \frac{1}{|\Delta D_{\text{th}}|}, \tag{5.7}$$

where ΔD_{th} is the range of dioptric powers for which a laser is stable for a specific resonator configuration. $w_{\text{min-M}}$ is therefore inversely proportional to the variance in thermal lens dioptric power where a resonator is stable. This implies that for large pump radii ΔD_{th} is small, making the laser more sensitive to changes in thermal lens dioptric power. The pump radius must therefore be made as small as possible to make the resonator insensitive to changes in the strength of the thermal lens.

The two thermal lens factors therefore compete against each other in the choice of the pump beam radius.

Final choice of the pump beam radii

The final measured pump beam focus radii (using the second moment method) was 0.71 and 0.63 mm for the 140 W and 75 W diodes respectively. The size difference was small enough so that comparative experiments could be performed.

The Rayleigh lengths for the weaker absorbing σ-polarisation of the vanadates were both equal or longer than the 13 mm absorption length that was required. The Rayleigh length of the 140 W laser was close to the minimum in order to fulfil the absorption length condition (Section 5.2.2). The lasers that were pumped with it should therefore have been quite efficient according to Equation 5.3.

The stress in the crystal was not adversely affected by the pump beam size since the pump to crystal ratio was $\sim$0.35 (Figure 5.5). The only way to have a significantly reduced maximum stress in the crystal would have been to use thinner crystals. However, practically mounting and working with these crystals would have been difficult. The beam radii also caused thermal lenses in the 50 to 100 mm range which could easily be handled by the curved optics we had available.

5.2.3 Pump profile

The transverse profile of a diode pump beam changes as it propagates through a focus. This is different from beams from simple stable resonators which can generally be described as a linear combination of orthogonal Gaussian modes which have constant profiles as they propagate. The pump profile near the pump-face is the most influential since it is the position where the diode power is the highest due to the strong absorption of the crystal. The high refractive indices of the vanadates also spread out the pump beam inside the crystal so that a specific pump profile propagates over a longer distance than in air. We also experimentally found that end-pumped lasers are most efficient when the pump focus is placed close to the pump-face.

The most commonly used pump profile is a flat-top (also called top-hat) profile. It has the favourable quality of providing a roughly uniform pumping region which is easy to model. A flat-top profile also reduces the thermal aberrations because the heat load is constant over the pump-region. This leads to a roughly quadratic temperature profile inside the pump-region (Section 3.5).

A bell-shaped pump profile is not often used because it requires specialised alignment techniques. This profile matches better with that of a TEM_{00} laser mode profile so that intuitively it can be expected to produce a more efficient, good beam quality lasers with lower thresholds. The threshold will also be lower for bell-shaped pump profiles since most lasers are TEM_{00} at threshold due to higher gain in the centre of the pump-region. The pump and laser TEM_{00} mode profiles also matches better spatially. However, this profile causes stronger spherical aberration in the crystal. From Section 3.5 it can be predicted that the spherical aberration would be in-between that of a flat-top and a Gaussian pump beam with the same pump beam radius. In many cases the advantage of the higher slope efficiencies often outweighs these extra thermal liabilities. We chose to perform all our experiments with a bell-shaped profile because the results could be used to build efficient high-power lasers. In the next section we will focus on how to align the pump relay system to obtain a bell-shaped profile at the pump focus position.

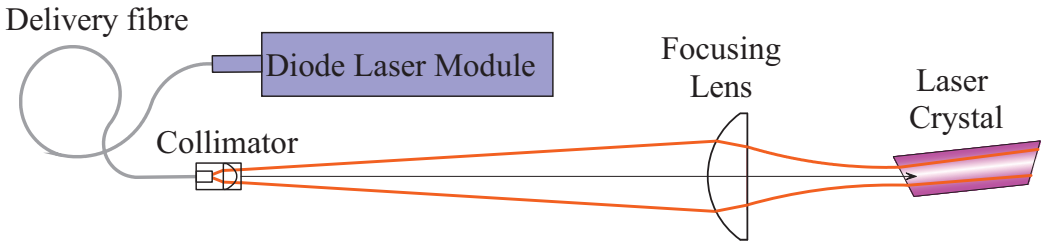

Figure 5.6: The pump collimation and focusing relay system that was used in all the experiments in this study. The distances are taken to and from the principle points of the lenses.

5.2.4 Pump collimation and focusing

A popular relay system from the fibre-end to the crystal is the imaging set-up. Two medium focal length lenses are used in close proximity to each other to image the fibre-end into the laser crystal. The beam profile in the crystal will then have a flat-top shape which is an image of the multimode output of the fibre-end. If one-to-one imaging is used the beam diameter in the crystal will be equal to the multimode fibre-core diameter.

We opted to rather use a collimation and focusing set-up as is illustrated in Figure 5.6. The light exiting the fibre is highly divergent due to the high M^2 values of the pump beams (Section 5.2.1) and relatively small fibre-core diameters. A strong lens with a short focal length is therefore used to collimate the output beam from the fibre. The collimated beam is then focused into the crystal with a focusing lens with a longer focal length.

To obtain a bell-shaped profile at the crystal focus, a flat-top profile must be formed on the focusing lens by **imaging** the uniformly radiating multimode fibre-end onto it with the collimating lens. The focusing lens then converts the uniform (flat-top) input profile into a spatially compressed profile at its focal plane which is the Fourier transform of the input profile on it (Siegman, 1986 pp. 707-708). The Fourier transform of the flat-top beam is a first order Bessel function which consists of a high central bell-shaped peak surrounded by weaker rings (Hecht, 1998 pp. 523-524). Most of the power is located in the central intensity peak so that the rings can be ignored in pumping applications. The pump profile at the crystal focus position is therefore effectively bell-shaped.

5.2.5 Pump characterisation

The size and position of the pump beam focus behind the focusing lens were characterised with a CCD camera by measuring the pump beam radius at a number of positions through the focus. Figure 5.7 illustrates such a measurement of the 140 W pump beam radii near the focus. The measurement positions are corrected for propagation in the c-direction (for the π-polarisation) of an 18 mm long Nd:YVO_4 crystal. The distances are given relative to the pump-face and the z-position of the pump in the crystal was then experimentally determined for the lowest threshold.

Figure 5.7 illustrates how the crystal stretched out the pump beam because of its larger refractive index. Also shown are the scaled π-profiles of the pump beam as it was absorbed

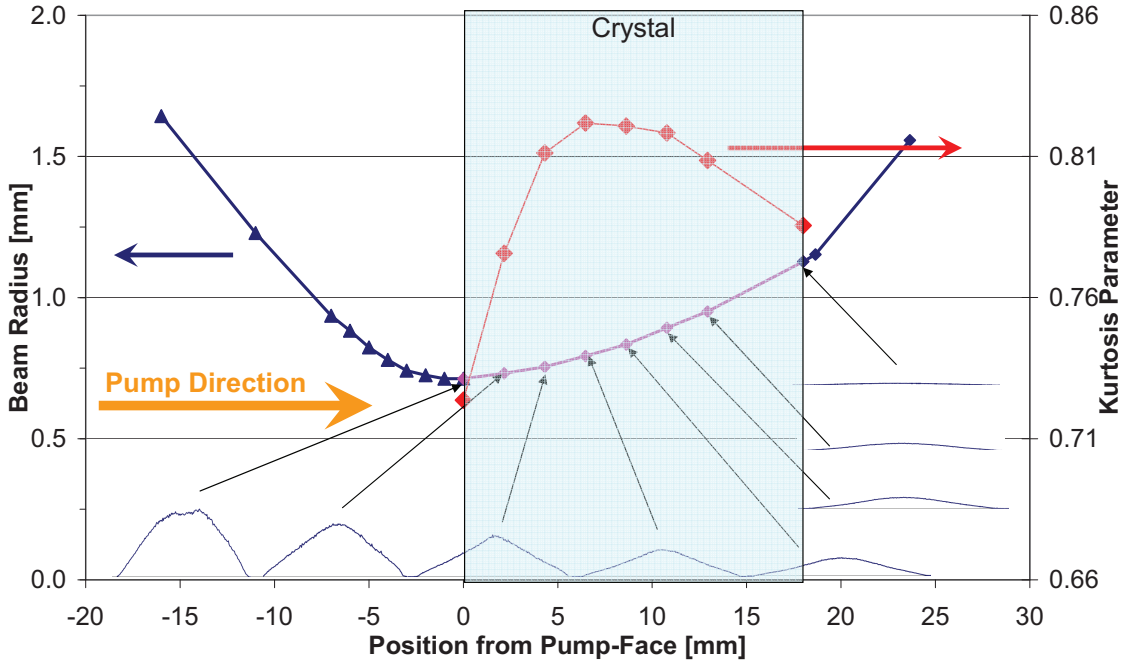

Figure 5.7: The pump beam propagation into a 0.15% doped Nd:YVO_4 crystal is shown in blue (and pink inside the crystal) on the left axis. Also illustrated are the pump profiles in the stronger absorbing *c*-direction. The kurtosis parameters for these profiles are shown in orange on the right axis.

in the stronger absorbing *c*-direction inside the 0.15% doped Nd:YVO_4 crystal. The pump profile clearly changed as the pump propagated into the crystal. At the pump-face it was roughly bell-shaped with a small vestige of a flat-top. It then evolved into a cone-shaped profile which again gradually became bell-shaped as it propagated through the crystal.

The evolution of the pump profile could be quantified by the kurtosis parameter K_s which is plotted in red in Figure 5.7 on the right axis. K_s is defined as (Mei & Zhao, 2007)

$$K_s = \frac{\langle r^4 \rangle}{3\langle r^2 \rangle^2} \tag{5.8}$$

where

$$\langle r^2 \rangle = \frac{\int I(r - \langle r^1 \rangle)^2 dr}{\int I dr} \tag{5.9}$$

is the 2nd intensity moment and

$$\langle r^4 \rangle = \frac{\int I(r - \langle r^2 \rangle)^4 dr}{\int I dr} \tag{5.10}$$

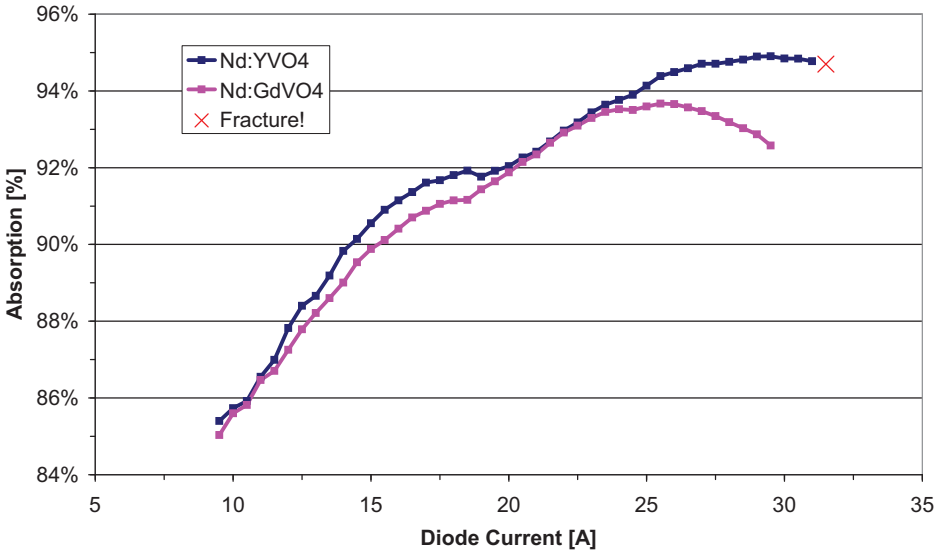

Figure 5.8: The total absorption of the 140 W diode in 0.15% doped 20 mm long Nd:YVO_4 and Nd:$GdVO_4$ crystals with a 0.71 mm pump beam size. The fracture point in the Nd:YVO_4 crystal is indicated with a red cross.

is the 4^{th} intensity moment. $\langle r^1 \rangle$ is the 1^{st} intensity moment and is defined in a similar manner.

The kurtosis parameter is a measure of how "sharp" a beam profile is. K_s is 1 for a perfect Gaussian profile and 0.6 for a perfect flat-top one. It is therefore a good indication of the shape of the beam. Most fibre-coupled diode pump beams have a kurtosis parameter somewhere in between these two extremes.

The measured beam profile at the pump face had a K_s of 0.72 which indicated that it was more flat-top. It then reached a maximum value of 0.82 roughly 5 mm into the crystal. This coincided with the cone-shaped profile which indicated that even though the cone appeared "sharper" than a Gaussian profile its "sharpness" was actually roughly in-between that of a flat-top and a Gaussian profile. Similarly changing beam profiles is usually also observed for the flat-top diode end-pumped profiles described earlier (Section 5.2.3).

5.2.6 Pump absorption and the fracture limit

Figure 5.8 shows the total absorption of the 140 W diode laser (cooled at 30°C) in the 0.15% doped, 20 mm long Nd:YVO_4 and Nd:$GdVO_4$ crystals as a function of the current through the diode laser module. The pump beam size in the crystal was 0.71 mm and the cooling mount of the crystal was kept at 25°C. The power was incrementally increased and the absorption measured at each step. Similar absorption curves were obtained for the 18 mm long crystals and measurements were also carried out using the two 75 W diodes. The absorption curves in Figure 5.8 can be explained with the help of the absorption spectra (Figure 2.5) and the wavelength variance of the diode laser with current through it (Figure 5.4). The absorption

increased and peaked as the wavelength (which increased with current) increased to 808 nm (at ∼27.5A). The absorption length therefore decreased with power so that the heat load shifted to the front of the crystal. The valley between the two peaks at 806 and 808 nm could just be resolved in the polarisation combined convolution of the broad diode laser spectrum and the absorption spectra of the vanadates.

A 20 mm Nd:YVO_4 crystal was slightly damaged on one side during mounting so that the other undamaged side could be used for the destructive testing. This was therefore done by performing absorption measurements on it until thermal fracture was observed in the crystal, thereby establishing its fracture limit. All the other experiments in this thesis were then performed at lower pump powers. The maximum tensile stress in the crystal at which fracture occurred was subsequently determined with FEA calculations and is presented in Section 7.4.5.

5.2.7 Single and double end-pumping

Table 5.1 summarises the properties and focusing characteristics of the three pump sources. Thermal lens measurements were performed by pumping the crystals with the 140 W diode from only one side (single-side end-pumping). Data from these single-side end-pumped experiments could be used to design lasers with strongly absorbing crystals that were pumped from two sides (double end-pumping). The strong absorption in the vanadates effectively separated the two sides of the crystal so that it could be approximated as two thin lenses located on the two pump-faces.

A single crystal can absorb more pump power if it is pumped from both sides. This is because the main factor that limits the amount of power that can be extracted from a crystal is its fracture limit. Fracture almost always occurs close to the pump-face because that is where the heat load is highest due to the absorption. By pumping from two sides, a highly absorbing crystal is able to absorb a little bit less than twice the power that it is able to absorb from only one side. We therefore used double end-pumping to investigate how much power could be extracted from a single crystal.

Two 75 W diodes were used for this purpose (Section 5.2.1). The set-up of the pump focus size and profile was identical to that described in Section 5.2.4. One of the 75 W pumps was aligned into the centre of the crystal and its z-position adjusted for lowest threshold. The other 75 W pump was then also aligned into crystal from the other side. The x, y and z-positions of its focus was then adjusted for the lowest threshold in an already optimised single-side end-pumped resonator. The *HeNeprobe*-positions of both pumps was then adjusted at full pump power until the highest lasing output power was achieved.

5.3 Laser alignment

Once the pump beam was set up and characterised the crystal could be positioned on the optical table. Two HeNe lasers were first aligned collinear, counter-propagating and parallel to the edge of the optical table in order to define the optical axis inside the crystal. The crystal was then orientated and centred with these HeNe lasers.

Properties	Pump Source 1	Pump Source 2	Pump Source 3
Manufacturer's #	JOLD-75-CPXF-2P	JOLD-75-CPXF-2P	JOLD-140-CAXF-6A
Max Power [W]	140	75	75
Max Current [A]	40	50	50
$\lambda_{\text{dio-min}}$ @ 30°C [nm]	804.65 @ 8A	804.31 @ 10A	804.25 @ 10A
$\lambda_{\text{dio-max}}$ @ 30C [nm]	807.89 @ 30A	807.91 @ 50A	808.03 @ 50A
d [μm]	600	400	400
NA	0.22	0.22	0.22
M^2 (measured)	265	149	137
Slope eff. [W]	$P = 4.05I_{[W/A]} - 33.05_{[W]}$	$P = 1.54I_{[W/A]} - 12.04_{[W]}$	$P = 1.41I_{[W/A]} - 10.71_{[W]}$
w_p in crystal [mm]	0.71	0.65	0.67

Table 5.1: Summary of the properties of the diode pump sources that were available to us, as well as their focusing characteristics.

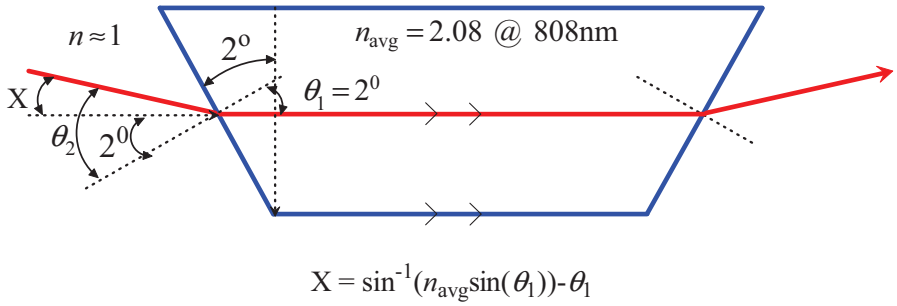

Figure 5.9: The angle X with respect to the side cooled edges of a wedged crystal to which a pump beam must be aligned in order to propagate parallel to them.

The angle of both HeNe lasers were then adjusted so that they coincided with the angle at which the pump beam would be diffracted (by the wedged pump face) so that it is parallel to cooled sides of the crystal. This angle was determined from Snell's law (Hecht, 1998 pp. 101) and an illustration of this can be seen in Figure 5.9. Due to the birefringence the average value of the two refractive indices at 808 nm had to be used to obtain an average angle for the two polarisations.

Two 45° laser mirrors (HR 1.06 μm HT 805 nm) were then inserted on both sides of the crystal. Only the right HeNe laser was subsequently used to align a flat-flat construction laser which consisted of two flat mirrors (M_2 and M_4 in Figure 5.10), each with relatively high reflectivity for the laser wavelength. The positive thermal lens inside the crystal made the flat-flat resonator configuration stable. The unpolarised HeNe was split in two by the birefringence of the crystal. The polarisation of the construction laser could therefore be chosen as either π or σ by aligning the appropriate 632 nm reflection from M_2 back into the HeNe laser.

A lower reflectivity flat output coupler (M_5) with a 70% reflectivity at 1.06 μm was then

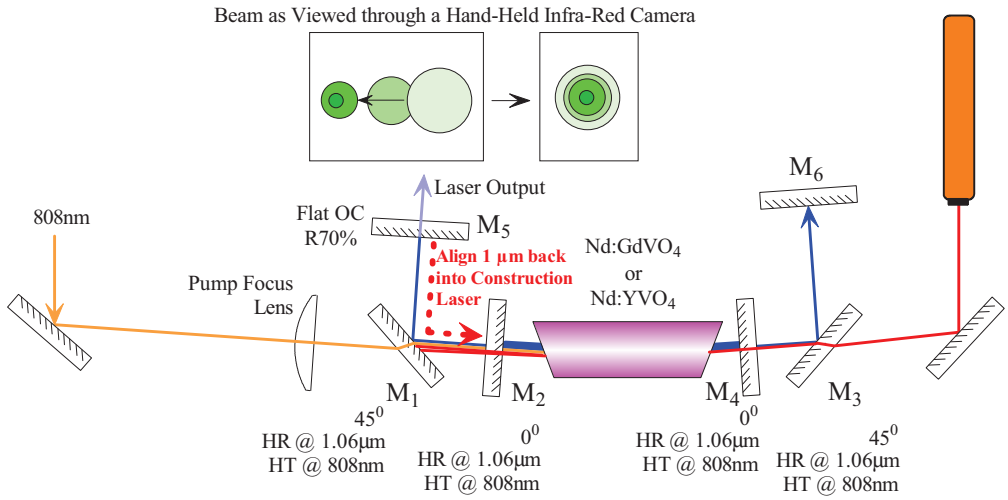

Figure 5.10: An illustration of the alignment of a construction laser that was used to build a more complex resonator.

inserted in the path of the construction 1.064 μm output beam reflected off the left 45° laser mirror M_1. M_5 was then roughly adjusted so that the part of the beam that was reflected from it was aligned back into the construction laser. The transmitted part of the beam through M_5 then consisted of a line of spots that were caused by multiple reflections between M_5 and M_2, as is shown at the top of Figure 5.10. M_5 was then adjusted so that all the spots overlapped, which meant that M_5 was aligned with respect to the optical-axis of the construction laser.

M_2 was then removed and the pump power was increased until lasing was observed from M_5. The new laser was optimised for lowest threshold which was considerably higher than the one of the construction laser due to the extra losses from M_5 which had a higher transmission than M_2. This new laser became the new second construction laser that was used to align all the resonators that was employed in this study.

The right arm of the resonator was lengthened in order to apply the resonator quenching method (Section 4.2.1). A 0° HR laser mirror (M_6 in Figure 5.10) was positioned behind the right 45° HR laser mirror M_3. This was done with exactly the same construction laser method as was used to align M_5. The position and orientation of M_4 were carefully marked so that the right arm could be easily adjusted between measurements by quickly reassembling the second construction laser.

The flat back reflector (M_6) was replaced with various curved ones to implement the new mode-matching method. These curved mirrors could also be located at various distances from mirror M_3 (Section 4.2.3). The resulting three element laser system oscillated if it was stable for a specific thermal lens focal length according to the stability criterion provided by Magni (1987).

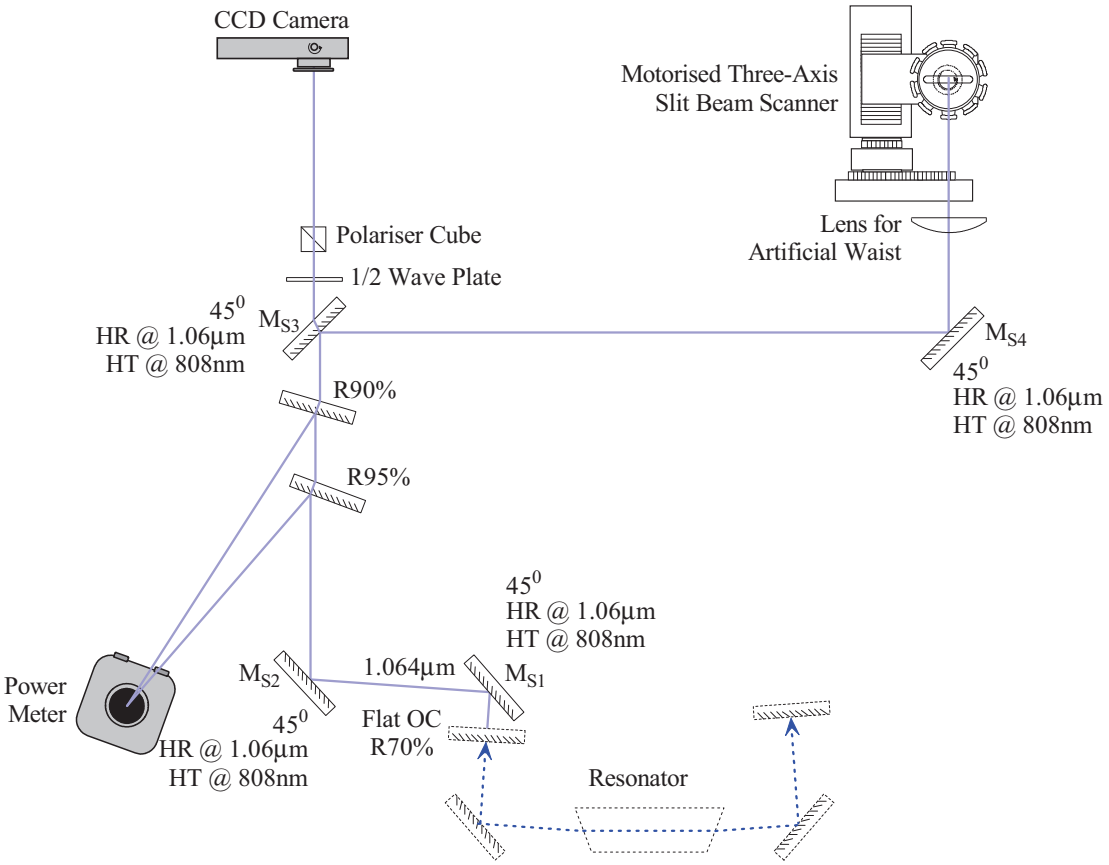

Figure 5.11: The 1.064 μm high power diagnostic set-up, which consisted of partial reflectors, a power meter, attenuation optics, a CCD camera and a three-axis slit beam scanner.

5.4 Diagnostic set-up

The diagnostic set-up which is described in the following section involved measuring the characteristics of both the laser beam at 1.064 μm and the probe beams at 632.8 nm.

5.4.1 High power 1.064 μm laser beam diagnostics

The diagnostic set-up to analyse the 1.064 μm output beam of a high-power laser is illustrated in Figure 5.11. The beam behind M_5 was steered with two 45° HR laser mirrors (M_{S1} and M_{S2}) onto two partial reflectors (95% and 90% reflectivity at 1.06 μm) which reflected most of the power of the laser beam onto a LM-200-HTD Coherent power meter (Coherent, 2009). The power meter measured the output power and also acted as a beam dump.

The remaining part of the beam was then steered with two other 45° HR laser mirrors (M_{S3} and M_{S4}) through a 300 mm focal length lens onto a motorised three-axis beam scanner. The beam scanner was built in-house and utilised the slit scanning technique to measure the

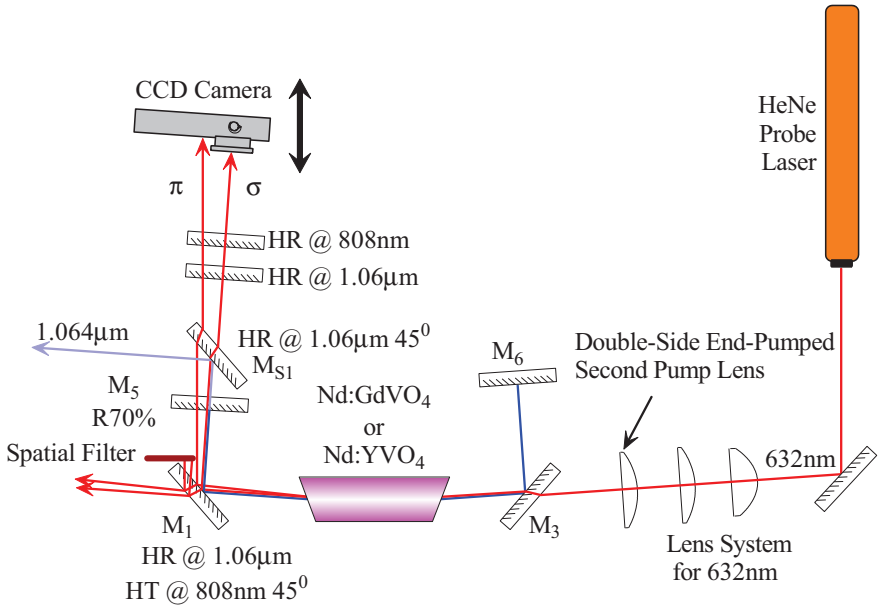

Figure 5.12: The probe diagnostic setup, which consisted of an unpolarised HeNe laser, a beam shaping system, a crystal, optics to remove the 1.064 μm laser and 808 nm pump radiation as well as a CCD camera.

beam profiles in both the x and y-directions at various z-positions. The beam quality (M^2) factors in the two transverse directions could then be obtained by using the second moment method to calculate the laser beam radii (ISO11146, 1999) and fitting the Gaussian beam propagation equation to them. The beam quality factors were used in both of the resonator method thermal lens measurements, but they were especially important in the mode-matching method (Section 4.2.3).

The small percentage of the beam that was transmitted through M_{S3} was further attenuated with a variable attenuator (consisting of $\lambda/2$ wave plate and a polariser cube) before being detected by a 1/2" LaserCam IIID beam diagnostics camera from Coherent (Coherent, 2009). The beam profile was monitored and recorded with the CCD camera and also provided the beam radii in the x and y-directions. These beam radii were then primarily used to improve the accuracy of the mode-matching method (Section 4.2.2).

5.4.2 HeNe probe diagnostics

The same 632 nm HeNe beam that was used to align the laser (Section 5.3) was used to probe the the crystal to measure the strength of the thermal lens at this wavelength (Section 4.3.1). The 632 nm beam was propagated through three lenses before it entered the crystal. At the time we also wanted to have the option to do comparative measurements with a double pumped set-up. The 632 nm beam therefore had to be propagated through a 808 nm pump focus lens on the right. The position of this pump lens is indicated in Figure 5.12. Two other

lenses were then needed so that the 632 nm beam had roughly the same size as the 808 nm pump beam focus size in the crystal. However, it was not possible to collimate the 632 nm probe beam due to the extra pump lens. The beam could only be made slightly divergent with the desired radius of ∼0.7 mm in the crystal.

The wedged birefringent crystal then split the HeNe probe beam into an ordinary (o) and an extraordinary (e) beam. The 632 nm probe beams reflected off M_1 were separated from the 1.064 μm laser beam behind M_5 by means of the 45° HR laser mirror (M_{S1}). 0° HR's for both the laser and the pump wavelengths were then inserted behind M_{S1} to ensure that only the 632 nm beams were detected by a CCD camera. The same camera that was used for the 1 μm diagnostics was moved here. The thermal lens strongly focused the probe beams which meant that the camera had to be shifted to shorter distances when one of the probe beams became larger than the CCD array.

The e and o-beams (π and σ-polarised respectively) propagated at different angles due to the birefringence of the wedged crystal (Section 4.3). The CCD camera had to be shifted horizontally to measure either the π or σ-thermal lenses. The π-polarisation has a larger refractive index in both vanadates and is refracted more strongly. Figure 5.12 illustrates that the left beam on the CCD camera was therefore the π-polarisation.

5.5 Complete thermal lens measurement set-up

The entire thermal lens measurement set-up consisted of the pump set-up (Chapter 5.2), resonator (Section 5.3), 1.064 μm laser diagnostics (Section 5.4.1) and probe beam diagnostics (Section 5.4.2) and is shown in Figure 5.13. The curvature and position of of M_6 could easily be changed to measure the thermal lens with either the quenching method (Section 4.2.1) or the mode-matching method (Section 4.2.3). Probe beam measurements with the HeNe laser could be done concurrently with either of these resonator measurements or could be done separately. With this single set-up the following parameters could be determined:

- The two-dimensional beam profile.
- The beam quality factors M_x^2 and M_y^2.
- The maximum output power and slope efficiency of multimode and TEM_{00} lasers.

The thermal lens could be determined when the resonator was

- non-lasing or lasing, on either the
- π and σ-polarisations, during
- multimode or TEM_{00} operation.

Results from the different measurement methods could also be directly compared with each other by using this set-up.

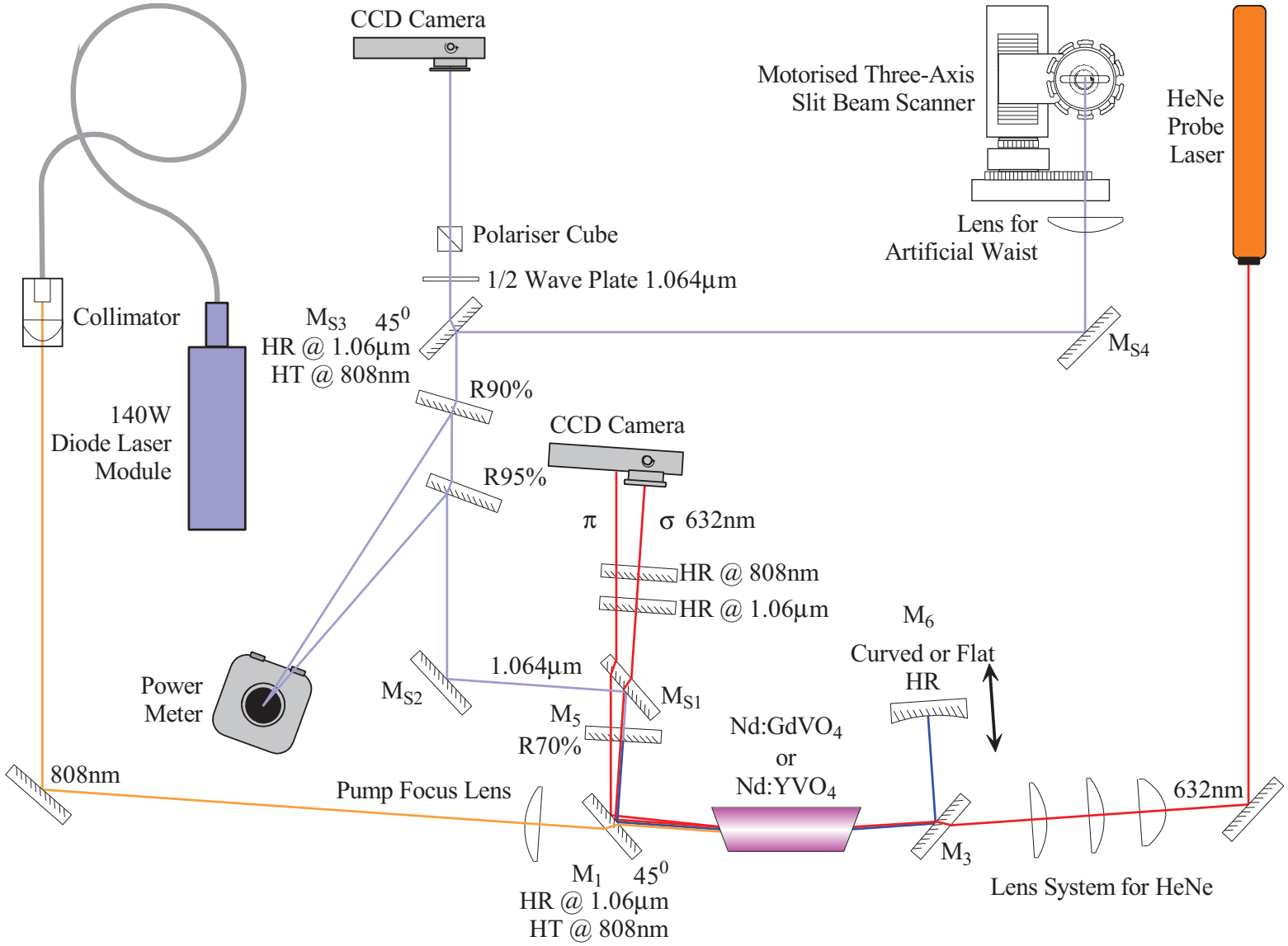

Figure 5.13: Complete set-up to measure thermal lens strengths with all three methods described in Sections 4.2.1, 4.2.3 and 4.3.1.

5.6 Conclusion

The crystal mounting, pump set-up, laser alignment, 1.064 μm diagnostics and probe beam diagnostic set-ups were combined to measure the thermal lens of both single and double end-pumped systems. This was done with the quenching, mode-matching and probe beam methods that were described in Chapter 4. In the next chapter we present the experimental results of these measurements.

Chapter 6

Experimental results and discussion

6.1 Introduction

This chapter presents the results of the thermal lens measurements using the quenching, mode-matching and probe beam methods that were described in Chapter 4. We evaluate all of these methods before we present the actual thermal lens results since they were either not described in the literature or our results differed from those reported. We also present results from double end-pumped lasers which we used to investigate how much power we could obtain in multi and TEM_{00} mode operation.

6.2 Results of the quenching method

The quenching method was discussed in Section 4.2.1 and we used it in this study to pre-evaluate the thermal lensing in the two vanadates. A number of publications reported that the slope efficiencies of flat-flat quenching resonators have two peaks but as yet no one has explained the phenomenon (Lancaster & Dawes, 1998; Sennaroglu, 1999; Song *et al.*, 2002). In the next section we attempt to explain this behaviour by carefully measuring the slope efficiency, M^2 values and 2D camera profiles at various pump powers.

6.2.1 Evaluation of the quenching method

A typical flat-flat, double end-pumped quenching resonator with a long arm length (L_2 in Figure 4.1) of 219 mm and a short arm length (L_1) of 6 mm was used to investigate the quenching process. Figure 6.1 illustrates the laser output power (on the left axis) and the M^2 values (right axis) in the horizontal (x) and vertical (y) directions as functions of the total absorbed diode end-pumped power. 2D beam profiles measured with a CCD camera are also plotted on the edges of the graph.

It can be observed from Figure 6.1 that the laser output power increased linearly at low pump powers. The beam started off as a TEM_{00} Gaussian shaped profile at 9.2 W which corresponded to a M^2 value of $\sim$1.

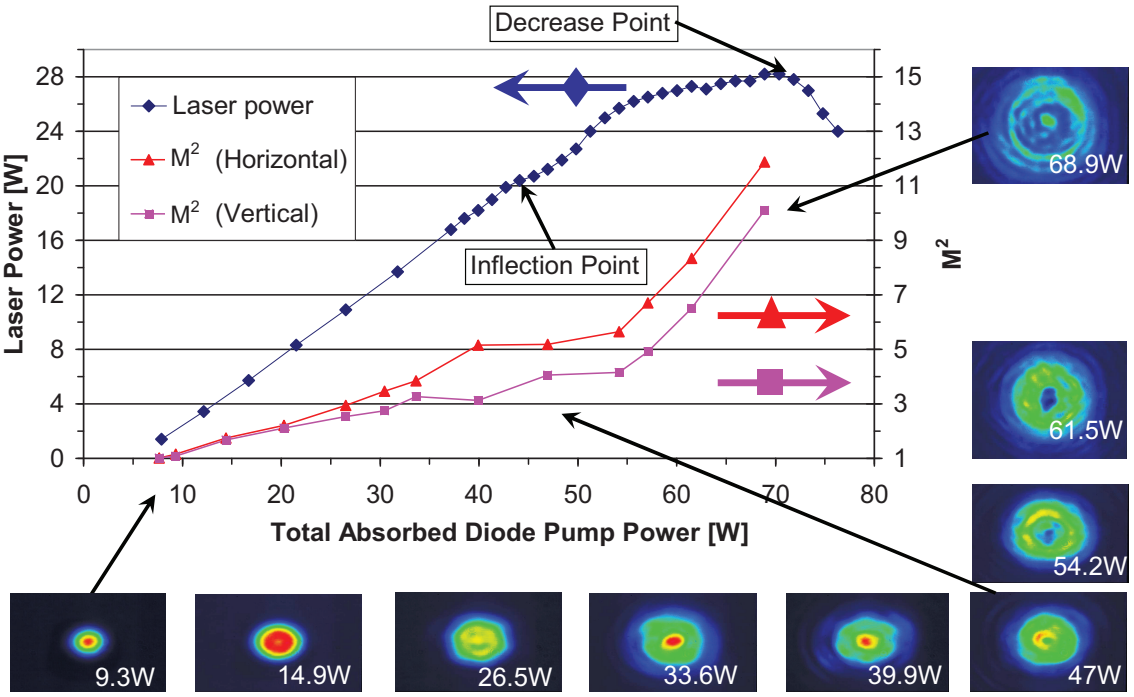

Figure 6.1: The laser output power (blue diamonds, left axis), M^2 values (red triangles and pink squares, right axis) and 2D beam profiles of a double end-pumped, 0.15% doped Nd:YVO_4, flat-flat resonator with a long arm length of 219 mm (and a short arm length of 6 mm).

The M^2 value subsequently increased linearly as the pump power was increased and the gain increased above threshold in the outer parts of the pump-region. The beam also acquired a significant higher mode content which can clearly be observed in the 2D beam profiles. At an absorbed diode pump power of roughly 40 W the M^2 values in the x and y-directions started to diverge substantially from each other. The 2D profiles also illustrate that the beam developed wings in the horizontal direction, indicating that the thermal lens in the horizontal direction was slightly stronger. This asymmetry of the thermal lens is due to the different thermal conductivities in the transverse directions (Section 2.3.3). The quenching method can therefore detect asymmetrical thermal lenses, which is a new result that has not yet been reported in the literature.

As the pump power was further increased the laser output power dipped slightly to form an inflection point at roughly 45 W. The 2D profile manifested a decreased intensity in the centre of the beam (or hole) which increased in size as the power was increased. This is because the radial rate of the phase change was less in the outer aberrated part of the thermal lens, which remained stable, while the inner part started to quench. The hole quickly developed into a zero intensity area that spanned the entire central part so that the beam profile resembled a doughnut. The hole can therefore potentially be used to determine the extent of the unaberrated part of the thermal lens by back calculating its size into the crystal (Section 4.2.2). After the inflection point the laser output power returned to almost the value

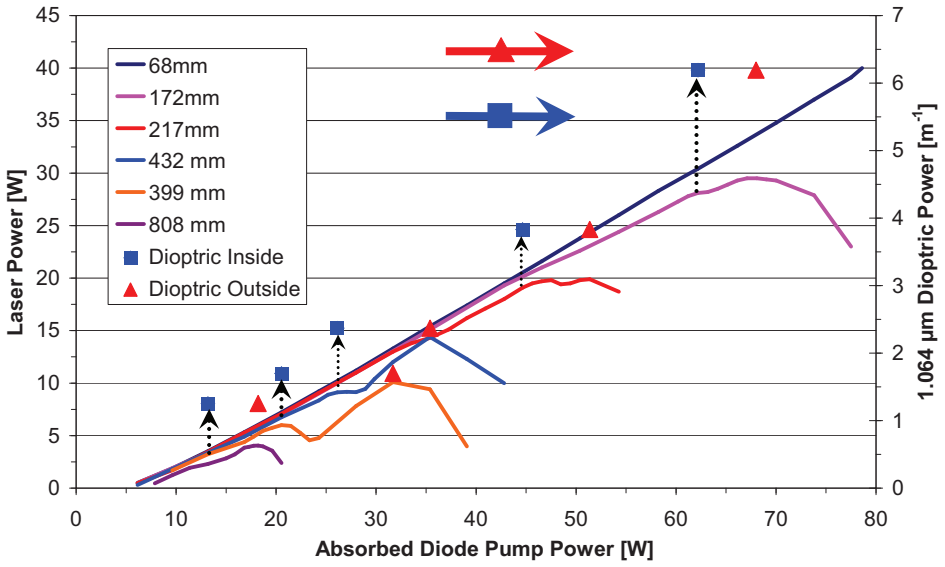

Figure 6.2: The output powers a function of single-side absorbed diode pump power of several flat-flat resonators with different long arm lengths L_2 (solid lines, left axis) and their corresponding derived central dioptric powers (discreet points, right axis). The short arm length was 6 mm)

it would have been without the inflection point. This indicates that the doughnut mode extracted the gain from the crystal almost as efficiently as the previous multimode beams did.

At a total absorbed pump power of 55 W the M^2 values in both directions increased sharply, which coincided with a decrease in laser output power and indicated that the outer part of the beam also started to quench (Sennaroglu, 1999). This quenching did not coincide with a sudden decrease in laser output as the literature would lead one to expect (Lancaster & Dawes, 1998). Rather, the laser output power remained relatively constant for a considerable pump power range before it decreased. This indicated that the outer aberrated part gradually quenched from the inside outwards. This can also be observed from the decreasing intensity of the 2D doughnut profile after 61,5 W and the multiple ring structure at 68.9 W. This result is therefore a confirmation of the theory of Section 3.9 which predicts a lower rate of phase change in the outer part. Above 69 W the output power dropped sharply down to zero (the decrease point) which implies that both the central non-aberrated and outer aberrated parts of the resonator became unstable.

Both the inflection and decrease points can be used to obtain information about the inner unaberrated and the outer aberrated part of the thermal lens respectively. Figure 6.2 plots the laser output powers of several flat-flat resonators with different long arm lengths L_2. A single-side end-pumped Nd:YVO_4 crystal was used in the flat-flat resonator. The values of the 1.064 μm quenching dioptric powers were determined by taking the inverse of the long arm lengths (L_2's) which included the optical path length in the crystal.

The pump power level where the central unaberrated part of the thermal lens was

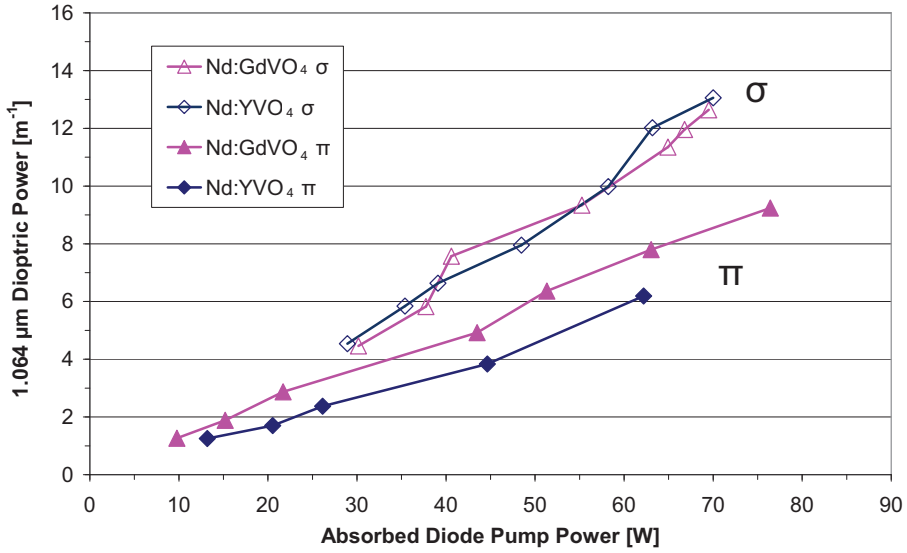

Figure 6.3: The unaberrated dioptric powers determined with the quenching method for both polarisations of a 0.15 % doped, single-side end-pumped Nd:YVO_4 (blue diamonds) and Nd:$GdVO_4$ (pink squares) crystals as a function of absorbed diode pump power.

quenched was determined by noting the pump power level of the inflection point. This relation is indicated in Figure 6.2 by the broken black arrows between the inflection points and associated dioptric powers. The resonator with the long arm length L_2 of 68 mm showed no inflection point, which indicated that it was never quenched in the pump power range that was used. The slope efficiency of this short resonator then served as the reference to identify the inflection points of the other resonators by observing the point where their slope efficiencies started to deviate from it. The dioptric powers derived from the inflection points are very valuable when designing high-power TEM_{00} lasers since matching of the laser mode with the pump-region only occurs inside the unaberrated part (Section 4.2.3). However, they are not suited for accurate thermal lens measurements since they can be difficult to identify.

The average dioptric power of the outer aberrated part of the thermal lens at certain absorbed pump powers could also be determined in order to estimate how the aberrations acts as a soft aperture for the TEM_{00} mode in other resonators (Section 3.9). This was done by noting the pump power level of the decrease point. The range of the dioptric powers between the unaberrated value and this value provides a good indication of the variation of the dioptric powers over the aberrated gain cross section. From the values illustrated in Figure 6.2 we derived that there was a maximum dioptric power difference in thermal lensing of $\sim$1 between the inner and outer parts of the thermal lens.

6.2.2 Thermal lens results determined from the quenching method

Figure 6.3 plots the dioptric powers of the inner unaberrated part of the thermal lens for both polarisations of Nd:YVO_4 and Nd:$GdVO_4$. It can be observed that Nd:YVO_4's π-polarisation

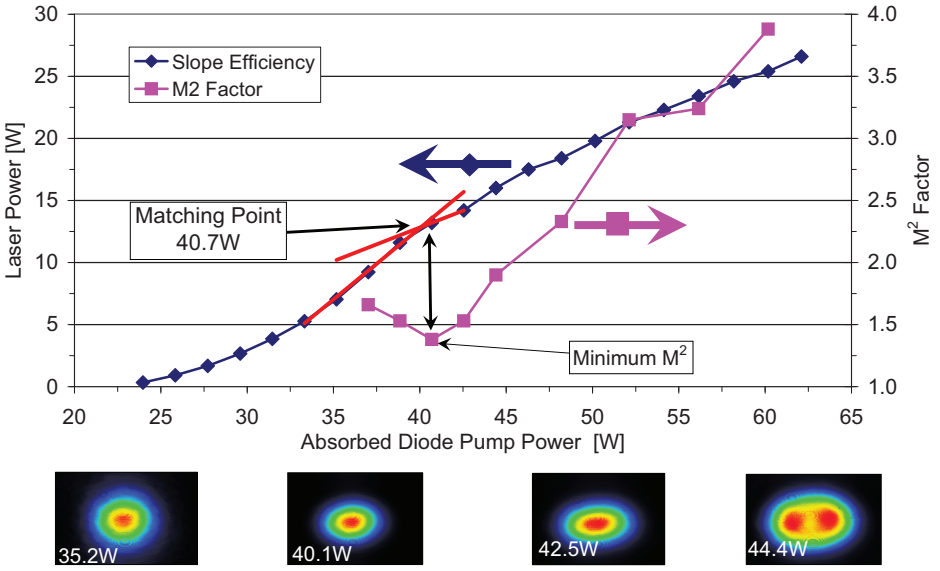

Figure 6.4: The laser output power (blue, left axis), M^2 factors (pink, right axis) and selected camera profiles (bottom)over a range of total absorbed pump powers of a typical double pumped concave flat resonator that was used to evaluate the mode-matching method.

(with the stronger gain) has slightly weaker thermal lensing than its equivalent in Nd:$GdVO_4$. The thermal lensing of the σ-polarisations of both materials were almost twice as strong as for the respective π-polarisations. However, the difference between the two material's σ-thermal lenses was less than the measurement error. We were therefore unable to conclude which material had the stronger thermal lens on this polarisation. This is in any event only of academic interest since one would rather choose one of the vanadates by the properties of its π-polarisation because of its stronger gain and weaker thermal lens. Figure 6.3 therefore indicates that Nd:YVO_4 has more favourable thermo-optical properties than Nd:$GdVO_4$ at 1.064 μm.

6.3 Results of the mode-matching method

The novel mode-matching method (Section 4.2.3) is more reproducible than previous methods because it only measures the central relatively unaberrated part of the thermal lens.

6.3.1 Evaluation of the mode-matching method

The method was evaluated by also comparing M^2 measurements, 2D beam profiles and the laser output power as functions of the total absorbed diode pump power. A double-end-pumped CV-flat resonator with a 250 mm radius concave back-reflector at a distance of 338 mm from a Nd:YVO_4 crystal (L_2 in Figure 4.4) was used to evaluate the method. The crystal was 49 mm from a 70% flat output-coupler (L_1). Figure 6.4 depicts the laser output power (blue diamonds, left axis) and $x-y$ averaged M^2 factors (pink squares, right axis) as

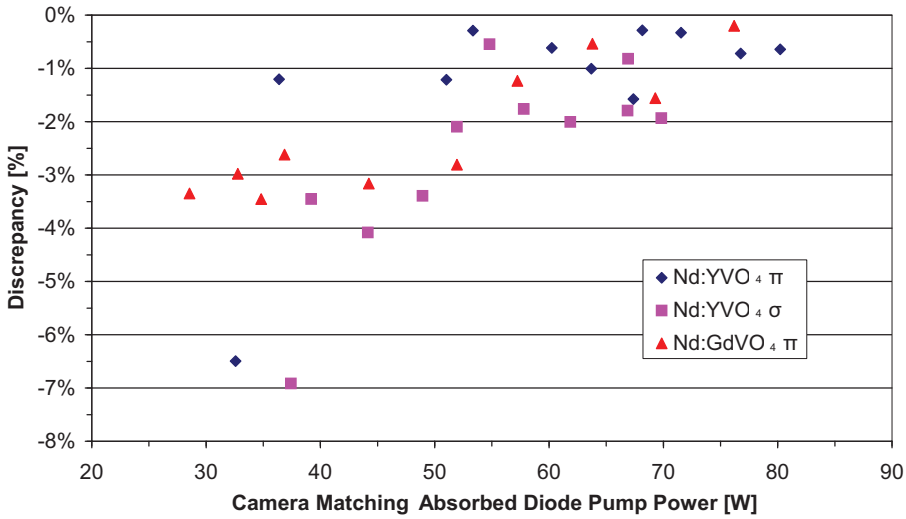

Figure 6.5: Discrepancy of using the intersection points of two linear fits on both sides of the linearisation region near matching instead of monitoring the peaking of the central intensity on a CCD camera.

functions of the total absorbed diode pump power. It also shows a few selected 2D camera profiles at the bottom of the graph. We could therefore compare the different data sets to analyse the matching of the laser mode with the pump mode.

The behaviour of the laser output power can be explained as follows: The laser only started oscillating at a high absorbed pump power of $\sim 24\,\mathrm{W}$ when $f_{\mathrm{th}} \geq \mathrm{L}_2$. This is at a much higher pump power than the threshold would be for resonators that are stable for long thermal focal lengths like the flat-flat resonators of the previous section. A large gain was available when the laser started to oscillate and as the diffractive losses decreased with increasing pump power the laser output increased sharply up to a total absorbed pump power of $\sim 40\,\mathrm{W}$. The local slope efficiencies in this region was significantly higher than for the multimode extraction encountered in short, flat-flat resonators because of the sudden decrease in losses. At $\sim 40\,\mathrm{W}$ the increase in the laser output power became linear and continued to increase linearly at higher absorbed pump powers. The TEM_{00} matching power was in the centre of the easily identifiable linearisation region. This is because it corresponded to the lowest M^2 factor which was close to 1 and implies that in this region the TEM_{00} mode had low diffraction losses and the beam had a minimal percentage of higher order modes. This is further supported by the 2D profiles which have the most intense and smallest Gaussian profile at 40.1 W. This result confirms the theory on matching presented in Sections 3.7.2 and 4.2.3.

As the diode pump power was increased after matching, the laser beam intensity elongated in the horizontal direction and the peak intensity decreased as the TEM_{10} mode started to oscillate. The fact that a pure rectangular mode was formed in the horizontal direction

indicated that the thermal lens was slightly stronger in that direction. This result was consistent with the quenching method which found that the beam became unstable in the horizontal direction first (Figures 6.1). The TEM_{00} mode radii decreased well below the matching value, (Figure 4.6) which allowed the output laser power to increase linearly with increasing higher order mode content.

By back-calculating the TEM_{00} beam of this resonator into the crystal a matching ratio between the laser and the pump mode sizes of $\sim 63\%$ was obtained. By using this and an ABCD model of the resonator it could be established that the focal length at 40.1 W was ~ 322 mm. Multiple new resonators could then be built to obtain the focal lengths at other matching powers and pump set-ups.

Finally, it is valuable to know whether a resonator is matched by evaluating only its output power since a CCD camera and beam profilers are not always available (especially at longer wavelengths like the mid and far infra-red). The matching pump power can be estimated by fitting linear functions on both sides of the linearisation region. Their intersection point is then taken as the matching pump power. The error that is made by doing this can easily be ascertained by deducting the resulting matching pump power from the one found by the more accurate CCD method (Figure 4.5). The discrepancy between the two methods is given in Figure 6.5 for all the TEM_{00} matching measurements that were performed for both polarisations of Nd:YVO_4 and the π-polarisation of Nd:$GdVO_4$. It can be observed that the values of the slope efficiency method are always weaker than those determined by the CCD camera. This discrepancy decreased to less than 1% for high pump powers, which is probably due to sharper linearisation.

6.3.2 Thermal lens results from the mode-matching method

Figure 6.6 shows the derived dioptric powers as a function of absorbed diode pump power for the two polarisations of Nd:YVO_4 and the π-polarisation of Nd:$GdVO_4$ measured at 1.064μm. We can observe that Nd:YVO_4 has weaker thermal lensing than Nd:$GdVO_4$ for the more useful π-polarisation. This is therefore another confirmation of the findings of Sato & Taira (2007) that the ratio of the dn_e/dT value and the thermal conductivity of Nd:YVO_4 is lower than that of Nd:$GdVO_4$ (Equation 5.6). This first direct comparison between the two materials therefore clearly shows that the cheaper and more widely available Nd:YVO_4 has better thermo-optical properties.

By comparing the thermal lens behaviour of two polarisations of Nd:YVO_4 it can be observed that the thermal dioptric powers of the weaker gain σ-polarisation were almost twice that of the π-polarisation. This large difference can cause the polarisation state of lasers with certain resonator configurations (containing crystals with unwedged pump faces) to flip at certain pump power levels. In such cases the σ-polarisation with the stronger thermal lens is stable at low pump powers while for higher pump powers the stronger gain π-polarisation becomes stable. These effects will also be reflected in the laser output powers which will undergo sudden changes unlike those described in the previous sections. Also, when constructing such lasers it is useful to keep an eye on the polarisation state of the laser, because any polarisation dependent attenuation optics will transmit rather than reflect when the polarisation flips. This will likely destroy any sensitive equipment behind them.

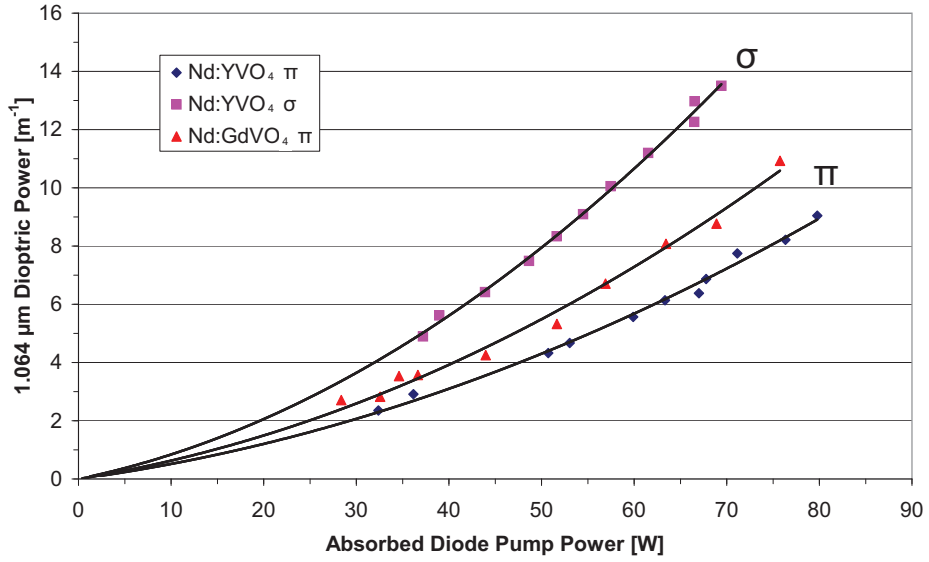

Figure 6.6: Thermal lens dioptric powers measured with the mode matching method for both polarisations of 0.15 % doped, single-side end-pumped Nd:YVO_4 and the $\pi-$polarisation of Nd:$GdVO_4$ crystals as functions of absorbed diode pump power.

A single measurement point using a fixed resonator was repeated for all the crystals in our possession to determine the variance in the results from using different crystals which can also come from different boules and even different parts of the same boule. The crystals where simply interchanged and the resonator realigned for each measurement. The resonator arm lengths therefore stayed roughly the same. It was subsequently determined that the measured dioptric power for a given crystal type varied by a maximum of $0.5\,\mathrm{m}^{-1}$. This was mainly due to differences in the doping of the different crystals.

It can be observed from the general behaviour and the fitted curves of all three plots in Figure 6.6 that the dioptric powers did not converge linearly towards the origin. However, the thermal lens must have increased from zero pump power since there is always heating during pumping due to the quantum defect (Section 2.5.4). This implies that the dioptric power must have increased non-linearly with respect to the absorbed diode pump power. Further proof of this non-linear increase is given in Figure 6.7 which illustrates single-side and double end-pumped dioptric power values for the π-polarisation of Nd:YVO_4.

The double end-pumped crystal can be approximated as two closely spaced thin lenses due to the high absorption of the pump power at ∼805 to 808 nm (Section 5.2.7). The combined dioptric power of the double-pumped system is then just the sum of the dioptric powers of each side according to the effective focal length equation $D_{\mathrm{eff}} = D_1 + D_2$ (Hecht, 1998 pp. 169). If the dioptric power increase was linear, the two measurement sets would overlap since the effective focal length equation is also linear. The fact that they do not, indicates that the thermal lens dioptric power increased non-linearly. A quadratic function $D_{\mathrm{single}} = A_1 P_{\mathrm{abs}}^2 + A_2 P_{\mathrm{abs}}$ was also fitted through the single end-pumped data points. The

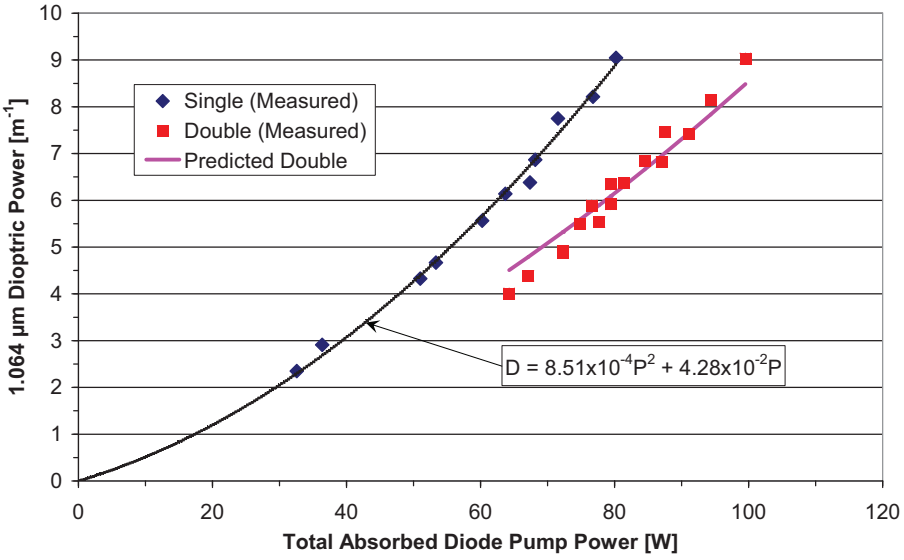

Figure 6.7: Single (blue diamonds) and double (red squares) pumped dioptric powers of Nd:YVO_4 as a function of the total absorbed diode pump power. The two measurement sets do not overlap which proves that the dioptric power increases non-linearly.

dioptric power from the double end-pumped system was then estimated with this function using the absorbed diode pump powers from each side (P_{left} and P_{right}). The estimated effective dioptric power of the double pumped set-up was therefore:

$$D_{\text{double}} = A_1 P_{\text{left}}^2 + A_2 P_{\text{left}} + A_1 P_{\text{right}}^2 + A_2 P_{\text{right}} \tag{6.1}$$

This relationship is shown as the solid pink line in Figure 6.7. This estimated line corresponded reasonably well with the measured values (in red), which further confirms the non linearity. This non-linear behaviour is contrary to most results reported in literature (Ozygus & Erhard, 1995; Lancaster & Dawes, 1998; Peng *et al.*, 2001; Kong *et al.*, 2004). Articles that do report it usually explain it by means of upconversion or some other non-linear heat source in the crystal (Eichenholz & Richardson, 1998; Amarande & Damzen, 2006). We show in Section 6.5.2 using probe beam experiments, that it is definitely not due to upconversion. We also identify or discount potential sources of this nonlinear behaviour by means of numerical FEA thermal calculations in Section 7.2.

6.3.3 The TEM_{00} M^2 factors

Each beam that was used in the mode-matching method had the best beam quality value (M^2) that was possible to obtain from the specific laser without physical apertures. Figure 6.8 illustrates these minimum M^2 factors of π and σ Nd:YVO_4 matched lasers as a function of absorbed diode pump power. The beam quality of both polarisations clearly deteriorated as the pump power was increased. This is mainly due to an increase in the spherical aberrations

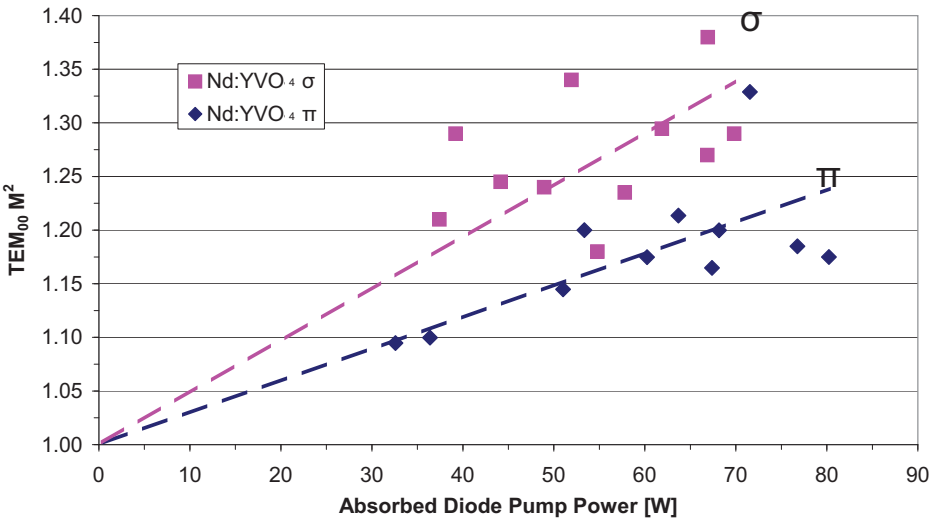

Figure 6.8: M^2 parameters of the π (blue diamonds) and σ (pink squares) TEM_{00} beams which were used to determine the dioptric powers of the thermal lenses in Nd:YVO_4 using the mode-matching method.

with pump power. The beam quality of the σ-polarisation also deteriorated faster than the π-polarisation despite the fact that its matching ratio was smaller.

6.3.4 The matching ratio

Figure 6.9 illustrates the matching ratios (w_{00}/w_p in Section 3.7.2) for the π and σ-polarisations of Nd:YVO_4 obtained from mode-matching measurements. The pumping arrangement for the two measurements was identical, only the curved back-reflector was aligned at a slightly different angle. The relatively low values of the matching ratios had significant repercussions for the efficiency since only part of the gain could be extracted in the TEM_{00} mode.

It can be observed that the matching ratio stayed constant with respect to the absorbed diode pump power for a specific polarisation. The matching ratio was therefore clearly not dependent on the absorbed diode pump power in the crystal. The probable reason for this is that the matching ratio depends on the relative losses between the fundamental and first higher order mode which does not change with pump power. The constant matching ratio further indicates that it does not depend on the absolute value of the spherical aberrations since these increase with pump power as was observed by the increase in the M^2 factor.

The measured matching ratios of the π-polarisation were also larger and had an average value of 0.635 compared to 0.563 for the σ-polarisation. The matching ratio therefore depends either on the dn/dT factor, or the gain, or both, since these were the only two parameters that were different in the two measurements.

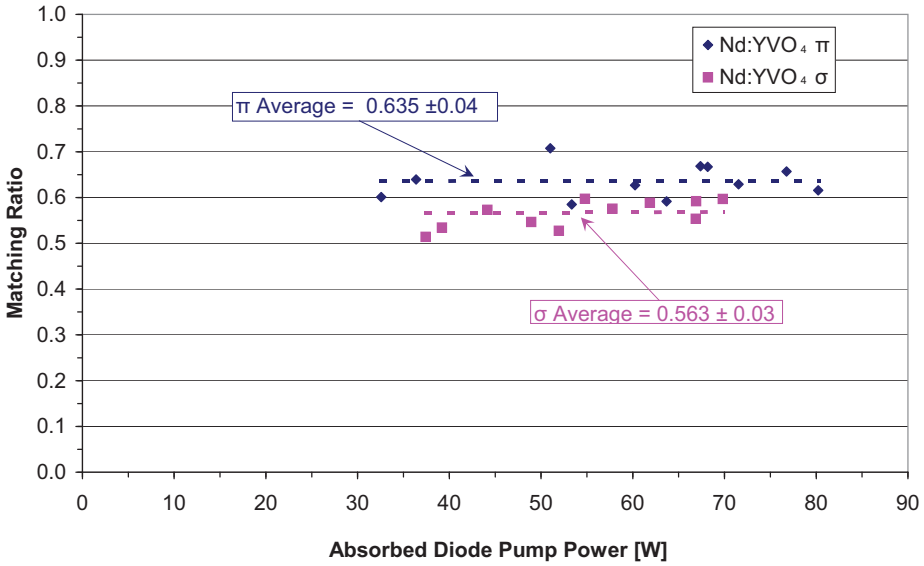

Figure 6.9: The matching ratio (w_{00}/w_{p}) for the π (blue diamonds) and σ (pink squares) polarisations of the Nd:YVO_4 crystals in our setup.

6.3.5 The TEM_{00} slope efficiencies

Figure 6.10 illustrates the laser output power as a function of absorbed diode pump power of all the TEM_{00} beams that were used to determine the dioptric powers of Nd:YVO_4 using the new mode-matching method. The plot of the output powers of resonators each optimised for optimum beam quality effectively formed a slope efficiency for the TEM_{00} beams. The slope efficiency at any given absorbed diode pump power could then be directly compared to the one taken from a short, flat-flat multimode resonator that extracted all the available gain from the crystal (Section 3.9).

It can be observed in Figure 6.10 that the output powers and slope efficiencies of the π-polarisation was clearly higher and had a lower threshold than that of the σ-polarisation. This was due to the higher gain of the of π-polarisation (Section 2.5.2). By fitting a quadratic function through the π-TEM_{00} output power values it can be seen that its effective slope efficiency decreased from roughly 42% to roughly 21.5% at the maximum pump power. From Equation 5.4 we can deduce that the losses (L_{ls}) for the TEM_{00} mode increased with pump power since the other parameters remained constant. This is therefore further confirmation that the spherical aberrations increase with the pump power as was already determined from the increasing M^2 results. However, this effect is a far more severe consequence of the spherical aberrations than the slight increase in M^2 of Figure 6.8. It also severely affected the efficiency of the system which was already decreased by the matching ratio. It is therefore crucial to find ways to minimise the spherical aberrations in order to build efficient, good beam quality lasers with materials exhibiting strong thermal lensing.

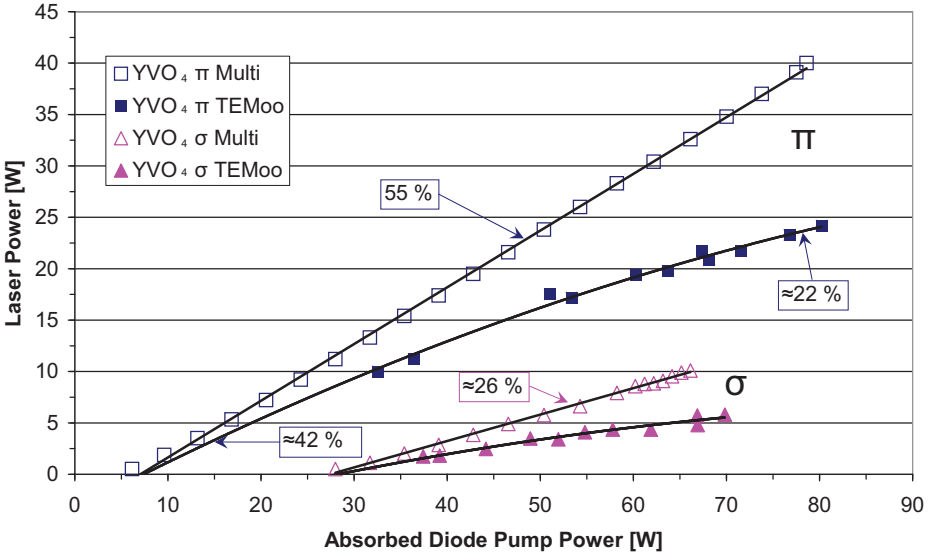

Figure 6.10: The output powers of short flat-flat resonators extracting all the gain from a resonator (open symbols), increase linearly. The effective slope efficiencies for the TEM_{00} beams (filled in symbols) shows a decreasing rate for an increase in pump power. Only results for the π (blue squares) and σ (pink triangles) polarisations of Nd:YVO_4 are shown.

6.4 Comparison between the quenching and mode-matching methods

A direct comparison of the results of the two resonator methods could be made by plotting the two sets of measured dioptric powers for Nd:YVO_4's π-polarisation observed in Figures 6.3 and 6.6 on the same graph in Figure 6.11. It can be observed that the dioptric powers agreed remarkably well with each other. This proves our earlier assumption that using the inflection point in the quenching method measures the defocus of the central unaberrated part of the thermal lens. The much easier and quicker quenching technique can therefore in future be used to measure dioptric powers for building high-power lasers by using the deflection point. However, the mode-matching technique is still more reproducible and also provides us with the matching ratio, effective TEM_{00} slope efficiencies, TEM_{00} M^2 values and therefore good quality lasers that could potentially be used for other applications.

6.5 Results of the probe beam method

We used the probe beam method described in Sections 4.3.1 and 5.4.2 to measure changes to the thermal lens dioptric power at 632.8 nm.

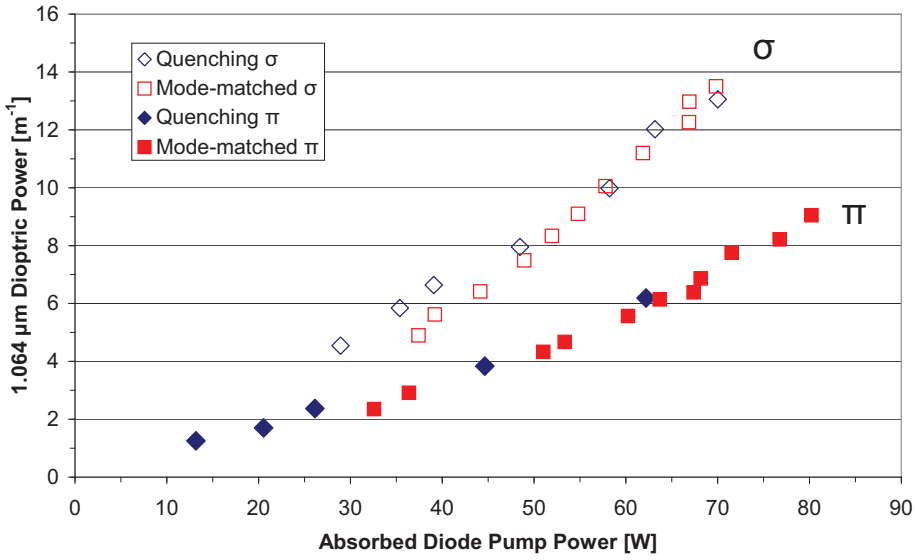

Figure 6.11: Comparison of the quenching (blue diamonds) and mode-matching (red squares) methods using dioptric powers of the thermal lenses of the π (closed symbols) and σ (open symbols) polarisations of Nd:YVO_4.

6.5.1 Evaluation of the probe beam method

Comparative measurements of the relative thermal lensing between Nd:YVO_4 and Nd:$GdVO_4$, their two polarisations and especially the lasing and non-lasing conditions (Section 4.3.1) could be performed with the probe beam technique. The astigmatism of the thermal lens could also be determined from the second moment beam radii in both transverse directions.

The size of the probe beam was chosen to be equal to that of the pump beam in the crystal. A significant part of the aberrated part of the thermal lens was therefore measured as well so that the far field profile of the transmitted probe beam consisted of several concentric rings (Section 3.8). The second moment radii of these ring profiles were used to back calculate the focal length of the thermal lens at 632.8 nm. In retrospect it would have been better to decrease the size of the probe beam until no rings were observed.

Figure 6.12 illustrates a typical series of the probe ring profiles that were recorded with a CCD camera placed 307 mm behind a Nd:$GdVO_4$ crystal under lasing conditions. The extraordinary (e) beam on the left measures the π-thermal lens and ordinary (o) beam on the right the σ-thermal lens (Table 2.2).

The o-probe-beam was focused at roughly 28 W and the e-probe beam at roughly 35 W of absorbed pump power at the camera measurement point. The o-beam also diverged more and had more rings than the e-beam at a specific pump power. This is a striking visual confirmation that the σ-polarisation had a much stronger thermal lens than the π-polarisation (Sections 2.3.4, 6.2 and 6.3).

The ring structure only emerged at high pump powers and only in the far field after the beams were focused. This corresponded very well with the theory presented in Born & Wolf

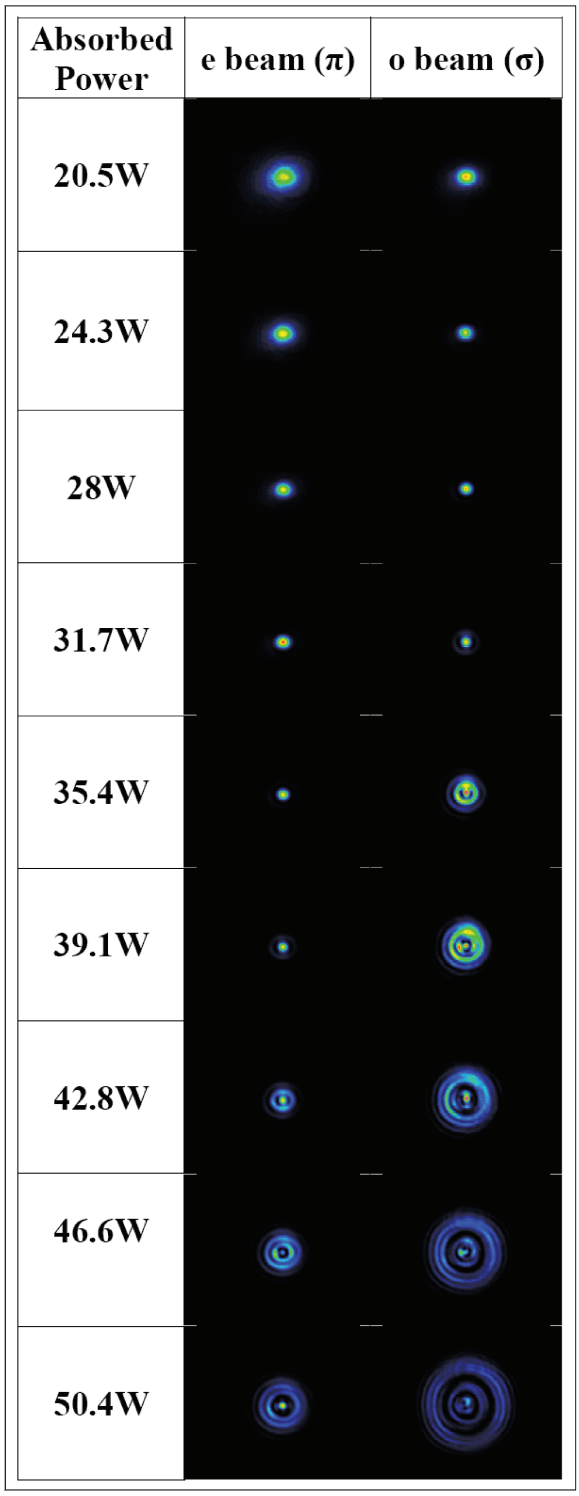

Figure 6.12: 2D camera profiles of the extraordinary (π) and ordinary (σ) components of a HeNe probe beam placed 307 mm behind a Nd:$GdVO_4$ crystal pumped over a range of diode pump powers.

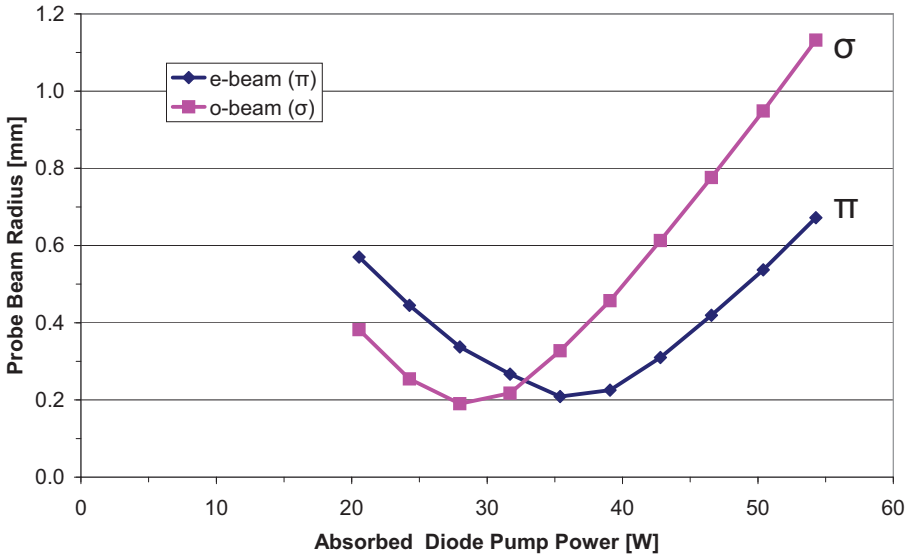

Figure 6.13: Average beam radii of the 2D plots of Figure 6.12. The e-beam (π-polarisation) is shown in blue diamonds and the o-beam (σ-polarisation) in pink squares.

(1986) presented in Section 3.8. The beams were also roughly symmetrical in the horizontal and vertical directions. We therefore opted to ignore the slight astigmatism at first and to use only the averaged second moment beam radii in the two transverse directions to back calculate the focal lengths of the thermal lenses (Section 4.3.1). Figure 6.13 plots the second moment beam radii of the ring profiles shown in Figure 6.12 as a function of the absorbed diode pump power. Only values significantly larger than the focus could be used because a slope in the beam radius values was needed to accurately link a beam size with a focal length. The comparative thermal lens results are presented in the next few sections.

6.5.2 Thermal lens results from the probe beam method

Material comparative measurements

Figure 6.14 illustrates the 632 nm dioptric powers of both polarisations of Nd:YVO_4 and Nd:$GdVO_4$ as a function of relatively high absorbed diode pump powers. It can be observed that Nd:YVO_4 had somewhat weaker thermal lensing for both polarisations. The σ-polarisations of both materials also had substantially stronger thermal lensing at 632 nm than their respective π-polarisations. This was to be expected because the dn_o/dT value were higher for both materials (Table 2.4). The measured thermal lensing at 632 nm was stronger than at 1.064 μm due to higher dn/dT values at the probe wavelength. The measurement value sets of the experiments at 1.064 μm and 632 nm could also not be compared with each other because they overlapped with different parts of the thermal lens (their respective Zernike radii were different).

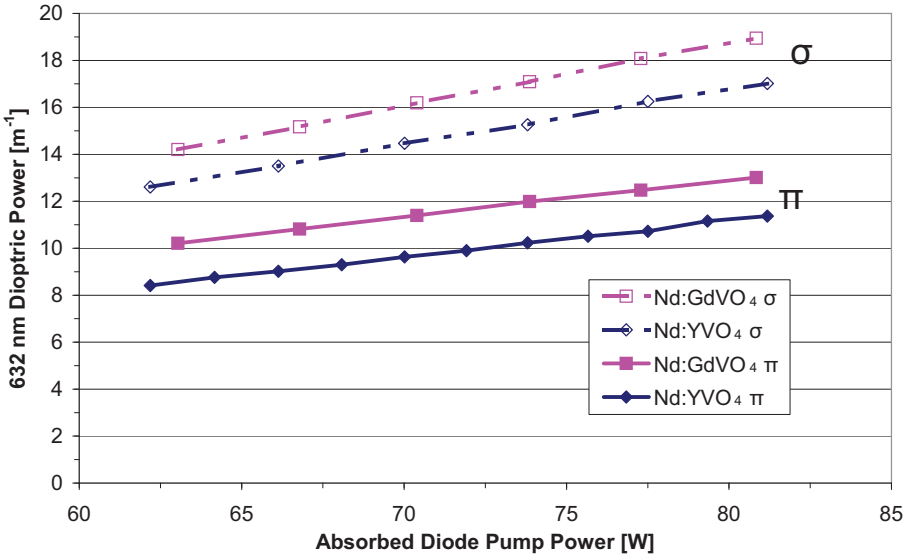

Figure 6.14: Dioptric powers measured with the probe beam method at 632 nm for the π (solid lines) and σ (broken lines) polarisations of Nd:YVO_4 (blue diamonds) and Nd:$GdVO_4$ (pink squares).

Lasing/non-lasing comparative measurements

The probe beam method is very accurate in determining the difference in thermal lensing (and therefore the heat load) between lasing and non-lasing conditions because the diagnostic and pump set-up is not varied between measurements. Only the temperature profile changed before and after insertion of a beam-block in the resonator between mirrors M_3 and M_6. Figure 6.15 illustrates the 632 nm dioptric powers under lasing (blue diamonds) and non-lasing (pink squares) conditions for the π-polarisations of both vanadate materials measured at relatively high diode pump powers. It can be observed that there was almost no difference in the thermal lensing, which translates into a negligible difference in the temperature profile inside the crystal. This was unusual for vanadate crystals since upconversion, which increases the heat load during non-lasing conditions, is usually strong in them (Section 2.5.5). The absence of upconversion was probably due to the very low doping concentration of the crystals (0.15%), since upconversion is strongly dependent on the intermolecular distances between the dopant ions (Chen *et al.*, 2000). This had the consequence that there was no danger of damage to the crystal if lasing was interrupted when the laser was operated close to the fracture limit of the crystal.

The fact that the thermal lensing did not become weaker when lasing was interrupted also indicated that there was no excited state absorption of the laser radiation in either of the materials (Section 2.5.6). This result is expected for the 1.064 μm experiments. However, significant excited state absorption is expected if the laser is operated at 1.34 μm (Chen *et al.*, 1999). Explorative experiments were therefore performed at 1.34 μm by exchanging the curved back-reflector and output coupler of Figure 4.4 with 1.3 μm coated optics. After the laser started oscillating at 1.34 μm, the pump power could be decreased to a much lower

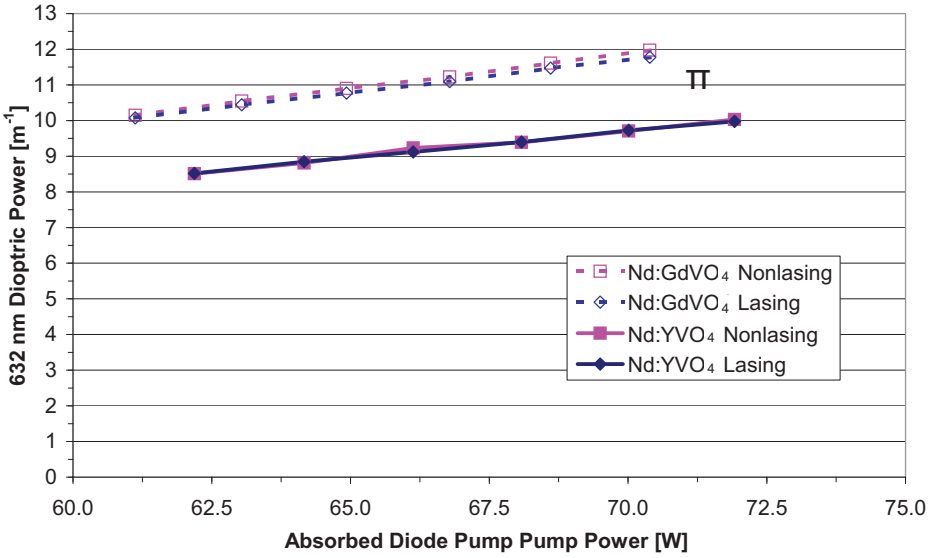

Figure 6.15: Dioptric powers at 632 nm of the π-polarisations of Nd:YVO_4 and Nd:$GdVO_4$ under lasing (blue diamonds) and non-lasing (pink squares) conditions.

value than the initial threshold value before the laser stopped oscillating again. The stronger thermal lens during lasing kept the laser stable at these lower powers due to the extra heat load from excited state absorption. This hysteresis in the threshold was therefore a partial confirmation of the results of Chen *et al.* (1999) who measured a stronger thermal lens at 1.34 μm during lasing conditions. Further study is however needed because 1.3 μm stimulated emission forces more ions to the $^4I_{13/2}$ level during lasing. This substantially increases the quantum defect which could therefore also be responsible for the increase in temperature.

Astigmatism of the thermal lens

The astigmatism could be estimated by back-calculating the thermal lens dioptric powers from the beam radii in the horizontal and vertical directions. Figure 6.16 illustrates these dioptric powers for the π-polarisations of Nd:YVO_4 and Nd:$GdVO_4$. The horizontal a-direction (Section 5.1) clearly had a slightly stronger thermal lens in both materials which can be explained by the lower thermal conductivity of both materials in this direction (Section 2.3.3). The temperature profiles were therefore different in the two crystallographic directions. This result corresponded with the quenching measurements of Section 6.2 where the central part of the thermal lens became unstable in the horizontal direction first. It also corresponded with the mode-matching method in which the first higher order mode first emerged in the horizontal direction (Section 6.3.1).

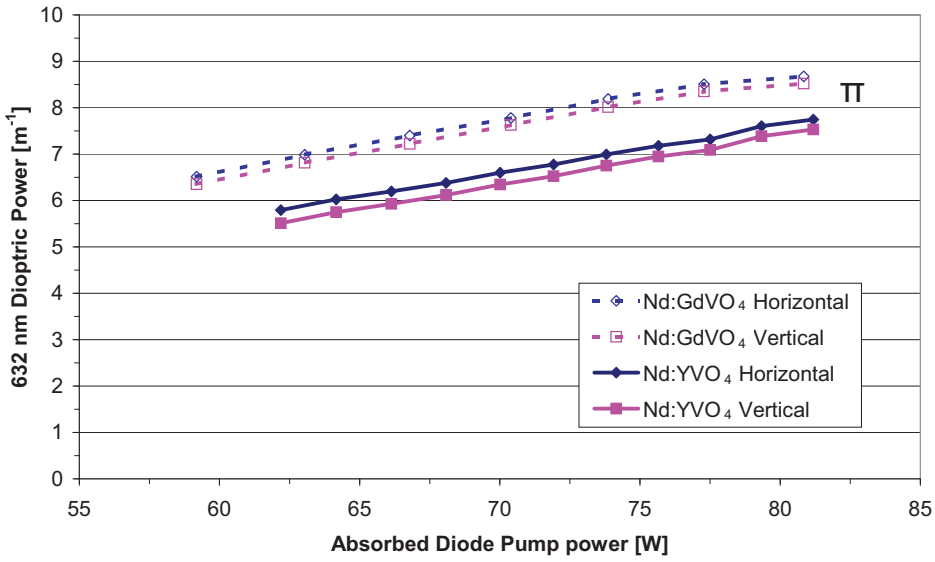

Figure 6.16: Dioptric powers in the horizontal (blue diamonds) and vertical (pink squares) directions of the π-polarisations of Nd:YVO_4 (solid lines) and Nd:$GdVO_4$ (broken lines).

6.6 Double end-pumped laser experiments

Finally, double end-pumped laser experiments were performed to investigate the maximum power that could be extracted from a single crystal in multimode or TEM_{00} operation. Figure 6.17 illustrates both the multimode and matched TEM_{00} output powers as a function of absorbed diode pump powers of lasers built with an 18 mm long 0.15% doped Nd:YVO_4 crystal.

The multimode values were obtained from a single short flat-flat resonator (Section 4.2.1) with a 70% reflectivity output coupler. The high optical to optical slope efficiency of 58% indicated that the multimode beam extracted all the inversion and that the output-coupler was chosen close to the optimum reflectivity according to Equation 5.4. We could therefore build highly efficient multimode 1.064 μm lasers by using these vanadate crystals. It was possible to increase the maximum multimode output power from 66.5 W for a double pumped crystal to over 80 W by using a double crystal, quadruple pumped setup. At that stage the high intra-cavity power fractured one of the crystals due to pre-existing damage on one of the pump-faces.

Also shown in Figure 6.17 are the output powers of TEM_{00} mode-matched beams from a couple of concave-flat matching resonators which contained a double pumped crystal. Two distinctive groups of output powers which originated from the same resonators can be observed. Two TEM_{00} output values were obtained from a single resonator because the effective thermal lens was strong enough for matching to occur twice. The first group of values at lower pump powers was from the normal alignment **insensitive** side of Zone 2 that was previously used in the mode-matching method (Section 4.2.3 and Figure 4.6). The other values at higher pump powers were on the alignment **sensitive** side of Zone 2 just before the laser be-

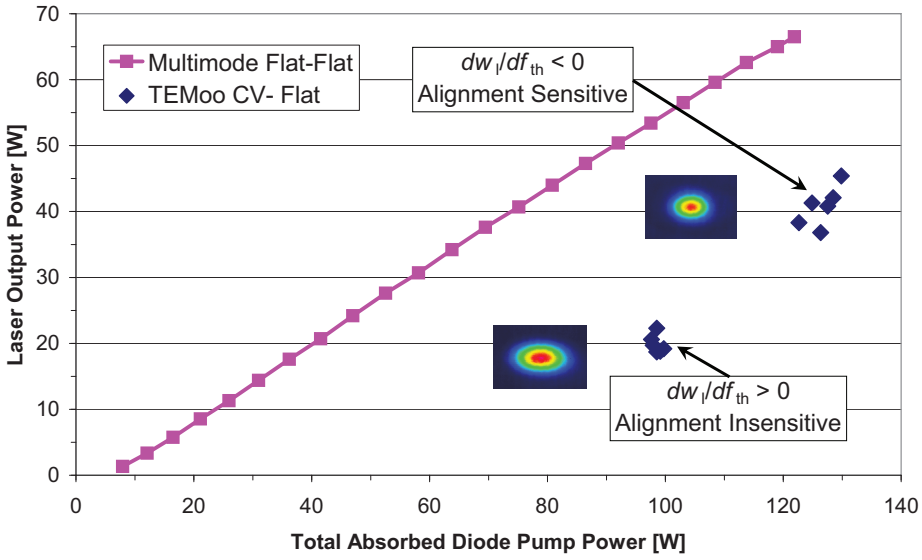

Figure 6.17: Multimode and TEM_{00} output powers of a double end-pumped laser.

came unstable again (Figure 3.6). The output power of the second group therefore fluctuated widely. However, they seemed to have better beam quality than the alignment insensitive ones as could be observed from their smaller 2D CCD profiles. The second group also had a better extraction efficiency as could be seen from their higher power percentage with respect to the multimode output which now acts as a reference. This interesting result confirms a theory postulated by Clarkson (2001) that more efficient lasers can be built if dw_l/df_{th} is negative. He views the thermal phase change as a lens with a radially varying focal length. This intuitive approach stems from the traditional view of negative spherical aberration in which light rays further from the optical axis are focussed further away than those closer to optical axis (Figure 3.3). Negative spherical aberration therefore weakens the strength of the thermal lens in its outer parts due to the r^4 dependence. This implies that the beam radii of the higher order modes (which are larger than the TEM_{00} mode with fixed relationships) are reduced by the thermal lens if $dw_l/df_{th} < 0$. Their sizes are therefore closer to that of the TEM_{00} mode than if there would be no spherical aberrations and this leaves them with less gain because of the higher overlap with the TEM_{00} mode. This shifts the power at which higher order modes start to oscillate to higher pump powers which implies that the matched resonator is more efficient.

In Figure 4.6 it can be observed that in all the resonators that were used in the mode-matching method, dw_l/df_{th} was positive. The Figure also shows that dw_l/df_{th} was negative for the second matching points which could only be reached with the stronger effective thermal lens in double-pumped crystals. The higher efficiency of the second matching points therefore confirms the theory of Clarkson (2001). The low power extraction of both zones was also due to the poor matching ratio and the large thermal spherical aberrations caused by the two thermal lenses on either side of the crystal. It could also be that the two pump beams did not

overlap perfectly, which would have further decreased the effective matching ratio because the aberrated regions would have overlapped with the un-aberrated ones. It is therefore vital that new pump shaping techniques be developed to decrease the thermal spherical aberrations and increase the matching ratio.

6.7 Conclusion

This chapter mainly evaluated the results from thermal lens measurements by means of three different methods that were described in Chapter 4. We showed for the first time that by using the inflection point in the slope efficiency of a flat-flat resonator, one can obtain reasonably accurate values of the unaberrated part of the thermal lens focal length. Our own novel mode-matching method reproducibly measured the central unaberrated thermal focal lengths and also provided a wealth of information on how the aberrations affect good quality laser beams. Probe beam measurements showed for the first time that there was little thermal difference between lasing and non-lasing conditions in our crystals. This indicated that there was no upconversion present because of our chosen optimal low doping. In the next chapter we evaluate the thermal lens results by means of finite element analysis.

Chapter 7

Numerical investigation of Nd:YVO_4's material properties and thermal lensing behaviour

7.1 Introduction

In the previous chapter we demonstrated that Nd:YVO_4 has superior thermo-optical properties. In this chapter we show how we used numerical FEA calculations to establish which of the different dn_e/dT values of Nd:YVO_4 in the literature (Table 2.4) fit our experimental results the best. By varying different input parameters we could also identify or discard potential sources of the nonlinear increase in the dioptric power (Figure 6.7). Finally, we calculated the stresses inside the crystal to evaluate how to further power scale lasers built with these materials.

7.2 Finite Element Analysis using LASCAD

Numerical finite element analysis (FEA) calculations were performed to model various aspects of our thermal lens measurement results and to investigate the aberrations and thermal stresses in the crystals. Many FEA packages are available on the market. The commercial program LASCAD (LASCAD, 2008) was specifically developed for laser modelling applications and greatly simplifies thermal calculations for laser crystals. The program contains most crystal geometries, side or end-pumped configurations and end-pumped profiles.

LASCAD divides the crystal into small three dimensional elements which together form a mesh. For a square crystal the mesh elements are cubic with dimensions Δx and Δy in the transverse directions and Δz in the propagation direction. Δz is usually longer because the heat flow is mainly transverse towards the edges (Section 3.3).

The 3D temperature distribution is iteratively obtained for each mesh element by solving the steady state heat equation (Equation 3.1). The thermal expansion, stress and refractive index profiles can then be calculated from this 3D temperature distribution.

LASCAD provides libraries of the material and laser properties of a few common laser materials and gives the user control over the FEA mesh size and convergence limits. However, it proved quite a challenge to obtain accurate material parameters to use in the calculations since many of the parameters in LASCAD's material data files were incorrect. This was not the fault of the programmer, but rather a consequence of the debate in the literature about the values of dn/dT and thermal conductivity (Section 2.4) and to which we will contribute. The next sections review the settings and the final choice of material parameters that were used in the calculations in roughly the same sequence as they were entered into the program.

7.2.1 Symmetry and crystal geometry

All the crystals in this study were uni-axial and were cut so that their c-axes were perpendicular to the propagation axis. This implied that the square crystals had different properties in the horizontal and vertical directions (Section 2.3.1). It was therefore logical to use rectangular symmetry in our calculations.

A slab geometry with widths of 4×4 mm and a length of 18 mm was selected in LASCAD. Wedged geometries could also be selected but the temperature outputs were difficult to process due to a slight symmetry error in the program. It was therefore decided to model the square wedged crystals with an unwedged geometry. The error incurred because of this was deemed small because the wedge was only $2\,^\circ$ and had a much larger influence on the optical propagation than the thermal distribution.

7.2.2 Pump settings

Choosing a pump profile was more complicated since the real pump profile changed during propagation (Figure 5.7). Only one unvarying end-pumped profile could be chosen by changing a super-Gaussian coefficient. The pump profile could be continuously varied between Gaussian and flat-top, meaning that its kurtosis parameter (Equation 5.8) could also be varied from 1 to 0.6. In Section 7.3.1 a temperature profile calculated with a kurtosis parameter value of 0.6 (a flat-top pump beam) was used to compare the numerical calculations to the analytical model given by Equation 3.23. In order to simulate our experimental set-up we weighed the kurtosis parameters of the pump profiles of Figure 5.7 with the percentage of the total power that was not yet absorbed at their positions. This weighted kurtosis parameter was calculated to be 0.78, which corresponded to a beam with a super-Gaussian coefficient of 3.28. The other final input pump parameters were a pump focus radius of 0.71, at a position 2 mm from the pump-face into the crystal and a divergence of 48 mrad (Section 5.2.2). The incident pump powers in the calculations were changed in seven steps between the values of 16 to 100 W to simulate the thermal and thermo-optical behaviour of the vanadate crystals.

7.2.3 Boundary conditions

The same boundary conditions applied as those of Section 3.3. We achieved very good cooling of all our crystals by mounting them with heat conduction epoxy to four copper pre-mount blocks (Section 5.1.2). All four constant edge temperatures of the FEA model were therefore set to the temperature of the cooling water in the heat-sinks which was cooled at 293 K

(25 °C). It was thus assumed that there was only a very small temperature gradient between the crystals and their heat-sinks.

7.2.4 The thermo-optical coefficients

Section 2.4 revealed that there is still considerable contention over the dn/dT values of the two vanadates. The LASCAD simulations afforded us the opportunity to test each of the dn_e/dT values from the different research groups that are listed in Table 2.4 by comparing the thermal dioptric powers that were calculated with each of their values to our measured results. We show in Section 7.4.1 that Sato & Taira (2007)'s value matches our experimental results the best. Their value was then used in further calculations to identify or discard the sources of the nonlinear increase in dioptric power.

7.2.5 The thermal conductivity

Sato & Taira (2006) also demonstrated that the thermal conductivities of both the vanadates and YAG are significantly reduced when the temperature is increased (Section 2.3.3). This decrease in thermal conductivity leads to an even higher peak temperature increase in the crystals. LASCAD is able to incorporate temperature variable material parameters. We could therefore test what effect the temperature dependent thermal conductivity had on the thermal lens. We did this by performing two sets of calculations. In one we kept the thermal conductivities constant at the 300 K values and in the other we inserted temperature dependent equations that we fitted to their data and listed in Table 2.1. The equations had to be sent to the LASCAD programmer in order to incorporate it into the material data input files. We could therefore directly compare the two thermal lenses and from that judge the influence of the temperature dependence of the thermal conductivities on the thermal lensing.

7.2.6 Diode absorption coefficients in the *a* and *c*-directions

The outputs of fibre-coupled diode lasers are usually not polarised and in order to polarise them one has to discard half of the available pump power. The two vanadates had different absorption coefficients in the two crystallographic directions and this had to be incorporated in the calculations. In both vanadates the component of the pump light that was parallel to the c-direction (π-polarised light) had a much stronger absorption (Figure 2.5) than the component that was parallel to the a-direction (σ-polarised light). The π-half of the pump light was therefore absorbed in a short distance at the front-end of the crystal and the σ-half was more spread out. This led to a complex heat load inside the crystal, which consisted of both a highly concentrated component near the pump-face and a dispersed component over the length of the crystal. To model such a heat load we had to specify the diode absorption coefficients in the two crystallographic directions ($\alpha_{\mathrm{diode}-a,c}(\lambda)$) at a specific incident pump power. These were determined from the convolutions of the broad 140 W diode spectrum ($I_{\mathrm{dio}}(\lambda)$) and the absorption spectra of the two polarisations of the two vanadates ($\alpha_{\mathrm{abs}-a,c}(\lambda)$ in Figure 2.5). Such convolutions were performed numerically in MATLAB (MATLAB, 2008) by using the integral equation

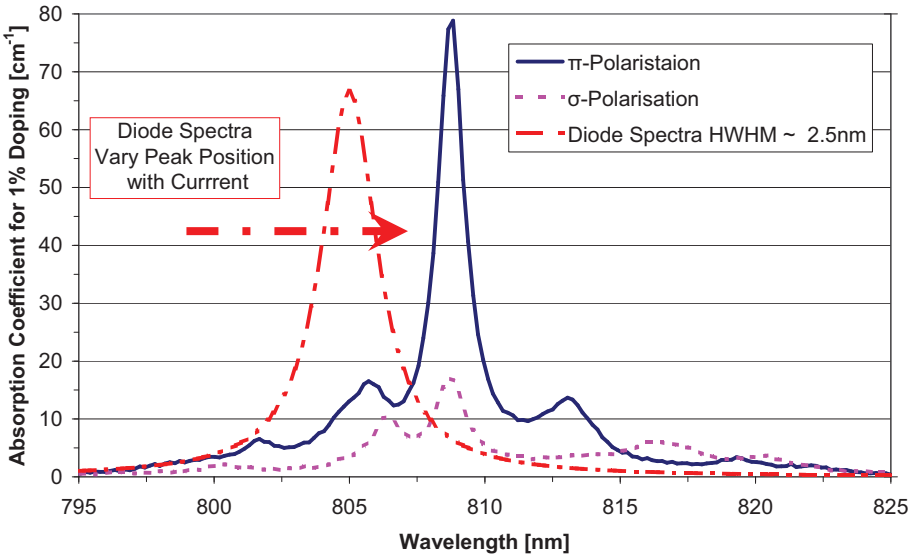

Figure 7.1: The absorption spectra of 1% doped Nd:YVO_4 and the output spectrum of the 140 W diode laser with its central intensity peak at 805 nm. The convolution of these two spectra gives the absorption spectrum of the diode laser at 805 nm.

$$\alpha_{\text{diode}-a,c}(\lambda) = \frac{\int_{\lambda_{\text{low}}}^{\lambda_{\text{high}}} I_{\text{dio}}(\lambda)\alpha_{\text{abs}-a,c}(\lambda)d\lambda}{\int_{\lambda_{\text{low}}}^{\lambda_{\text{high}}} I_{\text{dio}}(\lambda)d\lambda}. \tag{7.1}$$

$I_{\text{dio}}(\lambda)$ is the spectral profile of the diode at a specific central peak wavelength and λ_{low} and λ_{high} are the wavelength integration limits where the diode output power is essentially zero. The absorption spectra of the two materials were obtained from Cross (2004) and the diode spectrum was approximated with a Lorentz function with a half-width of approximately 2.5 nm. Figure 7.1 illustrates the convolution process by plotting both the 140 W diode output spectrum at 805 nm and the absorption spectra of both polarisations of Nd:YVO_4 on the same graph.

The central output wavelength of the 140 W diode laser also increased with the current through it and therefore effectively with its output power. No attempt was made to keep the wavelength constant by changing the cooling temperature (Section 5.2.1). This was because it would have required operation of the diode at unsafe temperatures that were either too low, which would have led to condensation inside the diode, or too high, which would have led to thermal damage of the diode. We rather opted to optimise the wavelength for maximum absorption at the maximum diode power. Obtaining the 140 W diode's absorption spectra in the two materials required a near continuous calculated series of convolutions of the absorption spectra with diode spectral profiles whose centre wavelengths varied between the values the diode had at threshold and at maximum output. The $\alpha_{\text{diode}-a,c}(\lambda)$ values obtained were

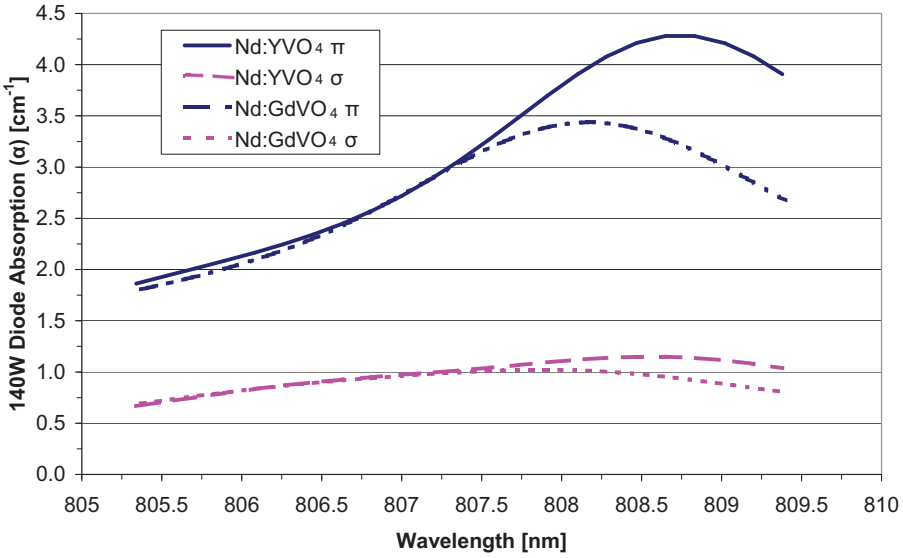

Figure 7.2: The absorption spectra of the 140 W diode laser of both polarisations of both vanadates.

then plotted as functions of the central diode wavelengths that were used to calculate them. The resulting diode absorption spectra of the two polarisations of both materials are shown in Figure 7.2. The spectra still need to be multiplied with the doping percentage of the crystals which was ∼0.15%. The diode absorption spectra coefficients were then correlated with the diode output power to obtain the the absorption coefficients that could be used in the LASCAD calculations for specific incident pump powers. A graph of these values is given in Appendix A.

7.2.7 Summary of the material input parameters

Several of the other material parameters were changed when a reliable source was found with a more recent value than what was available in the LASCAD material data files. All the material parameters that we used are summarised in Table 2.1. LASCAD's input units are somewhat different from the standard ones were used in this thesis. The material input parameters of the two vanadates are therefore given in Appendix A in the same layout and in the correct units that LASCAD required. Also, we used parameters of the π-polarisation of Nd:YVO_4 to calculate general temperature and phase change profiles for general illustrative purposes throughout this thesis.

7.3 Temperature, displacement and phase change profiles

In this section we illustrate how we calculated the temperature and thermal phase change profiles which we used to evaluate the thermal lensing and to calculate the thermal lens focal lengths, spherical aberrations and stresses.

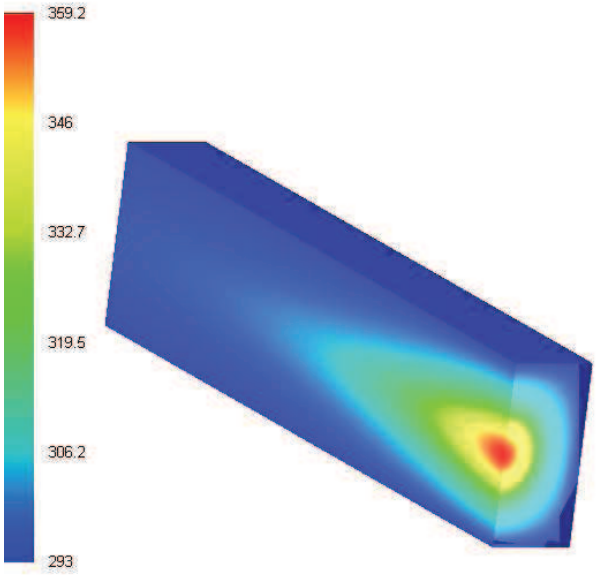

Figure 7.3: A 3D visualisation of the temperature distribution (in K) in a typical vanadate crystal. The crystal is vertically cut through the centre so that the temperature distribution in the propagation direction can be seen.

7.3.1 Temperature profiles

Figure 7.3 illustrates a 3D visualisation of a typical temperature distribution in one of the vanadate crystals and was generated with LASCAD using the pump distribution described in Section 7.2.2 . The visualisation of the crystal is vertically cut through the centre which allows observation of the temperature distribution in the propagation direction. The temperature was highest in the centre of the pump-face and dropped off towards the edges as was expected from Chapter 3. It also decreased in the propagation direction as the pump was absorbed.

We subsequently attempted to verify that the numerical results agreed with the theory of Chapter 3. We did so by calculating a numerical temperature profile for a 4×4 mm square cut crystal pumped by a flat-top beam of radius 0.71 mm. This temperature profile is plotted in pink dots in Figure 7.4. We also used Equation 3.23 as a fitting function to the data by varying only the constant $A_{\mathrm{ft}}(z)$ even though it was solved for radially symmetric crystals. A crystal radius R_{cr} of 2 mm and the same pump radius of 0.71 were used in the fitting function.

Figure 7.4 shows that Equation 3.23 fitted the numerically calculated data very well, if an appropriate value of $A_{\mathrm{ft}}(0)$ was chosen. This was further supported by a fourth order fit through the numerically calculated data which showed that the spherical aberration was almost non existent inside the pump-region which correspond very well with the quadratic part of Equation 3.23.

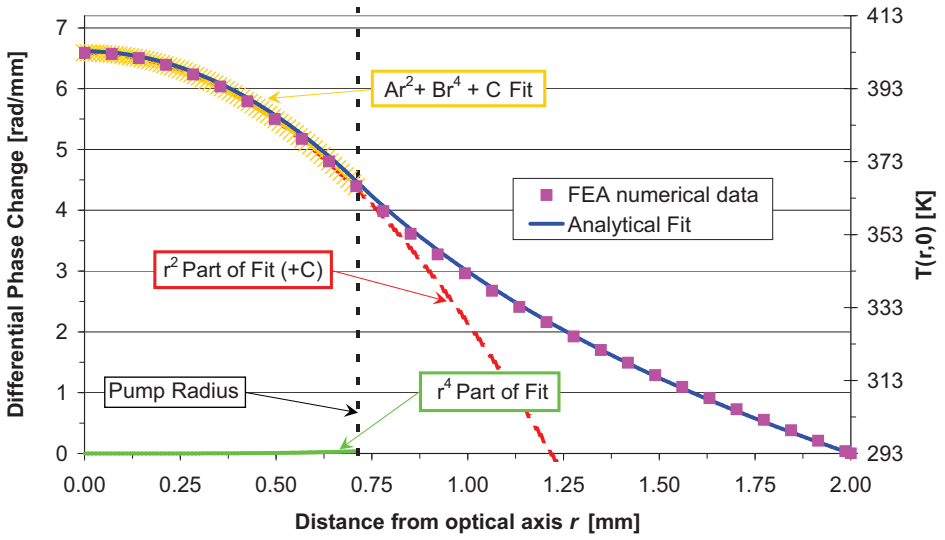

Figure 7.4: A numerically calculated pump face temperature (or differential phase change) profile for a 4×4 mm square-cut vanadate crystal pumped by a perfect, non-evolving flat-top beam of radius 0.71 mm (red squares) and an analytical fit using analytical Equation 3.23 (solid blue). A Seidel polynomial containing both second and fourth order terms is also fitted to the numerically calculated data.

7.3.2 Refractive index phase change profiles

The 3D refractive index and differential phase change profiles was calculated from the 3D temperature profile by using Equations 3.4 and 3.6. Figure 7.5 illustrates such a three-dimensional refractive index differential phase change profile. It can be observed that the phase of a beam that propagates through the crystal will only be significantly changed within the first third of the crystal (ignoring the constant phase lag due to the crystals refractive index). The total phase change contribution from the refractive index variation is obtained by integrating the 3D phase change distribution along the propagation direction according to Equation 3.7. Figure 7.6 illustrates the refractive index phase change profile obtained by integrating the differential phase change profile of Figure 7.5. Seidel functions fitted to the data indicates that there is significant spherical aberration inside the pump-region due to the refractive index profile.

7.3.3 End face bulging phase change profiles

LASCAD also provides the displacement of the pump-face. The sag profile could therefore be determined by means of Equation 3.8 from which the phase change profile of the end-face bulging contribution could be calculated using Equation 3.9. Figure 7.7 illustrates the displacement and phase change profiles of the crystal with the temperature distribution observed in Figure 7.3. The second order part of the Seidel fit indicates that the end-face bulging

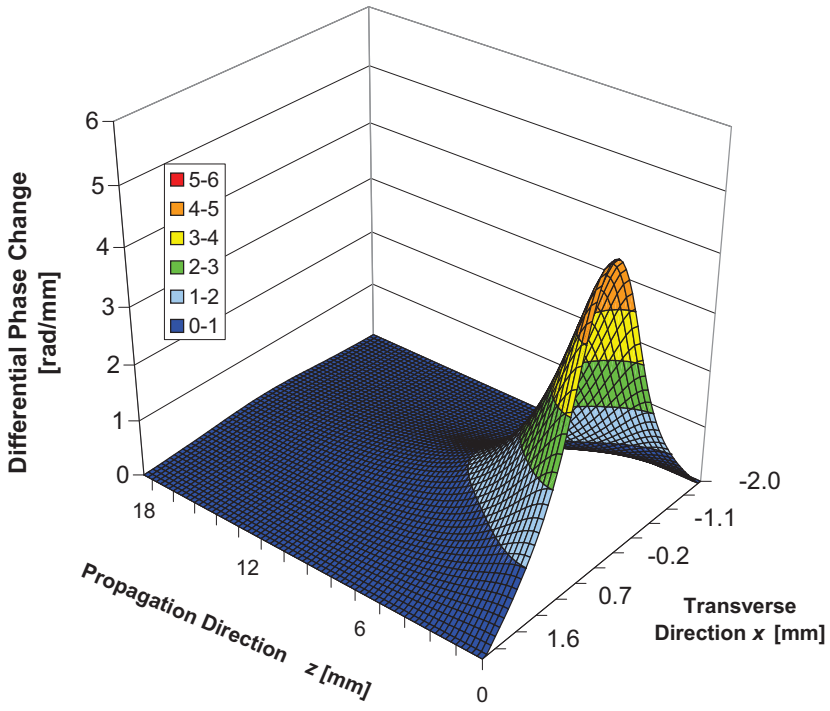

Figure 7.5: The 3D differential phase change profile of a vanadate crystal with the temperature distribution shown in Figure 7.3.

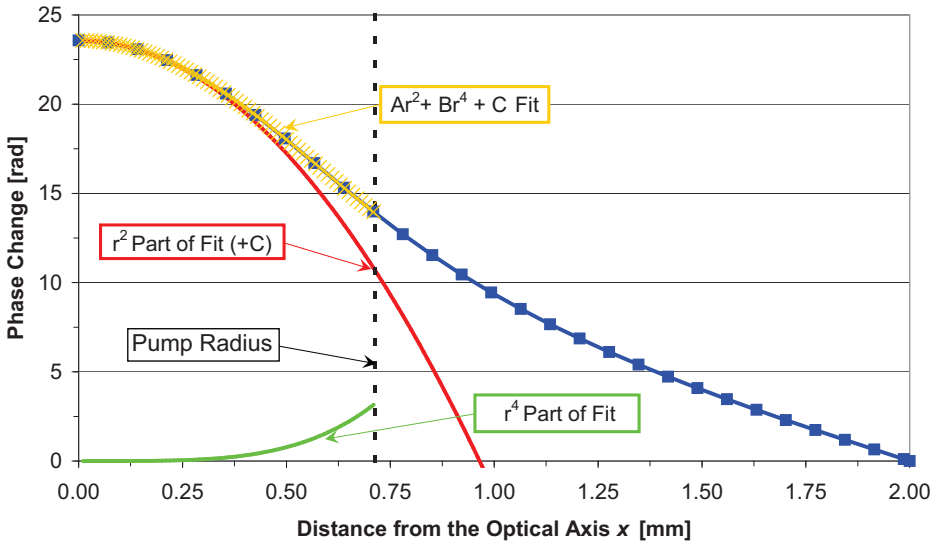

Figure 7.6: The refractive index phase change profile (blue squares) determined by integrating the 3D differential phase change distribution of Figure 7.5 in the propagation direction. The Seidel fit profiles are also shown and indicate that there is significant spherical aberration inside the pump-region.

caused a weak lens. The fourth order part of the Seidel fit confirms that the end-face bulging causes substantial spherical aberrations inside the pump-region.

7.3.4 Total phase change profiles and thermal lensing

The total phase change profile for a specific pump power was obtained by adding the integrated refractive index and end-face bulging phase profiles together according to Equation 3.12. The thermal lensing behaviour was then evaluated by expanding the phase profile with the Zernike polynomials (Section 3.4.4). The Zernike radius that was chosen depended on the experimental data that was modelled. For the data from the mode matching experiments the matching ratio times the pump radius was chosen as the Zernike radius (Section 6.3.4). The Zernike radius therefore corresponded to the average radius of all the TEM_{00} beams that we used to measure the thermal lens. This was 0.635×0.71 for the π-polarisation of Nd:YVO_4 and 0.563×0.71 for its σ-polarisation. The thermal lens focal length was then calculated using the A_2^0 Zernike coefficient in Equation 3.21 and the amount of spherical aberration was ascertained by the A_4^0 Zernike coefficient.

The phase profiles of Figures 7.6 and 7.7 are expanded with the Zernike polynomials in order to get an idea of the relative amount of defocus and spherical aberration inside the pump-region (here the pump size was used as the Zernike radius). The refractive index phase change contributed ~85% to the total defocus and and 87% to the spherical aberration. The bulging contributed the balance. The total spherical aberration was roughly 11% of the defocus ($A_4^0 \sim 0.62$ vs. $A_2^0 \sim -5.7$) indicating that it was an order of magnitude smaller. However, it was still significant since the defocus is usually not considered as an aberration

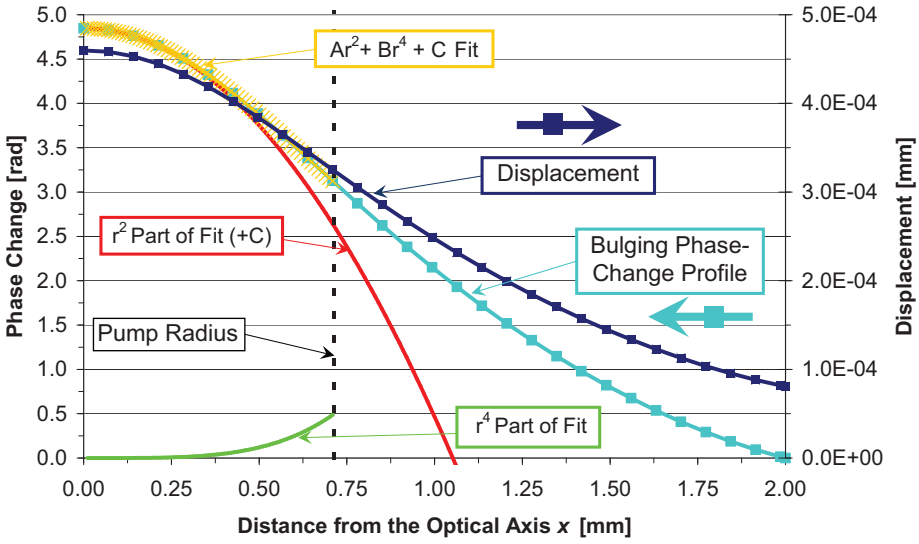

Figure 7.7: The phase change profile (light blue) due to the end-face bulging of a vanadate crystal with the temperature distribution seen in Figure 7.3. The displacement is plotted in dark blue on the right axis. The Seidel fit profiles to the phase change indicate that the end-face bulging also causes spherically aberrated thermal lensing inside the pump-region.

since it only changes the curvature of the wavefront.

7.4 Modelling of the experimental results

Thermal lens focal lengths were calculated for a range of pump powers in order to model our experimental results. We mainly used the properties of Nd:YVO_4 to evaluate different conditions and aspects of the thermal lensing in our experimental set-up.

7.4.1 Evaluating different dn_e/dT values of Nd:YVO_4 in the literature

We chose to only test the dn_e/dT values of Nd:YVO_4 since we have shown conclusively in the previous chapter that Nd:YVO_4 has the superior thermo-optical properties and is also much cheaper than Nd:$GdVO_4$.

Figure 7.8 illustrates the thermal lens dioptric power curves that were calculated with FEA simulations using several of the different dn_e/dT values of Nd:YVO_4 at 1.064 μm that are available in the literature (Table 2.4). The measured values from the mode-matching method that were presented in Figure 6.6 are also plotted on the same graph (in red diamonds). It is evident that the calculated values using Sato & Taira (2007)'s coefficient matched our measured values the best. The calculated dioptric curve of the dn_e/dT value from the manufacturers' data sheet (Castech, 2008) was approximately half the measured one.

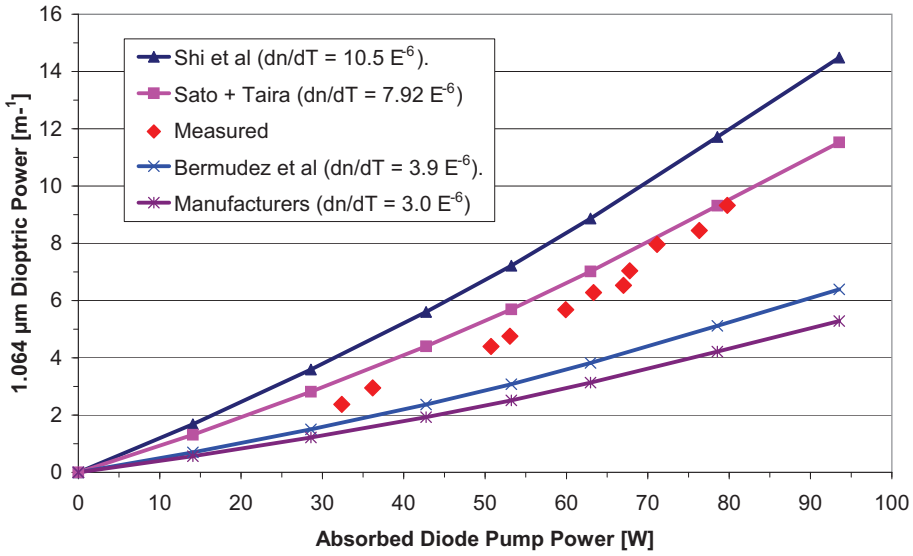

Figure 7.8: Dioptric powers calculated with FEA as a function of absorbed diode pump power using several values of the dn_e/dT values of Nd:YVO_4 that are available in literature. Experimental dioptric powers obtained using the mode-matching method are plotted in red diamonds.

The small discrepancy between the measured and the Sato & Taira (2007) calculated dioptric powers could have been due to:

1. measuring errors,
2. errors in other material parameters available in the literature,
3. input errors in LASCAD like the pump position, pump profile and absorption coefficients,
4. not being able to input a non-evolving pump profile into LASCAD.

We have therefore shown with one comprehensive experiment that Sato & Taira (2007)'s dn_e/dT value is the most correct one to use in thermal lens calculations of Nd:YVO_4.

7.4.2 Investigation of the non-linear increase in the dioptric power

The nonlinear increase observed in the experimental dioptric powers in Figure 6.6 could have been due to several factors. These are:

1. upconversion,
2. the varying absorption,
3. the end-face bulging or

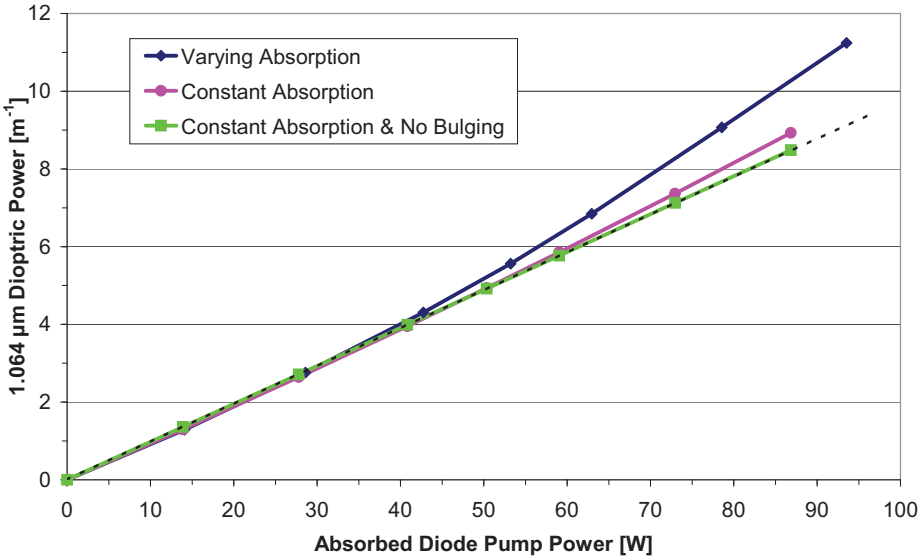

Figure 7.9: The calculated dioptric powers of the π-polarisation of Nd:YVO_4 while (blue diamonds) and without (pink circles) varying the absorption coefficients. The green square curve was calculated without varying the absorption coefficients and also ignoring the bulging of the pump-face.

4. the temperature dependence of the thermal conductivity.

We identified both the varying absorption and the end-face bulging as responsible. This section will illustrate how we did this by means of the numerical FEA calculations.

Firstly, upconversion (Section 2.5.5) could be ruled out because it was shown in Section 6.5.2 and Figure 6.15 that the heat load did not increase for nonlasing conditions, which should have happened if upconversion was present (Section 2.5.5).

Figure 7.9 illustrates the influence of the varying absorption due to the varying spectral output of the diode pump laser (Section 5.2.6) on the dioptric power of Nd:YVO_4's π-polarisation. The absorption increased with pump power because of the high absorption peak at 808 nm which was the wavelength of the diode module at maximum pump power. The varying absorption curve (blue diamonds) is the same as the one in Figure 7.8 that was calculated by using the dn_e/dT value given by Sato & Taira (2007). The constant absorption curve in Figure 7.9 was calculated with the absorption coefficients in the two transverse directions kept constant at the values of the first calculation point that had 16 W of total incident diode pump power (0.21 mm^{-1} for c and 0.08 mm^{-1} for a). The varying absorption curve extended further than the constant absorption curve because the absorption increases with pump power so that at full pump power more power is absorbed in the varying absorption curve.

It can be observed from Figure 7.9 that the varying absorption was clearly the predominant cause for the non-linear behaviour since the dioptric power increased almost linearly when the absorption was kept constant. The pump power was absorbed closer to the pump-face of the crystal at higher pump powers due to their higher absorption coefficients. This had two

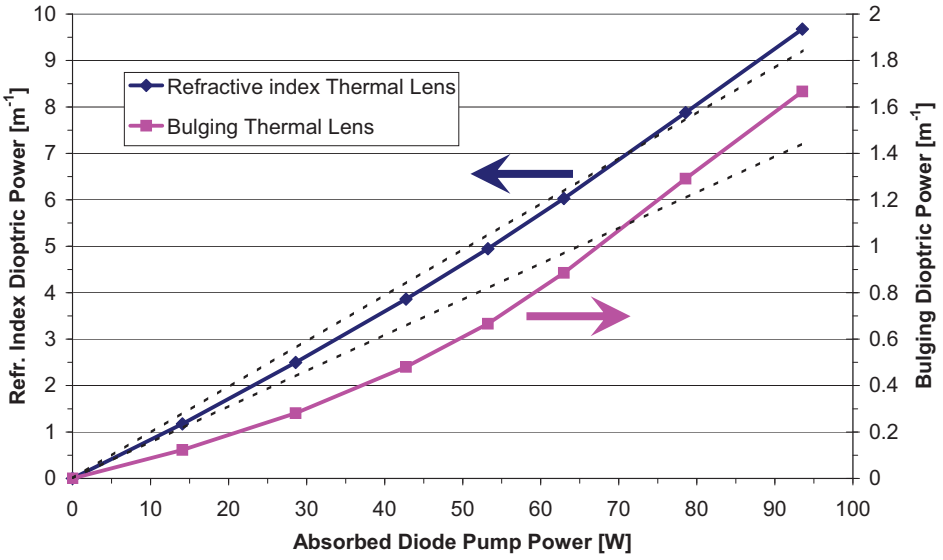

Figure 7.10: Contribution to the thermal lens from the refractive index profile (blue diamonds) and the bulging components (pink squares). The contribution from the bulging is ∼20% of the refractive index component and also increases more non-linearly.

main effects. The first was that the heat load became more localised at the pump-face which further increased its bulging. The second was a decrease of the effective pump radius. This can be explained by noting that the pump beam was focused close to the pump-face so that it diverged significantly within the crystal due to its poor beam quality. The percentage of absorbed power moved closer to the pump-face (where the pump beam radius was smaller) as the pump power was increased. This had a significant influence on the dioptric power of the thermal lens. It can be observed from Equation 5.6 that the thermal dioptric power is roughly dependent on the square of pump radius. The thermal dioptric power therefore increased non-linearly when the pump power was increased **and** the effective beam radius became smaller.

Figure 7.10 illustrates these two effects by separately plotting the refractive index and bulging dioptric power components as a function of the absorbed diode pump power. Linear fits through the two components are also plotted in broken lines. The scale of the bulging component on the right axis is five times smaller than the scale of the refractive index component on the left axis. The bulging component therefore contributed approximately only 20% to the total dioptric power. However, it did have a significant influence on the non-linear behaviour because of the localisation of the heat load at the pump face due to the increasing absorption. The non-linearity of the refractive index dioptric power component must therefore have been due to the decreasing effective radius.

The green curve in Figure 7.9 also illustrates the dioptric power when the absorption was kept constant **and** without bulging. From the perfect linear behaviour of the curve (seen from the dotted linear fit) it can be deduced that the small non-linear component

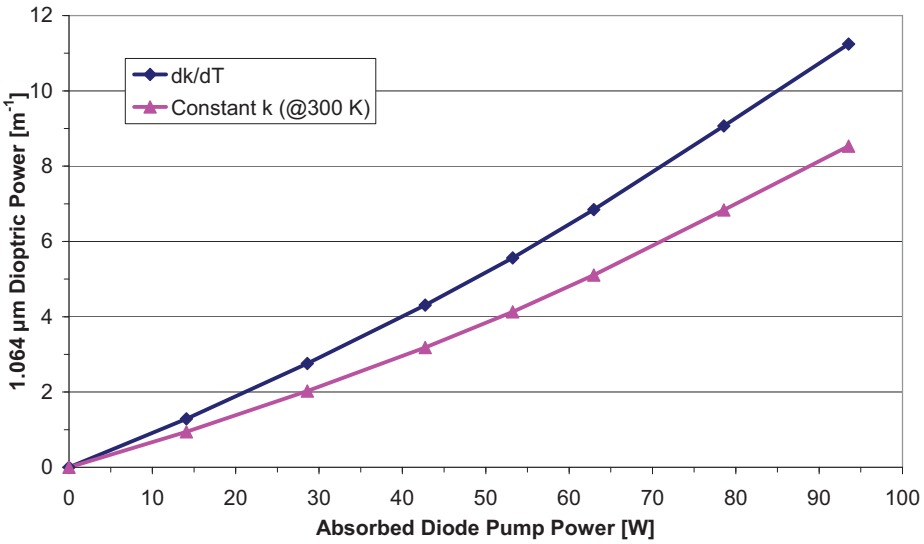

Figure 7.11: Influence of temperature dependence of the thermal conductivity on the dioptric power of the thermal lensing. The top curve (blue diamonds) takes into account the temperature dependency while the bottom one (pink triangles) does not.

observed in the constant absorption curve (pink circles) originates from the normal bulging component which did not increase linearly with absorbed pump power. This was due to a deviation from the plane stress approximation of Section 3.4.2 and is unlike the refractive index component which scaled linearly with absorbed pump power if the absorption coefficient stays constant (Equation 3.13). We can also deduce from this linear behaviour that the temperature dependence of the thermal conductivity did not contribute to the non-linear behaviour, because the thermal conductivity did vary with temperature in the calculations. In the next section we review what the influence of temperature dependence of the thermal conductivity on the dioptric power.

To summarise, the non-linear behaviour of the thermal lens was mostly due to the varying spectral output of the diode laser causing a varying absorption. It was also to a lesser degree due to the end-face bulging which did not increase linearly with absorbed diode pump power.

7.4.3 The influence of the temperature dependent thermal conductivity

The temperature dependence of the thermal conductivity is usually ignored in many calculations because its effects are regarded as negligibly small. Figure 7.11 illustrates the effect that it had on the FEA calculated dioptric powers. The top blue diamond curve is the same as the blue diamond one in Figure 7.9 which was calculated for the π-polarisation of Nd:YVO_4 with temperature dependent thermal conductivities (in the two crystallographic directions), varying absorptions and taking bulging into account. The pink triangle curve was calculated in a similar fashion but the thermal conductivities were kept constant at their 300 K values.

It can be observed that the two curves diverge to such an extent that at full pump power

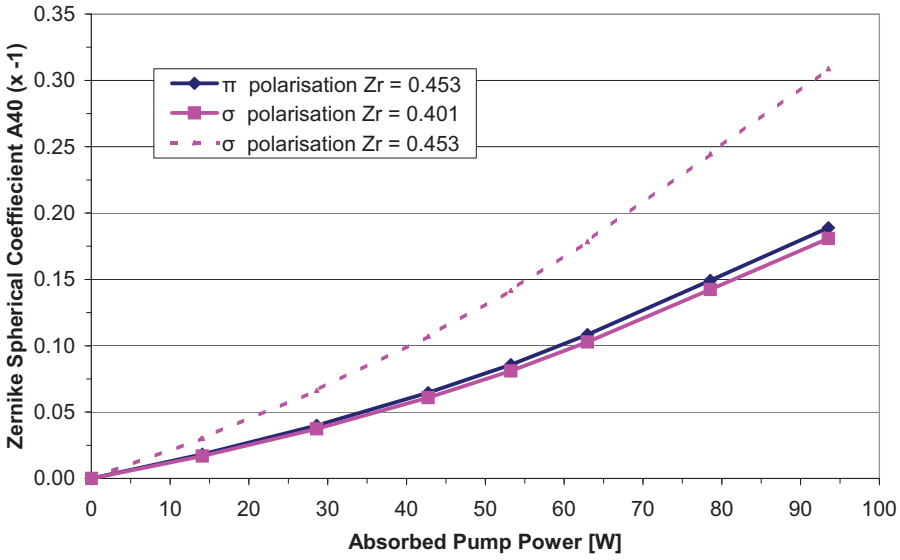

Figure 7.12: The A_4^0 Zernike spherical aberration coefficients of the thermal lensing of the π (blue diamonds) and σ (pink squares) polarisations of the TEM_{00} beams that were used in the mode matching method. The matched TEM_{00} radii were used as the Zernike radii in the bottom solid plots. For comparison the π-Zernike radius was used to calculate the σ-A_4^0 coefficient. The result can be seen as the top dotted curve.

the temperature dependent curve is approximately 20% higher than the constant curve. The increase is because the thermal conductivity decreased with temperature, which implies that heat was less efficiently conducted away. This led to an increase in the peak temperature in the crystal and therefore an increase in dioptric power. In a worst case scenario this can lead to a runaway thermal effect and catastrophic failure of the crystal. This finding therefore demonstrates that it is vital to take this temperature dependency into account in thermal calculations.

7.4.4 The influence of the spherical aberration

Section 3.4 concentrated on the general thermal phase change profiles inside the crystal. This section now focusses on the A_4^0 Zernike spherical coefficients of the two polarisations of Nd:YVO_4. Figure 7.12 illustrates that the spherical aberration increased non-linearly with absorbed diode pump power. This had severe effects on the TEM_{00} beams used in the mode-matching measurements.

Figure 6.10 illustrated that the effective slope efficiencies of these TEM_{00} lasers decreased with increasing pump power. Figure 7.12 now illustrates that this was due to the increase in the spherical aberrations which added extra losses to the system. A worrying trend is that spherical aberrations increase also non-linearly, which implies that the decrease of the slope efficiency will accelerate with pump power. This could have been the cause for the low output powers of the TEM_{00} double end-pumped laser experiments (Section 6.6) and illustrates the

need to combat or circumvent spherical aberrations in order to to power-scale these lasers.

The increase in TEM_{00} M^2 factors with pump power illustrated in Figure 6.8 could also be explained by the increase in spherical aberrations. A simple resonator can only generate a perfect single Gaussian TEM_{00} mode if there are no aberrations (and discriminates in some way against higher order modes). With aberrations present the output is technically no longer a Gaussian mode solution. In practice this manifests as an increase in the M^2 factor. However, the differences between the two solutions are small enough so that they are also generally referred to as TEM_{00} beams.

Figure 7.12 also shows that the thermal lenses of the π and σ-polarisations had almost exactly the same spherical aberrations when the matched TEM_{00} radii were chosen as their Zernike radii. For comparison, the A_4^0 coefficient of the thermal lens of the σ-polarisation was also calculated with the larger Zernike radius of the π-polarisation (Figure 6.9). The large difference this makes illustrates how close the spherical aberrations of the two polarisations actually were with respect to each other. The matched TEM_{00} beams therefore selected the same Zernike radius. This indicates that the matching ratio must depend in some way on the spherical aberrations through the Zernike radius. However, the matching did not depend on the absolute spherical aberration values because the matching ratio stayed constant with absorbed pump power (Figure 6.9), while the amount of spherical aberration increased (Figure 7.12).

7.4.5 The stress in the crystal

The thermal expansion also caused stress in the crystal. It was useful to calculate the von Mises stress (Equation 3.31) since it was defined as the stress at which materials start yielding when it reaches a critical value. LASCAD automatically calculated the von Mises stress and displayed it in a 3D visualisation. Figure 7.13 illustrates this for the crystal with the temperature profile seen in Figure 7.3. The highest stresses were clearly on the edges in the centre top and bottom positions of the crystal. We could therefore expect thermally induced crack formation to start from these positions where the stress is high. The edges also tend to have subsurface damage when the crystals are cut from the boule and cracks start from these damaged positions. Marion (1985) found that the maximum stress which the crystals can handle can be significantly increased if they are chemically etched after cutting to eliminate such subsurface damage.

A crack was observed during limited destructive testing (Section 5.2.6) and did indeed originate from the middle bottom of the crystal pump face from which it then proceeded to propagate vertically through the crystal. This can be observed in the photo insert of Figure 7.14.

Figure 7.14 plots (in blue diamonds) the values of the maximum von Mises stresses as a function of absorbed diode pump power for the cracked Nd:YVO_4 crystal. The experimentally determined pump power at which fracturing occurred is indicated with the red vertical line. The thermal fracture stress of this Nd:YVO_4 crystal was therefore $\sim$46 N/mm^2, as can be observed from the intersecting point of the red line with the von Mises stress curve. This compared well with the value in the literature of 53 N/mm^2 (Section 2.3.2).

We can also observe that the maximum von Mises stress increased non-linearly with

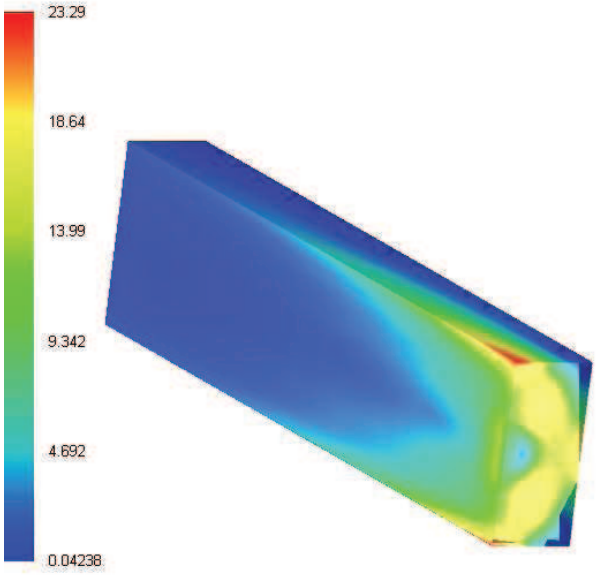

Figure 7.13: A 3D visualisation of the von Mises stress distribution (in N/mm^2) in the vanadate crystal with the temperature distribution seen in Figure 7.3. The crystal is vertically cut through the centre to allow observation of the stresses in the propagation direction.

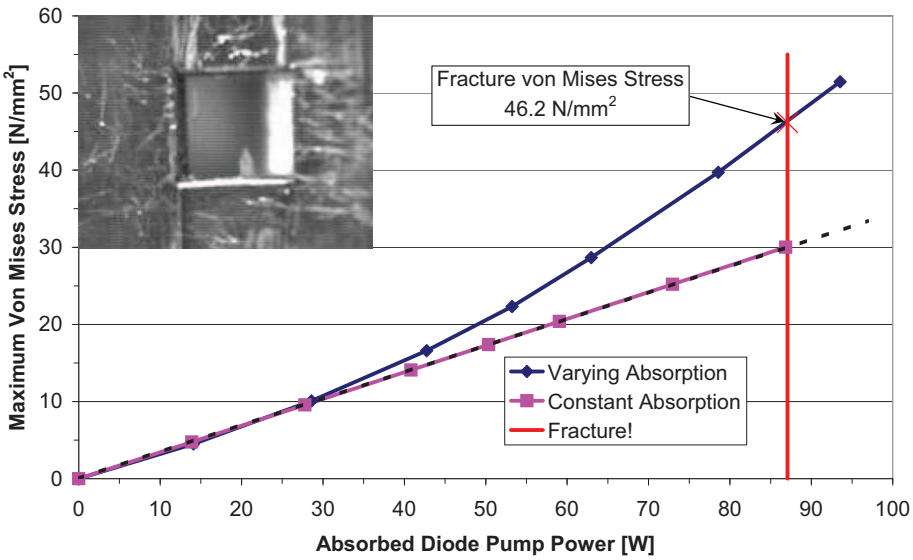

Figure 7.14: The von Mises stress in the crystal as a function of absorbed diode pump power for a varying (blue diamonds) and constant absorption (pink squares). The measured fracture power is indicated by the vertical solid red line.

absorbed diode pump power. In order to explain this, we also plotted the von Mises stresses that were calculated with the absorption coefficients held constant at their 16 W incident diode pump power levels (in pink squares) on Figure 7.14. From a linear fit to this curve (the dotted black line) we could observe that these von Mises stresses increased perfectly linear with absorbed pump power. Only the varying absorption was therefore responsible for this non-linear increase. Increasing absorption caused the heat load to shift to the front of the crystal and to become more localised. This increased the von Mises stress by more than a third at the fracture pump power. The heat load should therefore be spread out in future designs in order to power-scale end-pumped lasers.

7.5 Conclusion

In this chapter we used FEA numerical calculations to determine that Sato & Taira (2007)'s dn_e/dT value of Nd:YVO_4 matches our experimental results the best. We also show for the first time that the nonlinear increase in the thermal lens that was previously observed by others, was mostly due to a change of the spectral output of our pump diodes with current. It was also found that the temperature dependence of the thermal conductivity leads to an increases in the peak temperature but does not contribute to the nonlinear increase of the thermal dioptric power with absorbed pump power. Finally, we could determine the fracture stress limit of our Nd:YVO_4 crystals and their dependence on the absorbed diode pump power. In the next chapter we conclude this thesis and briefly give an outline of our future work.

Chapter 8

Summary, conclusions and future research

8.1 Summary and conclusions

Our investigation focused on techniques for power scaling end-pumped solid-state laser systems containing Nd^{3+} doped vanadate crystals. The research revealed a number of new findings relating to the thermal properties of Nd:YVO_4 and Nd:$GdVO_4$ as well as to strong positive aberrated thermal lenses and their influence on laser resonators.

We have used and compared three different experimental techniques to measure the strength of the thermal focal lens generated in the laser crystals at high pumping levels. These are:

1. the flat-flat quenching method,
2. a modified back calculation method using only TEM_{00} beams and
3. a probe beam technique.

We have developed a modified version of the method of Neuenschwander *et al.* (1995) to measure the thermal lens. By using only the TEM_{00} output of matched resonators we obtained more useful and repeatable measurements since only the central relatively unaberrated part of the thermal lens is measured by default. As an extra bonus, these measurements also provided us with the M^2 values and output powers of the optimal TEM_{00} beams. These values allowed us to quantify the negative effects of the aberrated thermal lenses on good quality (low M^2) output lasers.

The derived more reproducible thermal lens focal lengths could be used to compare the thermal lensing in Nd:YVO_4 and Nd:$GdVO_4$ directly at $1.064\,\mu$m. The results showed that Nd:YVO_4 had slightly weaker thermal lensing than Nd:$GdVO_4$ for the important, higher gain π-polarisation in contrast to other publications. We could also determine that in both materials the π-polarisation had roughly half the thermal lensing of the weaker gain σ-polarisation.

The probe beam method, was especially well-suited for comparative measurements and also demonstrated that Nd:YVO_4 has slightly weaker thermal lensing for both polarisations at 632 nm. More importantly, it revealed that there was almost no difference in thermal lensing under lasing and non-lasing conditions. This indicated that there was almost no upconversion present due to the low doping of the vanadate crystals. A consequence of the chosen favourable doping concentration was that the thermal lens was independent of the gain extraction profile, making the results from different resonator methods comparable. We could also determine the astigmatism of the thermal lens of both vanadates, which was a consequence of the uni-axial nature of the vanadates.

An important result of our investigations is that we could confirm the theory of Clarkson (2001) that resonators are more efficient if matching occurs in a region where $dw_\mathrm{l}/df_\mathrm{th} < 0$. This enables the construction of more efficient, good-beam-quality lasers.

Finite element analysis of the thermal behaviour in Nd:YVO_4 crystals, carried out with the help of LASCAD FEA models, has shown that of all the widespread values of Nd:YVO_4's dn_e/dT coefficient in the literature, the one reported by Sato & Taira (2007) corresponded the best with our experimental thermal lens measurements. Our modelling also showed that calculated thermal lenses are significantly weaker if the temperature dependence of the thermal conductivity is not taken into account. Furthermore, the model revealed that the nonlinear dependence of the dioptric power on the absorbed diode pump power was mostly due to the varying output spectrum of the pump with current and only to a lesser degree due to the end-face bulging. This non-linear behaviour was already observed in the literature but was not yet adequately explained.

Finally, we also developed new mounting techniques for square-cut laser crystals using heat conducting epoxy adhesive that efficiently conduct heat away from the crystal and that can be used widely in new systems. We found that our new mounting technique optimally cooled the laser crystals in our experiments. This enabled us to operate them at pump levels close to their fracture limit and extract output powers of over 65 W from a double end-pumped crystal.

8.2 Future research

The findings in this thesis can now be used to power-scale end-pumped vanadate lasers to higher levels. It is recommended that similarly low (or even lower) doped Nd:YVO_4 crystals be used. More research is needed to study the relationship between the pump profile and the thermal aberrations, slope efficiency and threshold. However, this work indicates that for materials with high dn/dT values such as Nd:YVO_4, more flat-top beams will most likely produce more efficient, high-power lasers. This is because, according to Figure 7.4, the influence of the spherical aberration is smaller for such pump beams. The absorption at maximum pump power must also be reduced and the crystal length increased in order to reduce the thermal stresses while maintaining the amount of pump power which is absorbed. It is also well worth investigating resonator designs in which matching occurs in regions where $dw_\mathrm{l}/df_\mathrm{th} < 0$ and which are not too alignment sensitive. If these steps are implemented, a two crystal quadruple pump setup can be built to obtain unprecedented average output powers

from intra-cavity doubled, Q-switched or mode-locked systems which can be used for various industrial and research applications.

Other interesting experiments would be to investigate the thermal lensing at 1.3 μm and also to develop high average power systems. However, this will be more challenging due to strong excited state absorption at this wavelength.

An analytical theory can also be developed to calculate the temperature and bulging of end-pumped crystals. A complete theory of thermal aberrations will enable the matching ratio to be increased by varying the pump profile while keeping the overall efficiency high. Alternatively, the program can be used to develop phase screens to correct for the optical aberrations in a resonator.

Another interesting experiment would be to vary the probe beam radius and monitor the ring formation. Probe beams from lasers built with other Nd^{3+} doped materials that emit close to the operating wavelength of the vanadates can be used to probe each other. By combining the probe beam experiments with a Shack-Hartman sensor the phase change profiles that cause the ring formation can be measured. In this way the rings can be correlated to the Zernike spherical aberration coefficient A_4^0.

While the main drawback of the vanadates are thermal aberrations, materials like YLF can be operated so that they have very weak thermal lensing and therefore little aberration. The trade-off is that the gain is lower and that YLF has a significantly lower fracture limit than most laser materials. YLF is also notorious for not showing any signs of stress until it fractures. A big problem is that there is very little experimental data on its fracture limits. We plan to do fracture tests on various low doped, short, uncoated Nd:YLF samples while monitoring the thermal aberrations with a Shack-Hartman wavefront sensor. This, coupled with the new thermal model, should enable us to better power scale end-pumped YLF lasers.

Appendix A

LASCAD input parameters

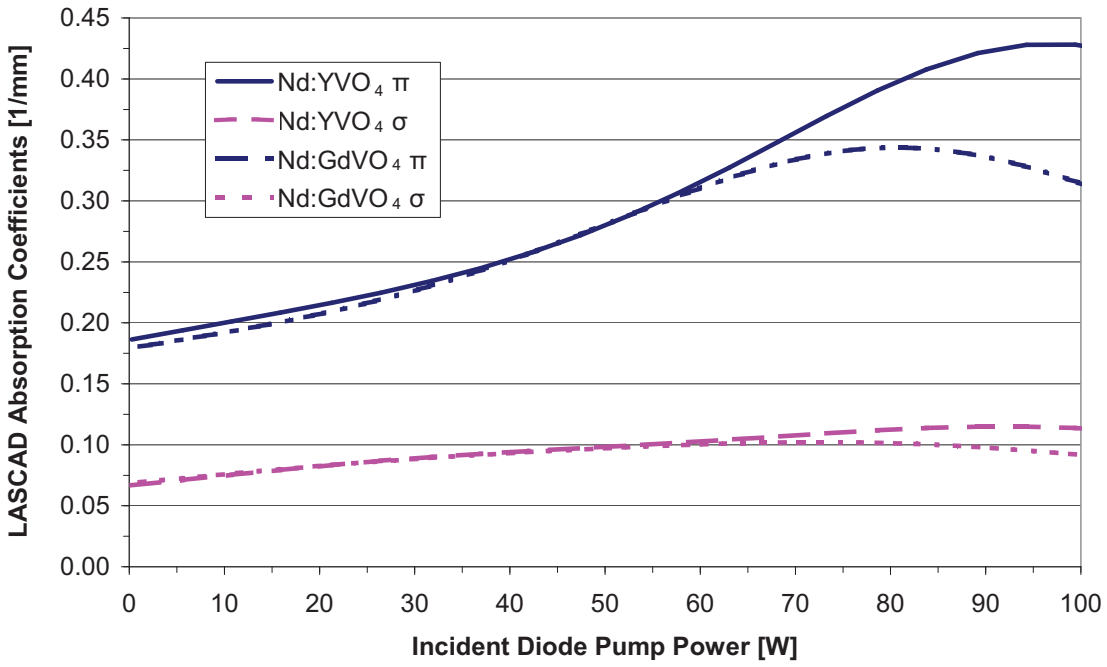

Figure A.1: The LASCAD absorption coefficients as a function of incident diode pump power.

Property	x-comp	y-comp	z-comp	Reference
$k_{\mathrm{th}}(T)$ [W/mmK]	$0.71632/T^{0.76766}$	$0.64394/T^{0.69711}$	$0.71632/T^{0.76766}$	Sato & Taira (2006)
α_{th} [1/K]	1.69E-06	8.19E-06	1.69E-06	Sato & Taira (2007)
E_{YM} [N/mm²]	133000	133000	133000	Ma *et al.* (2007)
ν_{Pois} (xy yz xz)	0.33	0.33	0.33	Ma *et al.* (2007)
n	Table 2.1	Table 2.1	Table 2.1	Sato & Taira (2007)
dn/dT [1/K]	Table 2.4	Table 2.4	Table 2.4	Sato & Taira (2007)
$\alpha_{\mathrm{abs}} \parallel$ [1/mm]	Figure A.1	$\alpha_{\mathrm{abs}} \perp$ [1/mm]	Figure A.1	Cross (2004)
$\%P \parallel$	50	η_{PH}:	0.24	Chen & Kuo (1998)
σ_{em} [mm²]	5.20E-17			Czeranowsky (2002)
τ_{s} [μs]	97			Czeranowsky (2002)
$\eta_{\mathrm{p\text{-}q}}$	0.9			Chen *et al.* (1999)

Table A.1: Nd:YVO_4 material properties used in LASCAD.

Property	x-comp	y-comp	z-comp	Reference
$k_{\mathrm{th}}(T)$ [W/mmK]	$0.82158/T^{0.79885}$	$0.89614/T^{0.78106}$	$0.82158/T^{0.79885}$	Sato & Taira (2006)
α_{th} [1/K]	1.14E-06	7.89E-06	1.14E-06	Sato & Taira (2007)
E_{YM} [N/mm²]	133000	133000	133000	Ma *et al.* (2007)
ν_{Pois}(xy yz xz)	0.33	0.33	0.33	Ma *et al.* (2007)
n	Table 2.1	Table 2.1	Table 2.1	Sato & Taira (2007)
dn/dT [1/K]	Table 2.4	Table 2.4	Table 2.4	Sato & Taira (2007)
$\alpha_{\mathrm{abs}} \parallel$ [1/mm]	Figure A.1	$\alpha_{\mathrm{abs}} \perp$ [1/mm]	Figure A.1	Cross (2004)
$\%P \parallel$	50	η_{PH}:	0.24	Chen & Kuo (1998)
σ_{em} [mm²]	1.25E-16			Czeranowsky (2002)
τ_{s} [μs]	100			Czeranowsky (2002)
$\eta_{\mathrm{p\text{-}q}}$	0.9			Chen *et al.* (1999)

Table A.2: Nd:$GdVO_4$ material properties used in LASCAD.

List of Publications

Masters Thesis

Strauss, H.J. 2005. (Correlations between the standard and alternative definitions of the beam quality factor. M.Sc. thesis, Department of Physics, University of Stellenbosch, Stellenbosch, South Africa.

International Conference Papers

Strauss, H.J., Bollig, C., Bergmann, H.M., & Esser, M.J.D. 2009. Comparative study of thermal lensing in low-doped Nd:YVO_4 and Nd:$GdVO_4$ of equal doping concentration. in *CLEO Europe*, Munich, Germany, paper CA9.5 (2009).

Bollig, C. **Strauss, H.J.**, Esser, M.J.D., Koen, W., Schellhorn, M., Preussler, D., Nyangaza, K., Jacobs, C., E.H., Bernhardi, & Botha, L.R.2009. Compact Fibre-Laser-Pumped Ho:YLF Oscillator-Amplifier System. in *CLEO Europe*, Munich, Germany, paper CA10.6 (2009).

Esser, M.J.D., **Strauss, H.**, Koen, W. S., Preussler, D., K., Nyangaza, & Bollig, C. 2009. Compact Fibre-Laser-Pumped Ho:YLF Oscillator-Amplifier System. in *Middle-Infrared Coherent Sources*, Trouville, France, (2009).

Strauss, H. J., Koen, W., Bollig, C., Esser, M. J. D., Preussler, D., K., Nyangaza, & Jacobs, C. 2009. Efficient Fiber-Laser-Pumped Ho:YLF Oscillator and Amplifier Utilizing the Transmitted Pump Power of the Oscillator. in *CLEO US*, Baltimore, USA, paper CWH3 (2009).

Bollig, C., Koen, W., **Strauss, H.**, Bernhardi, E., Botha, R., Esser, M. J. D., & Preussler, D. 2008. Exploiting the natural doping gradient of Nd:YLF crystals for high-power end-pumped lasers. in *3rd EPS-QEOD Europhoton Conference*, Paris, France, paper TUp.20 (2008).

Articles

Koen, K., Bollig, C., **Strauss, H.**, Schellhorn, M., Jacobs, C., & Esser, M.J.D. 2009. Compact Fibre-Laser-Pumped Ho:YLF Oscillator-Amplifier System. *Appl. Phys. B.*

Bibliography

Agnesi, A., & Uggetti, P. 2002. Measurement of thermal diffractive losses in end−pumped solid−state lasers. *Opt. Commun.*, **212**, 371 to 376.

Amarande, S.A, & Damzen, M.J. 2006. Measurement of the thermal lens of grazingincidence diode−pumped Nd:YVO_4 laser amplifier. *Opt. Commun.*, **265**, 306 to 313.

Anderson, F.G., Summers, P.L., Weidner, H., Hong, P., & Peale, R.E. 1994. Interpretive crystal−field parameters: Application to Nd^{3+} in $GdVO_4$ and YVO_4. *Phys. Rev. B: Condens. Matter*, **50**, 14802 to 14808.

Barnes, N.P. 2007. Solid−state lasers from an efficiency perspective. *IEEE J. Sel. Top. Quantum Electron.*, **13**, 435 to 447.

Bermudez, J.C., Pinto−Robledo, V.J., A.V., Kiryanov, & Damzen, M.J. 2002. The thermo−lensing effect in a grazing incidence, diode−side−pumped Nd:YVO_4 laser. *Opt. Commun.*, **210**, 75 to 82.

Bernhardi, E.H. 2008. *Modelling diode−pumped solid−state lasers.* M.Phil. thesis, School of Physics, University of Kwazulu−Natal, Durban, South Africa.

Bernhardi, E.H., Forbes, A., Bollig, C., & Esser, M.J.D. 2008. Estimation of thermal fracture limits in quasicontinuouswave endpumped lasers through a timedependent analytical model. *Opt. Express*, **16**, 11115 to 11123.

Blows, T., Omatsu, T., Dawes, J., Pask, H., & Tateda, M. 1998. Heat generation in Nd:YVO_4 with and without laser action. *IEEE Photonics Technol. Lett.*, **10**, 1727 to 1729.

Bollig, C. 1997. *Single−Frequency Diode−Pumped Solid−State Lasers.* Ph.D. thesis, Department of Physics, University of Southampton, Southampton, United Kingdom.

Born, M., & Wolf, E. 1986. *Principles of optics.* Sixth (corrected) edition edn. Headington Hill Hall, Oxford, 0X3 OBW, England: Pergamon Press.

Castech. 2008. *Castech.* Available: http://www.castech.com. last accessed 03 December 2008.

Chen, W., Shi, P., Hua, Z., Li., Long, & Gan, A. 2009. Semianalytical analysis of thermal effect in LD double−side−pumped rectangular laser crystal. *Opt. Commun.*, **282**, 3751 to 3756.

Chen, Y.F., & Kuo, H.J. 1998. Determination of the thermal loading of diode−pumped Nd:YVO_4 by use of thermally induced second−harmonic output depolarization laser−induced diffraction rings from a nematicliquid−crystal film. *Opt. Lett.*, **23**, 846–848.

Chen, Y.F., Huang, T.M., Kao, C.F., Wang, C.L., & Wang, S.C. 1997. Optimization in scaling fiber−coupled laser−diode end−pumped lasers to higher power: influence of thermal effect. *IEEE J. Quantum Electron.*, **33**, 1424 to 1429.

Chen, Y.F, Lee, L.J, Huang, T.M, & Wang, C.L. 1999. Study of high−power diode−end−pumped Nd:YVO_4 laser at 1.34 μm: influence of Auger upconversion. *Opt. Commun.*, **163**, 198 to 202.

Chen, Y.F, Liao, C.C, Lan, Y.P, & Wang, S.C. 2000. Determination of the Auger upconversion rate in fiber−coupled diode end−pumped Nd:YAG and Nd:YVO_4 crystals. *Appl. Phys. B*, **70**, 487 to 490.

Chenais, S., Balembois, F., Druon, F., Lucas−Leclin, G., & Georges, P. 2004. Thermal lensing in diode−pumped Ytterbium lasers Part I: theoretical analysis and wavefront measurements. *J. Quantum Electron.*, **40**, 1217 to 1234.

Chenais, S., Druon, F., Forget, S., Balembois, F., & Georges, P. 2006. On thermal effects in solid−state lasers: The case of ytterbium−doped materials. *Prog. Quantum Electron.*, **30**, 89 to 153.

Clarkson, W.A. 2001. Thermal effects and their mitigation in end−pumped solid−state lasers. *J. Phys. D: Appl. Phys.*, **34**, 2381 to 2395.

Coherent. 2009. *Coherent, Inc.* http://www.coherent.com/. last accessed 14 January 2009.

Cousins, A.K. 1992. Temperature and thermal stress scaling in finite−length end−pumped laser rods. *IEEE J. Quantum Electron.*, **28**, 1057 to 1069.

Cross, P.L. 2004. *Database of laser materials, Laser Systems Branch, NASA Langley Research Center, USA*. http://aesd.larc.nasa.gov/gl/laser/dbmain.htm. last accessed March 2005.

Csele, Mark. 2004. *Fundamentals of Light Sources and Lasers*. 2111 River Street, Hoboken, NJ 07030-5774: Wiley-IEEE.

Czeranowsky, C. 2002. *Resonatorinterne Frequenzverdopplung von diodengepumpten Neodym−Lasern mit hohen Ausgangsleistungen im blauen Spektralbereich*. Ph.D. thesis, Fachbereichs Physik, Universitët Hamburg, Hamburg, Germany.

Czeranowsky, C., Schmidta, M., Heumanna, E., G., Hubera, Kutovoib, S., & Zavartsevb, Y. 2002. Continuous wave diode pumped intracavity doubled Nd:$GdVO_4$ laser with 840 mW output power at 456 nm. *Opt. Commun.*, **205**, 361 to 365.

Du, C., Zhang, H., Ruan, S., Xu, G., Hu, D., Wang, Z., Xu, X., Wang, J., Xu, X, & Shao, Z. Jiang, M. 2004. Laser−diode−array end−pumped 8.2 W CW Nd:$GdVO_4$ laser at 1.34 μm. *IEEE Photonics Technol. Lett.*, **16**, 386 to 388.

Eichenholz, J.M, & Richardson, M. 1998. Measurement of thermal lensing in Cr−Doped colquiriites. *IEEE J. Quantum Electron.*, **34**, 910 to 919.

Epotek. 2008. *Epoxy technology engineered epoxies and adhesives for demanding applications website*. Available: http://www.epotek.com. last accessed 28 December 2008.

Ermeneux, F.S., Goutaudier, C., Moncorge, R., Cohen−Adad, M.T., Bettinelli, M., & Cavalli, E. 1999. Comparative optical characterization of various Nd^{3+}:YVO_4 single crystals. *Opt. Mater.*, **13**, 193 to 204.

Fan, T.Y., & Byer, R.L. 1988. Diode laser−pumped solid−state lasers. *IEEE J. Quantum Electron.*, **24**, 895 to 912.

Farrukh, U.O., Buoncristiani, A.M., & Byvik, C.E. 1988. An analysis of the temperature distribution in finite solid−state laser rods. *IEEE J. Quantum Electron.*, **24**, 2253 to 2263.

Festo. 2009. *Festo industrial automation*. http://www.festo.com/INetDomino/r1/en-za/company_portal_za.htm. last accessed 10 January 2009.

Hardman, P. J., Clarkson, W. A., Friel, G. J., Pollnau, M., & Hanna, D. C. 1999. Energy−transfer upconversion and thermal lensing in high−power end−pumped Nd:YLF laser crystals. *IEEE J. Quantum Electron.*, **35**, 647 to 655.

Hecht, Eugene. 1998. *Optics*. Reading, Massachusetts: Addison Wesley Longman, Inc.

Hodgson, Norman. 2005. *Laser resonators and beam propagation*. Second edition edn. Coherent Inc., 5100 Patrick Henry Drive, Santa Clara, CA 95054, USA: Springer−Verlag.

Hu, C., & Whinnery, J.R. 1973. New thermooptical measurement method and a comparison with other methods. *Appl. Opt.*, **12**, 72 to 79.

Innocenzi, M.E., Yura, H.T., Fincher, C.L., & Fields, R.A. 1990. Thermal modelling of continuous−wave end−pumped solid−state lasers. *Appl. Phys. Lett.*, **56**, 1831 to 1833.

ISO11146. 1999. Lasers and laser−related equipment − Test methods for laser beam parameters Beam widths, divergence angle and beam propagation factor. *International Organization for Standardization*, **1**, 124.

JENOPTIK. 2008. *Jenoptik laserdiode section website*. Available: http://www.jold.de. last accessed 28 December 2008.

Koechner, Walter. 1999. *Solid−state laser engineering*. Fifth revised and updated edition edn. 2855 Telegraph Avenue, Suite 600, Berkeley, CA 94705−1161: Springer−Verlag.

Kong, J., Tang, D.Y., Ng, S.P., Zhao, L.M., Qin, L.J., & Meng, X.L. 2004. High−power diode−end−pumped CW Nd:$GdVO_4$ laser. *Opt. Laser Technol.*, **37**, 5154.

Lancaster, D.G., & Dawes, J.M. 1998. Thermal−lens measurement of a quasi steady−state repetitively flashlamp−pumped Cr, Tm, Ho:YAG laser. *Opt. Laser Technol.*, **30**, 103 to 108.

LASCAD. 2008. *Laser Cavity Analysis and Design website*. Available: http://www.las−cad.com. last accessed 29 December 2008.

Lin, C.C., Ko, J.Y., Tsai, K.T., Cheng, Y.T., Ho, M.C, & Jiang, I.M. 2009. Effect of pump−beam conditions on dual polarization oscillations in a microchip Nd:$GdVO_4$ laser. *J. Phys. B: At. Mol. Opt. Phys.*, **42**, 1 to 4.

Liu, J., Shao, Z., Zhang, H., Meng, X., Zhu, L., & Jiang, M. 1999. Diode−laser−array end−pumped 14.3 W CW Nd:$GdVO_4$ solid−state laser at 1:06 μm. *Appl. Phys. B*, **69**, 241 to 243.

Ma, Z., Li, D., Gao, J., Wu, N., & Du, K. 2007. Thermal effects of the diode end−pumped Nd:YVO_4 slab. *Opt. Commun.*, **275**, 179 to 185.

Magni, V. 1986. Resonators for solid−state lasers with large−volume fundamental mode and high alignment stability. *Appl. Opt.*, **25**, 107 to 117.

Magni, V. 1987. Multi−element stable resonators containing a variable lens. *J. Opt. Soc. Am. A*, **4**, 1962 to 1969.

Malitson, I.H. 1965. Interspecimen comparison of the refractive index of fused silica. *J. Opt. Soc. Am*, **55**, 1205 to 1208.

Marion, J. 1985. Strengthened solid−state laser materials. *Appl. Phys. Lett.*, **47**, 694 to 696.

Mathematica. 2008. *Wolfram Research*. Available: http://www.wolfram.com/. last accessed 05 September 2009.

MATLAB. 2008. *The MathWorks Inc. website*. Available: http://www.mathworks.com. last accessed 29 December 2008.

Mei, Z., & Zhao, D. 2007. Kurtosis parameter of truncated standard and elegant Laguerre − Gaussian beams propagating through ABCD optical systems. *Opt. Laser Technol.*, **39**, 586 to 592.

Mudge, D., Veitch, P.J., Munch, J., Ottaway, D., & M.W., Hamilton. 1997. High−power diode−laser−lumped CW solid−state lasers using stable − unstable resonators. *IEEE J. Sel. Top. Quantum Electron.*, **3**, 19 to 25.

Mukhopadhyay, P.K., Nautiyal, A., Gupta, P.K., Ranganathan, K., George, J., Sharma, S.K., & Nathan, T.P.S. 2003. Experimental determination of the thermo−optic coefficient (dn/dT) and the effective stimulated emission cross−section (σ_e) of an a-axis cut 1.-at.% doped Nd:$GdVO_4$ crystal at 1.06 μm wavelength. *Appl. Phys. B*, **77**, 81 to 87.

Neal, D.R., & Mansell, J. 2008. *Application of Shack−Hartmann wavefront sensors to optical system calibration and alignment.* Available: http://www.wavefrontsciences.com/Application−2.pdf. last accessed 13 December 2008.

Neuenschwander, B., Weber, R., & Weber, H.P. 1995. Determination of the thermal lens in solid−state lasers with stable cavities. *IEEE J. Quantum Electron.*, **31**, 1082 to 1087.

Newport. 2009. *Millennia Prime 532 nm CW DPSS Lasers.* http://www.newport.com/pro3. last accessed August 2009.

Nienhuis, K. 1948. *On the influence of diffraction on image formation in the presence of aberrations.* Ph.D. thesis, University of Groningen, Groningen, Netherlands.

O'Donoghue, D. 2000. The correction of spherical aberration in the Southern African Large Telescope (SALT). *Proceedings of SPIE*, **4003**, 363 to 372.

Ogawa, T., Urata, Y., Wada, S.; Morikawa, J., Hashinioto, T., Higuchi, M., & Takahashi, J. 2005. Precise measurement of thermal conductivities of Nd−doped laser materials by the thermal wave analysis. in *Lasers and Electro− Optics Society, 2005. LEOS 2005. The 18th Annual Meeting of the IEEE, pp. 51 to 52.*

Okida, M., Itoh, M., Yatagai, T., Ogilvy, H., Piper, J., & Omatsu, T. 2005. Heat generation in Nd doped vanadate crystals with 1.34 μm laser action. *Opt. Express*, **13**, 4909 to 4915.

Ozygus, B., & Erhard, J. 1995. Thermal lens determination of end−pumped solid−state lasers with transverse beat frequencies. *Appl. Phys. Lett.*, **67**, 1361 to 1362.

Paschotta, R. 2008. *Field Guide to Lasers.* SPIE.

Paschotta, R. 2009. *Encyclopedia of Laser Physics and Technology.*

Peng, X., Asundi, A., Chen, Y., & Xiong, Z. 2001. Study of the mechanical properties of Nd:YVO_4 crystal by use of laser interferometry and finite−element analysis. *Appl. Opt.*, **40**, 1396 to 1403.

Pfistner, R., Weber, R., Merazzi, S., & Gruber, R. 1994. Thermal beam distortions in end−pumped Nd:YAG, Nd:GSGG, and Nd:YLF rods. *IEEE J. Quantum Electron.*, **30**, 1605 to 1615.

Pilkey, W. D. 1997. *Peterson's stress concentration factors.* Second edition edn. 605 Third Avenue, New York, NY, 10158−0012: John Wiley & Sons.

Pu, J. 1998. Focusing Gaussian beams by an annular lens with spherical aberration. *J. Mod. Opt.*, **45**, 239 to 247.

Saikawa, J., Sato, Y., Nakamura, O., & Furukawa, Y. 2005. Efficient 1.3 μm laser oscillation and heat generation characteristics in Nd:$GdVO_4$ laser under direct pumping into $^4F_{3/2}$ emitting level. in *Conference on Lasers and Electro− Optics/Quantum Electronics and*

Laser Science Conference and Photonic Applications Systems Technologies, OSA Technical Digest Series (CD) (Optical Society of America), OSA Technical Digest Series (CD) (Optical Society of America, 2005) paper CMS6.

Sato, Y., & Taira, T. 2006. The studies of thermal conductivity in $GdVO_4$, YVO_4, and $Y_3Al_5O_{12}$ measured by quasi−one−dimensional flash method. *Opt. Express*, **14**, 10528 to 10536.

Sato, Y., & Taira, T. 2007. Thermo−optical and mechanical parameters of Nd:$GdVO_4$ and Nd:YVO_4. in *Conference on Lasers and Electro− Optics/Quantum Electronics and Laser Science Conference and Photonic Applications Systems Technologies*, OSA Technical Digest Series (CD) (Optical Society of America), OSA Technical Digest Series (CD) (Optical Society of America, 2007) paper JWA87.

Sennaroglu, A. 1999. Experimental determination of fractional thermal loading in an operating diode−pumped Nd:YVO_4 minilaser at 1064 nm. *Appl. Opt.*, **38**, 3253 to 3257.

Sheldon, S.J., Knight, L.V., & Thorne, J.M. 1982. Laser−induced thermal lens effect: a new theoretical model. *Appl. Opt.*, **21**, 1663 to 1669.

Shen, H.Y., Meng, X.L., Zhang, G., Qin, J.J., Liu, W., Zhu, L., Huang, C.H., Huang, L.X., & Wei, M. 2004. Sellmeier's equation and the expression of the thermal refractive−index coefficient for a $Nd_{0.007}Gd_{0.993}VO_4$ crystal. *Appl. Opt.*, **43**, 955 to 960.

Shi, H., Zhang, G., & Shen, H. 2001. Measurement of principle refractive indices and the thermal refractive index coefficient of Yttrium vanadate. *J. Synth. Cryst. (Chinese)*, **30**, 85 to 88.

Siegman, Anthony E. 1986. *Lasers*. 20 Edgehill Road, Mill Valley, CA: University Science Books.

Song, F., Zhang, C., Ding, X., Xu, J., & Zhang, G. 2002. Determination of thermal focal length and pumping radius in gain medium in laser−diode−pumped Nd:YVO_4 lasers. *Appl. Phys. Lett.*, **81**, 2145 to 2147.

Stewen, C., Contag, K., Larionov, M., Giesen, A, & Hugel, H. 2000. A 1 kW CW thin disc laser. *IEEE J. Sel. Top. Quantum Electron.*, **6**, 650 to 657.

Wang, X., & Song, J. 2007. Multiphoton−excited upconversion luminescence of Nd:YVO_4. *Opt. Express*, **15**, 1384 to 1389.

Wetter, N.U., Sousa, E.C., Camargo, F.A., Ranieri, I.M, & Baldochi, S.L. 2008. Efficient and compact diode−side−pumped Nd:YLF laser operating at 1053 nm with high beam quality. *J. Opt. A: Pure Appl. Opt.*, **10**, 1 to 5.

Wu, H.H., Sheu, C.C., Chen, T.W, Wei, M.D., & Hsieh, W.F. 1999. Observation of power drop and low threshold due to beam waist shrinkage around critical configurations in an end−pumped Nd:YVO_4 laser. *Opt. Commun.*, **165**, 225 to 229.

Wyant, J. C., & Creath, K. 1992. *Basic Wavefront Aberration Theory for Optical Metrology.* Sixth (corrected) edition edn. New York: Academic Press, Inc., a subsidiary of Harcourt Brace Jovanovich.

Yan, L., & Lee, C.H. 1994. Thermal effects in end−pumped Nd:phosphate glasses. *J. Appl. Phys.*, **75**, 1286 to 1292.

Zagumennyi, A.I., Mikhailov, V.A., Vlasov, V.I, Sirotkin, A.A, Podreshetnikov, Yu. L., Zavartsev, Yu. D., Kutovoi, S.A., & Shcherbakov, I.A. 2003. Diode−pumped lasers based on $GdVO_4$ crystal. *Laser Phys.*, **13**, 311 to 318.

Zhang, H.J., Zhu, L., Meng, X.L, Yang, Z.H, Wang, C.Q, Yu, W.T., Chow, Y.T., & Lu, M.K. 1999. Thermal and laser properties of Nd:YVO_4 Crystal. *Cryst. Res. Technol.*, **34**, 1011 to 1016.